

# Design of a Dual-Polarized Dense Dipole Array for the SKA Mid-Frequency Aperture Array

by

Jacki Gilmore



*Dissertation presented for the degree of Doctor of  
Philosophy in Electronic Engineering in the Faculty of  
Engineering at Stellenbosch University*

Supervisor: Prof. D.B. Davidson

March 2016

# Declaration

By submitting this dissertation electronically, I declare that the entirety of the work contained therein is my own, original work, that I am the sole author thereof (save to the extent explicitly otherwise stated), that reproduction and publication thereof by Stellenbosch University will not infringe any third party rights and that I have not previously in its entirety or in part submitted it for obtaining any qualification.

Date: ..March 2016

Copyright © 2016 Stellenbosch University  
All rights reserved.



# Abstract

## Design of a Dual-Polarized Dense Dipole Array for the SKA Mid-Frequency Aperture Array

J. Gilmore

*Department of Electrical and Electronic Engineering,  
University of Stellenbosch,  
Private Bag X1, Matieland 7602, South Africa.*

Dissertation: PhD (Electronic)

March 2016

This dissertation presents the design of a dual-polarized Dense Dipole Array, or “DDA”, as a candidate element for the SKA Mid-Frequency Aperture Array. The design consists of tightly coupled dipole elements above a ground plane and is fed differentially through a specially designed common-mode suppressing feed.

Apart from the DDA, there are currently three design concepts under evaluation for the SKA Mid-Frequency aperture array as part of the SKA Advanced Instrumentation Program. The strength of the DDA is that it is a planar structure consisting only of a ground plane and an array element layer in addition to the feed structure, while the other geometries are either three layer or three dimensional structures, all of which complicates mass production of the array tiles.

The design is an implementation of Wheeler’s current sheet array and based on work by Munk, where a combination of the capacitances between the tips of neighbouring elements and the close proximity of the elements to one another are exploited in order to increase the overall bandwidth of the array.

In the first part of the dissertation, the design is restricted to the single-polarized case and an extensive parameter study is done in order to gain a better understanding of the physics involved. The single-polarized design is then optimised using a commercial genetic algorithm optimiser and simulation results are obtained that indicate that a bandwidth of 3.8:1 is achievable with good impedance behaviour with scan angle. A scan loss of < 5 dB across all in-band frequencies was also demonstrated.

The second part of the dissertation expands the single-polarized design to a dual-polarized design. Although difficulties were encountered with the optimisation of the dual-polarized design resulting in a perceived performance penalty from that of the single-polarized case, it is anticipated that performance similar to that of the single-polarized case will be achievable should an optimal design be identified. It has, however, been shown that the stability of the impedance with scan angle as well as the scan loss is still comparable to that of other MFAA front-end concepts.

The third part of the dissertation presents a design of an antenna feed that suppresses common-mode resonances commonly encountered in connected antenna arrays. The design makes use of symmetrical wideband microstrip-slotline transitions to cancel out common-mode signals, while differential-mode signals will still propagate through. The design is verified using both simulations and measurements of a manufactured prototype. A wide bandwidth and a CMRR  $> 30$  dB is achieved that exceeds the design specifications set out.

Lastly, both the single-polarized as well as the dual-polarized designs are verified using manufactured prototypes. A major contribution of this dissertation is the manufacturing of a  $\approx 1$  m<sup>2</sup> dual-polarized DDA prototype. The relatively flat embedded element pattern and good cross-polarization characteristics demonstrated with the large prototype is a crucial performance characteristic in achieving cost-effective digital beam-forming.

# Uittreksel

## Ontwerp van 'n Dubbel-Gepolariseerde Digte Dipool Samestelling vir die SKA Mid-Frekwensie Apertuur Samestelling

*("Design of a Dual-Polarized Dense Dipole Array for the SKA Mid-Frequency Aperture Array")*

J. Gilmore

*Departement Elektriese en Elektroniese Ingenieurswese,  
Universiteit van Stellenbosch,  
Privaatsak X1, Matieland 7602, Suid Afrika.*

Proefskrif: PhD (Elektronies)

Maart 2016

Hierdie proefskrif bied die ontwerp van 'n dubbel-gepolariseerde digte dipool samestelling, of "DDA", aan as 'n kandidaat topologie vir die SKA Mid-Frekwensie Apertuur Samestelling. Die ontwerp bestaan uit nou gekoppelde dipool elemente bo 'n grondvlak met 'n spesiaal ontwerpte voer wat gemene-modus resonanse onderdruk.

Buiten die DDA is daar tans drie ander ontwerpe onder oorweging vir die Mid-Frekwensie Apertuur Samestelling as deel van die SKA Gevorderde Instrumentasieprogram. Waar die ander ontwerpe of drie laag- of drie dimensionele strukture is wat massavervaardiging bemoeilik, is die DDA 'n planêre struktuur.

Die ontwerp is 'n implementasie van Wheeler se konstante-stroomplaat-samestelling en is gebaseer op werk gedoen deur Munk, waar 'n kombinasie van die kapasietansies tussen die punte van buurelemente en die nabyheid van elemente gebruik word om die bandwydte van die samestelling te verhoog.

In die eerste deel van proefskrif word die ontwerp beperk tot die enkel-gepolariseerde geval en 'n uitgebreide parameterstudie is voltooi om 'n beter verstaan te ontwikkel van die onderliggende fisika van die ontwerp. Die enkel-gepolariseerde ontwerp word dat ge-optimeer met 'n kommersiële optimeerder en simulasieresultate word bekom. Die simulasieresultate dui aan dat 'n bandwydte van 3.8:1 haalbaar is met goeie impedansiegedrag

oor 'n wye skanderingshoek. 'n  $< 5$  dB skanderingsverlies oor die volle frekwensiebereik word ook gedemonstreer.

Die tweede deel van die proefskrif brei die ontwerp uit na 'n dubbel-gepolariseerde ontwerp. Alhoewel probleme ondervind is met die optimering van die dubbel-gepolariseerde ontwerp wat gelei het tot 'n skynbare prestasieverlies, word daar verwag dat indien 'n optimale ontwerp ontwikkel kan word, die dubbel-gepolariseerde ontwerp soortgelyk aan die enkel-gepolariseerde ontwerp sal kan presteer. Daar is egter getoon dat die impedansiestabiliteit met skanderingshoek sowel as die skanderingsverlies steeds vergelykbaar is met die van ander MFAA topologieë.

Die derde deel van die proefskrif handel oor die ontwerp van 'n antennavoer wat gemene-modus resonanse - wat algemeen voorkom in verbinde antenna samestellings - onderdruk. Die ontwerp maak gebruik van simmetriese, wyeband mikrostrook-slootlyn oorgange om gemene-modus seine uit te kanselleer terwyl differensiële-modus seine toegelaat word om steeds deur te propageer. Die ontwerp word geverifieër deur van beide simulاسies sowel as metings van 'n vervaardigde prototipe gebruik te maak. 'n Wye bandwydte en 'n CMRR  $> 30$  dB word getoon wat die ontwerpsspesifikاسies wat gestel is oorskry.

Laastens word beide die enkel-gepolariseerde ontwerp sowel as die dubbel-gepolariseerde ontwerp geverifieër deur gebruik te maak van vervaardigde prototipes. A groot bydrae van hierdie proefskrif is die vervaardiging van 'n  $\approx 1$  m<sup>2</sup> dubbel-gepolariseerde DDA prototipe. Die relatiewe plat ingebedde stralingspatroon en goeie kruispolarisasie prestasie van die groot prototipe is 'n deurslaggewende prestasiekarakteristiek om koste-effektiewe digitale bondelvorming te vermag.

# Acknowledgements

I would like to express my sincere gratitude to the following people and organisations:

- My supervisor, Prof. David Davidson for his patience, insight and guidance throughout the project. Thank you for sharing your knowledge with me.
- Jan Geralt Bij de Vaate for hosting me at ASTRON for multiple visits, as well as the insight provided during discussions.
- Jan Noordam, for sharing his interesting point of view on radio astronomical receivers that lead to the design presented in this dissertation.
- Wim van Capellen for his support during my last ASTRON visit.
- Michel Arts for assisting me with my measurements at ASTRON.
- Albert van Duin for his unbelievably fast PCB manufacturing as well as insights into PCB manufacturing techniques.
- Raymond van den Brink for helping with the mechanical side of the manufacturing of the first prototype.
- Sjouke Kuindersma for helping to find mechanical solutions for the manufacture of the large prototype.
- Wessel Croukamp for painstakingly assembling the large prototype - your contribution can not be understated!
- Anneke Bester, for assisting me with my measurements at Stellenbosch.
- David Prinsloo, for providing valuable last-minute insight on obtaining the mixed-mode measurement results.
- Danie Lüdick, for being the go-to guy when getting stuck with my simulations.

- ASTRON (and all the other people who assisted me during my visits who are not named above), for hosting me on multiple occasions. Without these visits, this project would have not been possible.
- The following organisations for their financial support:
  - SKA South Africa through the S.A. Research Chairs Initiative of the Department of Science and Technology
  - S.A. National Research Foundation under Grant 75322
  - European Community FP7 program, MIDPREP, under Grant PIRSES-GA-2013-612599.
- My parents: Thank you for your words of encouragement and for believing in me.
- Lastly, my husband John for his unending support, comfort, encouragement and patience, delivered in the correct doses at the correct times. For believing in me from day one and for understanding when I was away from home for extended periods. You are an incredible partner!

# Dedications

*This dissertation is dedicated to my husband, John.*

# Contents

<b>Declaration</b>	<b>i</b>
<b>Abstract</b>	<b>ii</b>
<b>Uittreksel</b>	<b>iv</b>
<b>Acknowledgements</b>	<b>vi</b>
<b>Dedications</b>	<b>viii</b>
<b>Contents</b>	<b>ix</b>
<b>List of Figures</b>	<b>xi</b>
<b>List of Tables</b>	<b>xvi</b>
<b>Nomenclature</b>	<b>xvii</b>
<b>1 Introduction</b>	<b>1</b>
1.1 The Square Kilometre Array . . . . .	1
1.2 Introduction to Dense Aperture Arrays . . . . .	2
1.3 The Mid-Frequency Aperture Array . . . . .	3
1.4 Contributions . . . . .	3
1.5 Layout of the Dissertation . . . . .	4
<b>2 Literature Study</b>	<b>6</b>
2.1 Introduction . . . . .	6
2.2 The Infinite Current Sheet Concept . . . . .	6
2.3 Full-Wave and Reduced-Order Modelling Methodologies for Dense Aperture Arrays . . . . .	7
2.4 MFAA Performance Requirements . . . . .	9
2.5 Introduction to other MFAA Topologies . . . . .	12
2.6 Conclusion . . . . .	15
<b>3 The Basic Dense Dipole Array</b>	<b>16</b>
3.1 Introduction . . . . .	16



**CONTENTS**

x

3.2	Theoretical Background . . . . .	17
3.3	Parameter Study . . . . .	21
3.4	Optimisation . . . . .	44
3.5	Results . . . . .	48
3.6	Conclusions . . . . .	57
<b>4</b>	<b>The Dual-Polarized DDA</b>	<b>58</b>
4.1	Introduction . . . . .	58
4.2	Geometry . . . . .	58
4.3	Optimisation . . . . .	59
4.4	Results . . . . .	62
4.5	Conclusion . . . . .	73
<b>5</b>	<b>The Common-Mode Suppressing Feed</b>	<b>75</b>
5.1	Introduction . . . . .	75
5.2	Theoretical Background . . . . .	77
5.3	Feed Network Design . . . . .	81
5.4	Measurement Procedure . . . . .	87
5.5	Results . . . . .	88
5.6	Conclusion . . . . .	89
<b>6</b>	<b>Results</b>	<b>91</b>
6.1	Introduction . . . . .	91
6.2	Description of the Multi-Port Mixed-Mode S-parameter Measurement Procedure . . . . .	91
6.3	The $4 \times 4 \times 1$ Prototype . . . . .	93
6.4	The $10 \times 10 \times 2$ Prototype . . . . .	97
6.5	Conclusion . . . . .	103
<b>7</b>	<b>Conclusion and Future Work</b>	<b>111</b>
	<b>Bibliography</b>	<b>115</b>

# List of Figures

2.1	Magnitude and Phase of a single Vivaldi element for a reduced-order compared to a full-wave MoM solution using FEKO . . . . .	8
2.2	The percentage error between the reduced-order and the full-wave solution . . . . .	9
2.3	Propagation paths of noise waves that emanate from an LNA when connected to an antenna in a mutually coupled array. . . . .	11
2.4	Four THEA Tiles . . . . .	13
2.5	The aluminium vivaldi elements at one of the EMBRACE stations	13
2.6	Geometry of two-dimensional ORA unit cell . . . . .	14
2.7	FEKO model and dimensions of an LPDA element for MFAA . . . . .	15
3.1	An infinite dipole array backed by a ground plane [1] . . . . .	17
3.2	Visualisation of a DDA structure with single polarizations . . . . .	19
3.3	Basic current distribution on a linear DDA . . . . .	20
3.4	Parameters of the DDA . . . . .	22
3.5	Active reflection coefficient at broadside for different pitch values. Element width = 7.5 mm and Tip Gap = 0.5 mm. . . . .	22
3.6	Active reflection coefficient at broadside for different element spacings. Element width = 7.5 mm and Tip Gap = 1 mm. . . . .	23
3.7	Active reflection coefficient at broadside for different element spacings. Element width = 7.5 mm and Tip Gap = 1.5 mm. . . . .	24
3.8	Active reflection coefficient at broadside for different element spacings. Element width = 10 mm and Tip Gap = 1 mm. . . . .	25
3.9	Active reflection coefficient at broadside for different element spacings. Element width = 10 mm and Tip Gap = 1 mm. . . . .	26
3.10	Equivalent Circuit . . . . .	26
3.11	Single-Ended 2-port DUT . . . . .	27
3.12	Active reflection coefficient vs difference between single-ended port impedances. . . . .	28
3.13	Raw results of the full parameter study . . . . .	29
3.14	Raw results of the full parameter study . . . . .	30
3.15	Active reflection coefficient data from the parameter sweep, sorted i.t.o. data correlation . . . . .	31

3.16	Active reflection coefficient data from the parameter sweep, sorted sorted i.t.o. Bandwidth (in-band < -10 dB) . . . . .	33
3.17	Active reflection coefficient data vs relationships between the length, the width and the pitch, sorted i.t.o. Bandwidth (in-band < -10 dB)	34
3.18	Active reflection coefficient data from the parameter sweep, sorted i.t.o. Bandwidth (in-band < -15 dB) . . . . .	35
3.19	Active reflection coefficient data vs relationships between the length, the width and the pitch, sorted i.t.o. Bandwidth (in-band < -15 dB)	36
3.20	Active reflection coefficient data from the parameter sweep, sorted i.t.o. Fmax (in-band < -10 dB) . . . . .	37
3.21	Active reflection coefficient data vs relationships between the length, the width and the pitch, sorted i.t.o. Fmax (in-band < -10 dB) . . .	38
3.22	Active reflection coefficient data from the parameter sweep, sorted i.t.o. Fmax (in-band < -15 dB) . . . . .	39
3.23	Active reflection coefficient data vs relationships between the length, the width and the pitch, sorted i.t.o. Fmax (in-band < -15 dB) . . .	40
3.24	Active reflection coefficient data from the parameter sweep, sorted i.t.o. Fmin (in-band < -10 dB) . . . . .	41
3.25	Active reflection coefficient data vs relationships between the length, the width and the pitch, sorted i.t.o. Fmin (in-band < -10 dB) . . .	42
3.26	Active reflection coefficient data from the parameter sweep, sorted i.t.o. Fmin (in-band < -15 dB) . . . . .	43
3.27	Active reflection coefficient data vs relationships between the length, the width and the pitch, sorted i.t.o. Fmin (in-band < -15 dB) . . .	44
3.28	Comparison of the active reflection coefficients of the optimal parameter set from Optimization 1 compared to practical parameter values. . . . .	47
3.29	Comparison of the active reflection coefficients of the optimal parameter set from Optimisation 2 compared to practical parameter values. . . . .	48
3.30	Comparison of the active reflection coefficient at broadside of Optimisation 1 and Optimisation 2. . . . .	49
3.31	Active reflection coefficient at broadside for an infinite single polarized DDA . . . . .	50
3.32	Visualisation of the tested scan range along the <i>E</i> -plane. . . . .	51
3.33	Active reflection coefficient for various scan angles along the <i>E</i> -plane . . . . .	52
3.34	Visualisation of the tested scan range along the <i>H</i> -plane. . . . .	53
3.35	Active reflection coefficient for various scan angles along the <i>H</i> -plane . . . . .	53
3.36	Scan loss for $\theta_0 = 45^\circ$ , on the <i>E</i> -plane and <i>H</i> -plane . . . . .	55
3.37	Co-polar and cross-polar gain patterns along the <i>E</i> -plane. . . . .	56
3.38	Co-polar and cross-polar gain patterns along the <i>H</i> -plane. . . . .	56
3.39	Co-polar and cross-polar gain patterns along the <i>D</i> -plane. . . . .	57

4.1	A Dense Dipole Array Prototype . . . . .	59
4.2	Active reflection coefficient for the optimal- and three practical parameter sets. . . . .	60
4.3	Active reflection coefficient vs difference between single-ended port impedances. . . . .	61
4.4	Active reflection coefficient at broadside . . . . .	63
4.5	Visualisation of the tested scan range along the $E$ -plane, with a co-polarized incoming wave-front. . . . .	64
4.6	Active reflection coefficient for various scan angles along the $E$ -plane, with a co-polarized incoming wave-front. . . . .	65
4.7	Visualisation of the tested scan range along the $E$ -plane, with a cross-polarized incoming wave-front. . . . .	66
4.8	Active reflection coefficient for various scan angles along the $E$ -plane, with a cross-polarized incoming wave-front. . . . .	67
4.9	Visualisation of the tested scan range along the $H$ -plane, with a co-polarized incoming wave-front. . . . .	67
4.10	Active reflection coefficient for various scan angles along the $H$ -plane, with a co-polarized incoming wave-front. . . . .	68
4.11	Visualisation of the tested scan range along the $H$ -plane, with a cross-polarized incoming wave-front. . . . .	68
4.12	Active reflection coefficient for various scan angles along the $H$ -plane, with a cross-polarized incoming wave-front. . . . .	69
4.13	Scan loss for $\theta_0 = 45^\circ$ , on the $E$ -plane and $H$ -plane . . . . .	70
4.14	Normalised co-polar H-plane gain pattern for two relative ground plane heights . . . . .	71
4.14	Normalised co-polar and cross-polar gain patterns for an embedded element in an infinite array. The trace indices for all three plots are as follows: (1) Co-pol at 1 GHz, (2) Co-pol at 700 MHz, (3) Co-pol at 500 MHz, (4) Cross-pol at 1 GHz, (5) Cross-pol at 700 MHz, (6) Cross-pol at 500 MHz . . . . .	73
5.1	Fields in a Microstrip-Slotline Transition During Differential Mode Operation . . . . .	75
5.2	Active reflection coefficient at for a single-polarized DDA with varying feed lengths . . . . .	76
5.3	The Basic Microstrip-Slotline Transition . . . . .	78
5.4	Fields due to in-phase currents at a Symmetrical Microstrip-Slotline Transition . . . . .	79
5.5	Fields due to $180^\circ$ out of phase currents at a Symmetrical Microstrip-Slotline Transition . . . . .	80
5.6	Equivalent circuit of a symmetrical Microstrip-Slotline Transition . . . . .	81
5.7	Detailed Feed Design (See text for more details) . . . . .	82
5.8	Equivalent Circuit Model of the Feed Network . . . . .	83

5.9	Equivalent Circuit Transformation Steps for Differential-Mode Impedance Matching . . . . .	84
5.10	Dimensions . . . . .	86
5.11	Photograph of the manufactured prototype . . . . .	87
5.12	Single-Ended 4-port DUT . . . . .	88
5.13	Differential-Mode Transmission . . . . .	89
5.14	Common-Mode Transmission . . . . .	90
5.15	Common-Mode Rejection Ratio . . . . .	90
6.1	Array Assembly . . . . .	94
6.2	Array Assembly . . . . .	95
6.3	Measured and Simulated $\Gamma_{dd}$ at broadside for a central element in the array . . . . .	95
6.4	$\Gamma_{dd}$ at broadside for a corner element in the array . . . . .	96
6.5	$\Gamma_{cc}$ at broadside for a corner- and central element in the array . . . . .	97
6.6	Photograph of the $10 \times 10 \times 2$ DDA prototype mounted in the anechoic chamber. . . . .	98
6.7	Photograph of the feed board being used to feed the $10 \times 10 \times 2$ DDA prototype . . . . .	99
6.8	Photograph detailing the plastic laser-cut plates and standoffs that provide the mechanical support between the PCB layer and the ground plane. . . . .	100
6.9	Photograph of the continuous array structure of the $10 \times 10 \times 2$ DDA prototype . . . . .	100
6.10	Simulation model of the $10 \times 10 \times 2$ prototype. . . . .	101
6.11	Differential-mode reflection coefficient of a central element in the $10 \times 10 \times 2$ prototype array. . . . .	102
6.12	Differential-mode reflection coefficient of central elements in the $10 \times 10 \times 2$ prototype array of both horizontal and vertical polarization. . . . .	103
6.13	Common-mode reflection of a central element in the $10 \times 10 \times 2$ prototype array. . . . .	104
6.14	Common-mode reflection coefficient of central elements in the $10 \times 10 \times 2$ prototype array for both horizontal and vertical polarization. . . . .	105
6.15	Differential-mode mutual coupling between neighbouring co- and cross-polarized elements in the $10 \times 10 \times 2$ prototype array. . . . .	106
6.16	Common-mode mutual coupling between neighbouring co- and cross-polarized elements in the $10 \times 10 \times 2$ prototype array. . . . .	107
6.17	Mixed-mode mutual coupling between neighbouring co- and cross-polarized elements in the $10 \times 10 \times 2$ prototype array. . . . .	108
6.18	Normalised co-polar and cross-polar gain patterns along the $E$ -plane for an embedded element. . . . .	109

*LIST OF FIGURES*

6.19 Normalised co-polar and cross-polar gain patterns along the  $H$ -  
plane for an embedded element. . . . . 110

# List of Tables

3.1	Parameters of the DDA . . . . .	21
3.2	Details of the optimisation parameters. . . . .	45
3.3	Optimisation 1 output parameters . . . . .	46
3.4	Practical values for Optimisation 1 . . . . .	46
3.5	Optimisation 2 output parameters . . . . .	46
3.6	Practical values for Optimisation 2 . . . . .	47
4.1	Optimal and practical parameters values for the dual-polarized DDA . . . . .	60
5.1	Antenna Specifications . . . . .	81
5.2	Feed Network Specifications . . . . .	82
5.3	Feed Network Specifications . . . . .	86

# Nomenclature

## Constants

$$c = 2.99792458 \times 10^8$$

## Abbreviations

$\lambda$	Wavelength
AA	Aperture Array
$A_{\text{eff}}$	Effective Area
BW	Bandwidth
CBFM	Characteristic Basis Function Method
CMRR	Common-Mode Rejection Ratio
Co-Pol	Co-polar
Cross-Pol/X-Pol	Cross-Polar
CSA	Current Sheet Array
DDA	Dense Dipole Array
DGFM	Domain Green's Function Method
DUT	Device Under Test
$E$ -Field	Electric Field
EM	Electromagnetic
EMBRACE	Electronic Multi Beam Radio Astronomy Concept
FoV	Field of View
GA	Genetic Algorithm
$\Gamma_{\text{act}}(\theta, \phi)$	Active Reflection Coefficient at scan angle $(\theta, \phi)$
$H$ -Field	Magnetic Field
LFAA	Low-Frequency Aperture Array
LNA	Low Noise Amplifier
LPDA	Log-Periodic Dipole Array
MFAA	Mid-Frequency Aperture Array
MM	Mixed Mode
MoM	Method-of-Moments



ORA	Octagonal Ring Antenna
PAF	Phased Array Feed
PCB	Printed Circuit Board
SE	Single-Ended
SKA	Square Kilometre Array
SKALA	SKA Log-Periodic Antenna
SSFoM	Survey Speed Figure of Merit
TE	Transverse Electric
THEA	Thousand Element Array
TM	Transverse Magnetic
$T_{\text{sys}}$	System Noise Temperature
VNA	Vector Network Analyser

# Chapter 1

## Introduction

### 1.1 The Square Kilometre Array

In a few years, the Square Kilometer Array (SKA) will become the most sensitive radio telescope in the world. Current specifications for the SKA include a required operation from 70 MHz to 25 GHz and an effective increase in FoV (Field of View) at frequencies between roughly 0.3 and 1 GHz of at least two orders of magnitude from existing instruments. This increased FoV will allow larger portions of the sky to be surveyed in a more time efficient manner, which is a requirement for many of the science cases of the SKA [2–5].

As a result of these science requirements, an important specification for the SKA is survey speed, which can be quantified using the survey speed figure of merit (SSFoM). The SSFoM and sensitivity is expressed in terms of the effective area  $A_{\text{eff}}$ , the system noise temperature  $T_{\text{sys}}$ , and the FoV as follows [4,6]:

$$\text{SSFoM} = (\text{Sensitivity})^2 \times \text{FoV}, \quad (1.1.1)$$

with

$$\text{Sensitivity} = \frac{A_{\text{eff}}}{T_{\text{sys}}}. \quad (1.1.2)$$

Optimising the SSFoM would therefore involve attempting to increase both the sensitivity as well as the FoV of the telescope, and from Equation 1.1.2 it follows that the sensitivity is maximized by minimizing  $T_{\text{sys}}$  while increasing  $A_{\text{eff}}$ .

Furthermore, the parameters that have the greatest influence on  $T_{\text{sys}}$  and  $A_{\text{eff}}$  change as a function of frequency, which results in different design concepts being favoured for different frequency bands of the SKA [2,3,7,8].

In summary, sparse aperture arrays are better suited for frequencies below  $\sim 400$  MHz since  $T_{\text{sys}}$  is dominated by sky noise at those frequencies [2].

At frequencies above  $\sim 400$  MHz, the receiver noise temperature starts being the biggest contributor of  $T_{\text{sys}}$ . In order to retain the near constant sensitivity over the entire frequency band, a dense configuration is more suited (i.e. inter-element spacing to be limited to not much more than  $\lambda/2$  across the entire scan range) [7]. For frequencies above  $\sim 1$  GHz the most cost-effective solution is a reflector-based system [4].

Currently, a number of dense aperture array topologies are being investigated as a possible candidate for the mid-frequency range from roughly 450 to 1450 MHz. These include the Vivaldi array and the Octagonal Ring Antenna (ORA). With their ability to point in multiple directions simultaneously, the FoV of these arrays is limited only by the available processing power [9]. Technological road mapping indicates that forthcoming developments in cost effective element manufacturing processes, LNA technology as well as signal processing will make this topology a more suitable option from 2018 onwards [10].

This dissertation proposes a new dense aperture array concept called the Dense Dipole Array (DDA). The design is an implementation of Wheeler's current sheet array [11] and based on work by Munk [12, 13], where a combination of the capacitances between the tips of neighbouring elements and the close proximity of the elements to one another are exploited in order to increase the overall bandwidth. The planar nature of the DDA structure will aid in simplifying mass-production and deployment of the array.

## 1.2 Introduction to Dense Aperture Arrays

Dense arrays are made up of a number of small receiving elements which are each connected to an LNA. Signals from each element are filtered and further amplified after which the signals from groups of elements are "beamformed", either using analogue or digital techniques [10] or a combination of both as is the case with EMBRACE [14].

Beamforming is achieved by adding specific time delays to the signals of each individual element before summing them, which will result in the formation of a coherent beam in the required direction.

Besides being calibrated as a function of amplitude and phase, which is equivalent to the aligning of a parabolic reflector, signals in an AA can also be calibrated in terms of frequency.

An AA station consists of a number of tiles of which the beamformed signals are combined to form "station beams". The station beams are used to cover a sufficient portion of the sky for the required survey speed.

By having elements closer than  $\frac{\lambda}{2}$ , the dense AA fully samples the incoming EM signal for each polarization, which results in great performance benefits compared to other topologies. The lower frequency cut-off of the array is extended by the high level of mutual coupling between the elements,

however this results in spatial oversampling at these frequencies. As the frequency increases such that the element spacing is no longer  $\frac{\lambda}{2}$  (the array at these frequencies is therefore “sparse”), grating lobes will appear which will reduce the sensitivity of the instrument. Since the number of elements is determined by a square law of the highest “dense” frequency, the high frequency is therefore the greatest factor in the cost and power requirements of the array.

## 1.3 The Mid-Frequency Aperture Array

The development of the technology required to realise the aperture array concept in the mid-frequency range forms part of the SKA Advanced Instrumentation Program under the banner of the Mid-Frequency Aperture Array (MFAA) [15].

The technology development includes the design of the antenna elements, the amplifiers, and the hardware, firmware and software required to perform the necessary data transport and signal processing at station level [9].

A key objective of the MFAA Consortium is also to evaluate different front-end design concepts. More information on some of the different design concepts are given in Chapter 2.

In this dissertation, a dual-polarized dense dipole array (DDA) is presented as a design concept for the Mid-Frequency Aperture Array.

## 1.4 Contributions

### 1.4.1 Primary Contributions

- A single-polarized Dense Dipole Array. The design is an implementation of Wheeler’s current sheet array [11] and the design approach for broadband wire arrays introduced by Munk in [12] and [13] was used. Munk theorized that a combination of capacitances between the tips of neighbouring elements and the close proximity of the elements to one another can be exploited to increase the overall bandwidth. The DDA design uses a planar, printed structure where all the elements are printed on a single PCB layer instead of wire elements with multiple dielectric layers as presented in [16], or multiple vertically mounted PCB’s as presented in [17]. The DDA’s single-layer PCB design offers manufacturing simplicity, and allows two, co-located polarization layers to be etched on either side of the same PCB.
- A dual-polarized DDA. The single-polarized DDA was expanded to include a second, orthogonal, co-located polarization to allow for the

full set of Stokes parameters [18] to be measured. The dual-polarized connected dipole structure is in contrast with other designs ([13, 16, 17]) that offer only a single polarization.

- The design of an antenna feed that suppresses common-mode resonances commonly encountered in connected antenna arrays. This design offers a significant differential-mode bandwidth improvement to the design proposed by Cavallo et al. in [17]. It replaces the two narrow-band half-wavelength microstrip loops of the design in [17] with two symmetrical wideband microstrip-slotline transitions to cancel out common-mode signals, while differential-mode signals will still propagate through. The design is verified using both simulations and measurements of a manufactured prototype. A wide bandwidth and a CMRR > 30dB is achieved that exceeds the design specifications set out.
- The manufacture, assembly and measurement of a 1 m<sup>2</sup>, dual-polarized prototype DDA. A large, dual-polarized DDA was manufactured and both the S-parameters as well as the Embedded Element pattern were measured.

### 1.4.2 Secondary Contributions

- A method with which large quantities of multi-dimensional data can be visualized for analysis has been developed in order to conduct meaningful parameter studies.
- The use of cross-correlation functions to sort large datasets to aid in the visual analysis of multi-dimensional data.

## 1.5 Layout of the Dissertation

A literature review and brief introduction to some key concepts on which the work being presented was built is given in Chapter 2.

The development process of the single-polarized DDA, as well as the underlying theory and simulation results are presented in Chapter 3. This is followed by the expansion of the single-polarized DDA into a dual-polarized DDA in Chapter 4.

Chapter 5 presents the common-mode suppressing feed that was designed to filter out common-mode resonances native to connected antenna arrays.

Results of manufactured prototypes of both the single-polarized as well as the dual-polarized DDA's are presented in Chapter 6.

Lastly, concluding remarks and a brief introduction to the planned future work are contained in Chapter 7.

## Chapter 2

# Theoretical Framework and Literature Study

### 2.1 Introduction

This chapter discusses some important concepts that are applicable to the work presented in this dissertation. In addition to that, more in-depth background knowledge in the SKA Mid-Frequency Aperture Array (MFAA) is provided and other candidate topologies for the MFAA are introduced.

Section 2.2 introduces the Infinite Current Sheet Array concept formulated by Wheeler. In Section 2.3, various modelling approaches for large antenna arrays are discussed. Section 2.4 gives an overview of some performance metrics applicable to antenna arrays used for radio astronomy. Section 2.5 introduces the other candidate topologies for MFAA, and Section 2.6 concludes.

### 2.2 The Infinite Current Sheet Concept

The more conventional approach to large phased array design is to select a single antenna element that demonstrates the preferred characteristics and to then arrange the desired number of elements in some sort of array configuration. The problem with this approach is that the characteristic impedance of the antenna varies with scan angle as a result of mutual coupling.

Another method of large phased array design is the infinite Current Sheet Array (CSA) concept introduced by Wheeler [11]. The array design procedure is then approached from the other end - an infinite planar structure of interconnected electric current sources is designed and then scaled down to a finite structure. By following this approach, the CSA utilises the mutual coupling between elements, instead of attempting to reduce it.

Wheeler conceptualizes a hypothetical phased array formed by an infinite current sheet. The active impedance of the array then only includes the radiation resistance that varies with scan angle and no reactive component.

There are already a few phased array structures used in radio astronomy that are implementations of the CSA, including the Checkerboard Array [19, 20], which is the phased array feed (PAF) used on the Australian SKA Pathfinder (ASKAP), and the Octagonal Ring Antenna (ORA) which is an MFAA candidate topology. The ORA is discussed in further detail in Section 2.5.2.

## 2.3 Full-Wave and Reduced-Order Modelling Methodologies for Dense Aperture Arrays

This section presents a review of full-wave and reduced-order modelling techniques for large, dense antenna arrays. The aim of this review is to identify efficient and sufficiently accurate means of modelling various parameters of aperture arrays for array design purposes.

### 2.3.1 Reduced-Order Modelling of a Microstrip-Fed Vivaldi Array

A method to analyse microstrip-fed Vivaldi Arrays by combining electrodynamic and electrostatic field models was presented by Maaskant et al. in [21]. This method makes use of the Characteristic Basis Function Method (CBFM) to model the currents on the antenna conductors while the wide-band microstrip feeds are modelled separately using quasi-static circuit models.

For this study, models were developed that implemented this method of decomposition and make use the Method-of-Moments (MoM) solver of the commercial software FEKO to model the metal structure of the antenna elements. The results are then compared to a full-wave MoM analysis of the same structure with an incorporated microstrip feed.

The comparison between of a full-wave MoM simulation and the decomposed model of the reflection coefficient of a single Vivaldi Element is shown in Figure 2.1. The percentage error between the two results is depicted by Figure 2.2.

It can be seen that the results of the decomposed model closely tracks that of the full-wave simulation. Further tests have confirmed that the slightly larger deviation close to 1 GHz can be attributed to a resonance effect created in the slotline. Since the Vivaldi element is effectively the ground



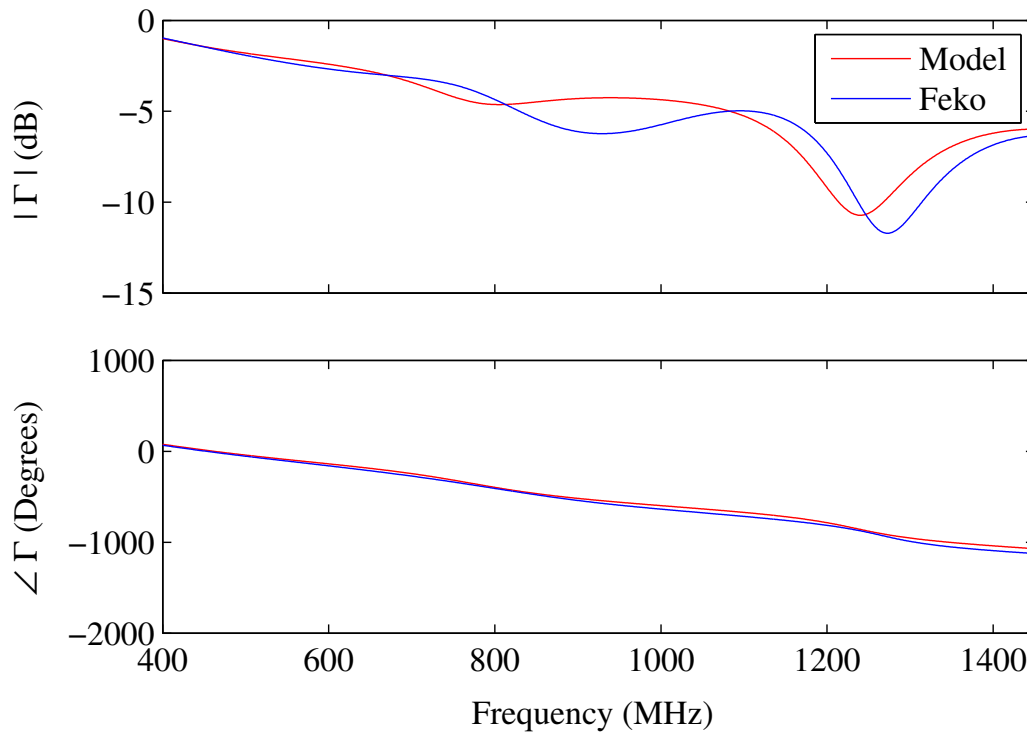


Figure 2.1: Magnitude and Phase of a single Vivaldi element for a reduced-order compared to a full-wave MoM solution using FEKO

plane of the microstrip feed, these cut-outs for the slot and the cavity result in a slightly enhanced approximation error with the quasi-static model.

### 2.3.2 Infinite Array Analysis

The dense aperture array topologies being investigated are all large, regular structures. Modelling the structures using infinite array approximations by means of periodic boundary conditions is therefore also an attractive option.

The Octagonal Ring Antenna (see Section 2.5.2) is a realisation of the CSA with dual polarization. Since the design is approximated as an infinite periodic structure, Floquet analysis can be applied to analyse this structure [22]. This method uses a series of orthogonal functions to represent the radiating fields of a periodic structure. The signal series of the source is decomposed into  $TE_{zmn}$  and  $TM_{zmn}$  modal sources which in turn can be used to calculate the electromagnetic field from each source. This approach has been successfully used to design aperture arrays [1, 23, 24].

### 2.3.3 Domain Green's Function Method

The Domain Green's Function Method (DGFM) approach to the analysis of large, phased-steered antenna arrays is a deviation from the infinite array

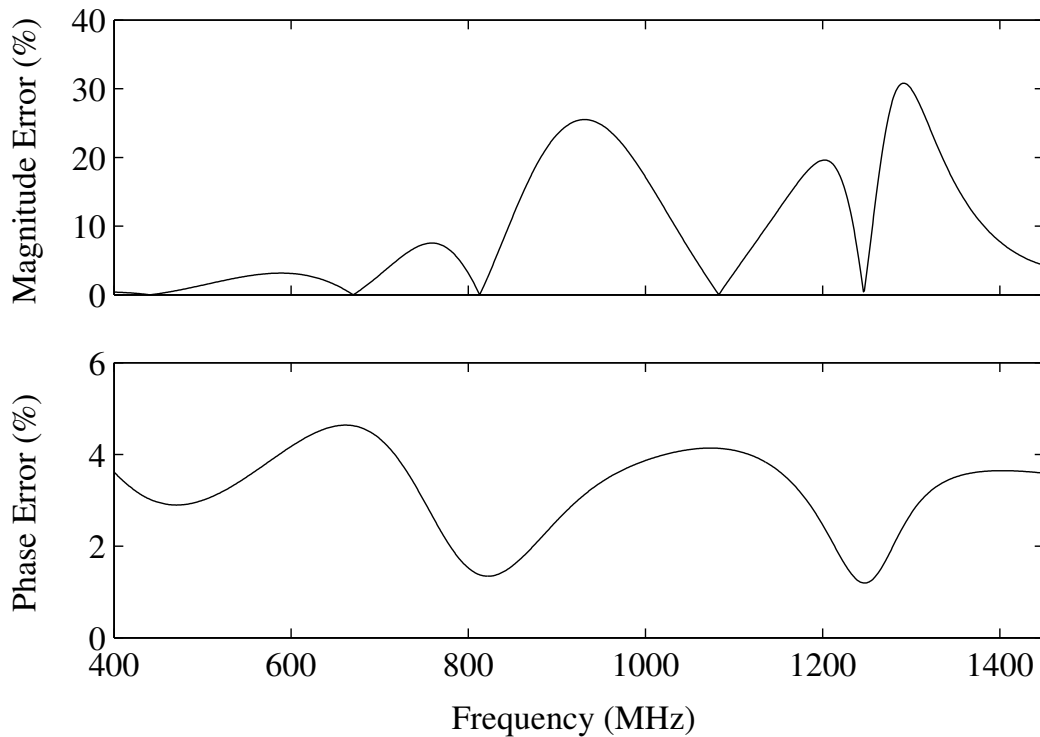


Figure 2.2: The percentage error between the reduced-order and the full-wave solution

solution and provides a solution that is both time- and memory efficient [25].

It is assumed that the current on each element or subarray is identical except for a complex scaling value. This approach results in the compression of the impedance matrix to obtain scan-impedance matrices, which will in turn account for mutual coupling between active elements [26].

The CBFM-Enhanced DGFM has proved to offer dramatic improvements in both runtime as well as memory usage for disjoint arrays [26]; however, this technique has not been implemented for use in connected arrays.

## 2.4 MFAA Performance Requirements

Due to the investigative nature of the MFAA program, a comprehensive system requirements specification is yet to be determined at this stage. In the absence of a fixed MFAA system specification, some key front-end performance characteristics has been identified and are elaborated upon in below.

The performance characteristics listed here are in addition to the standard performance criteria used for antenna design.

### 2.4.1 Cross-Polarization Performance

For polarization imaging in Radio Astronomy, it is customary to use two antenna feeds which are co-located and have identical gains and beam patterns but are placed in such a way that their polarizations are nearly orthogonal across the entire FoV [2].

With good knowledge of the antenna beam and polarization characteristics, it is then possible to accurately reconstruct the polarizations of signals from objects inside the main beam during post-processing [27].

McGrath et al. [28] studied the polarization properties of scanning arrays and came to the following three important conclusions:

1. The main beam polarization of an electronically steered array is the same as that of the embedded element pattern at broadside. The polarization characteristics of the array will differ from that of an isolated element due to the additional current modes excited on the radiating structure as a result of mutual coupling.
2. The polarization state of an electronically steered array will change with scan angle under the majority of circumstances. The change is affected by the radiator type, array configuration and scan angle.
3. The intended application of the array will determine whether the difference in polarization as a function of scan angle will imply an increase in polarization loss. The definition of the term “Cross-Polarization” will therefore depend on the application.

As noted above, the polarization characteristics of the antennas are not consistent across the entire FoV. Furthermore, if the actual polarization characteristics differ from those assumed in the correction procedure during post-processing, it can result in incorrectly identifying an unpolarized source as a polarized one.

Practical self-calibration algorithms have proven to be effective in dealing with polarization, but the data needed to make the corrections needs a high accuracy.

A good understanding, and more importantly, an accurate model of the polarization behaviour of the antenna array across the entire FoV is therefore a key requirement for Aperture Arrays for Radio Astronomy.

In this document, all references made to cross-polarization performance are in accordance with Ludwig’s III definition of cross-polarization [29].

### 2.4.2 Noise Performance

As shown in Chapter 1, the system noise temperature is critical to the survey speed of and sensitivity of radio telescopes. However,  $T_{\text{sys}}$  is not a straightforward parameter to determine in a tightly coupled antenna array.

The computational complexity of the problem make it impractical to attempt to determine the noise contribution due to dielectric and conduction losses using the computational methods that are currently available.

In addition to that, noise coupled from neighbouring elements also contribute to the total system noise temperature, necessitating proper noise matching of the system [24, 30–39]. The phenomenon of noise coupling is elaborated upon below and is a summary of the formulation done by Maaskant and Woestenburg in [32].

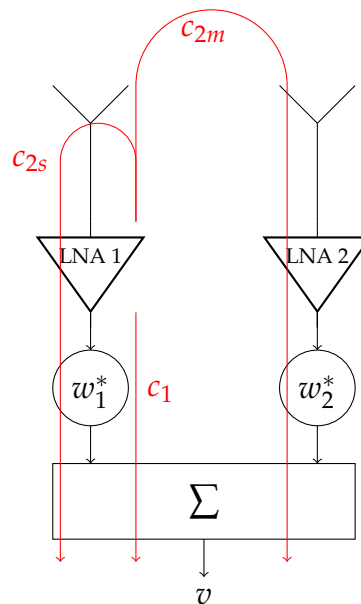


Figure 2.3: Propagation paths of noise waves that emanate from an LNA when connected to an antenna in a mutually coupled array.

Figure 2.3 illustrates the total noise contribution from a single LNA (LNA 1 in the figure) in a two element antenna array. From the figure, the noise contributions can be summarized as follows:

- $c_1$ : The correlated noise waves that emanate from the output of LNA 1.
- $c_{2s}$ : The correlated noise waves that emanate from the input of LNA 1 which are reflected back to LNA 1 as a result of the impedance mismatch between the antenna and LNA, and are received and amplified by element 1.
- $c_{2m}$ : The correlated noise waves that emanate from the input of LNA 1 which are received and amplified by element 2 as a result of mutual coupling.

The total noise contribution is therefore the sum of these three contributions:

$$\begin{aligned}
c_{\text{tot}} &= c_1 + c_{2s} + c_{2m} \\
&= c_1 + c_2 S_{11}^{\text{ant}} S_{21}^{\text{LNA}} + c_2 S_{21}^{\text{ant}} S_{21}^{\text{LNA}} e^{j\varphi} \\
&= c_1 + c_2 S_{21}^{\text{LNA}} \left( S_{11}^{\text{ant}} + S_{21}^{\text{ant}} e^{j\varphi} \right) \\
&= c_1 + c_2 S_{21}^{\text{LNA}} \Gamma_{\text{act}}^1(\varphi), \tag{2.4.1}
\end{aligned}$$

where  $\Gamma_{\text{act}}^1(\varphi) = S_{11}^{\text{ant}} + S_{21}^{\text{ant}} e^{j\varphi}$  and represents the active reflection coefficient of antenna 1 for a given scan angle  $\varphi$ . This active reflection coefficient would therefore also be a function of the beamforming weights  $w_1$  and  $w_2$ .

From this formulation it is clear the the total noise contribution of the LNA's in a tightly coupled antenna array is a function of the noise parameters of the LNA, the S-parameters of both the array and the LNA as well as the beamforming weights.

The process of optimising the noise performance of the array in order to minimise the noise contribution due to noise coupling is referred to as "noise matching" and involves matching the amplifiers to the active reflection coefficients of the array [32,33].

## 2.5 Introduction to other MFAA Topologies

### 2.5.1 Vivaldi Array

Dense aperture arrays as described in Section 1.2 can be made up of elements that offer good impedance match and wide radiation pattern across the entire band of operation. Since the Vivaldi Antenna meet these requirements and is also a compact element which assists in achieving a dense arrangement of the antenna elements, it has been identified as an ideal candidate for AA applications early on in AA feasibility studies.

During the last 3 decades, a number of studies have been done in order to gain understanding of the fundamental operation of these antennas [40–43], but only relatively recent advances in numerical simulation techniques have made it possible to begin to realise the full potential of the Vivaldi as a phased array element [21,44–46]. This has in turn resulted in successful use of the Vivaldi in AA Demonstrator Projects such as THEA and EMBRACE.

#### 2.5.1.1 THEA

THEA, or "Thousand Element Array" was developed by the Netherlands Foundation of Research in Astronomy (NFRA). It consists of  $16 \times 1 m^2$  active tiles which contain 64 single polarization Vivaldi antennas each and the operating frequency is 600 – 1700 MHz. Since development started in

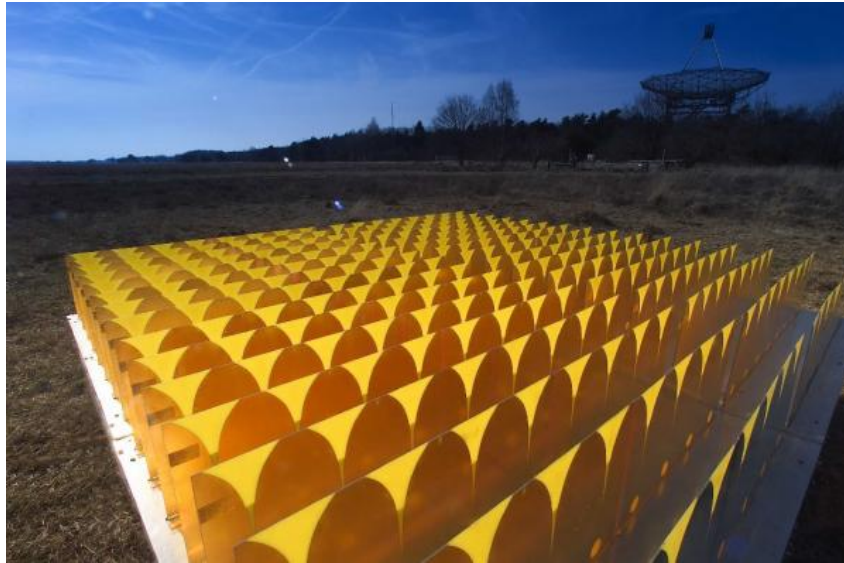


Figure 2.4: Four THEA Tiles [47]



Figure 2.5: The aluminium vivaldi elements at one of the EMBRACE stations

2000, the project has successfully demonstrated the multi-beam capabilities of AAs [47,48].

### 2.5.1.2 EMBRACE

EMBRACE, or “Electronic Multi Beam Radio Astronomy ConcEpt” was developed to demonstrate various design concepts for phased array technology in radio astronomy.

EMBRACE consists of two stations, one in Nancay, France and the other one in the Netherlands on the same site as the Westerbork Synthesis Radio Telescope (WSRT).

The array consists of Vivaldi elements organized in tiles of approximately  $1 \text{ m}^2$ . Each tile consists of 144 antenna elements in dual polarization, al-



though EMBRACE is only operational in a single linear polarization. The operational frequency is 500 – 1500 MHz [7,9,14,47].

## 2.5.2 Octagonal Ring Antenna

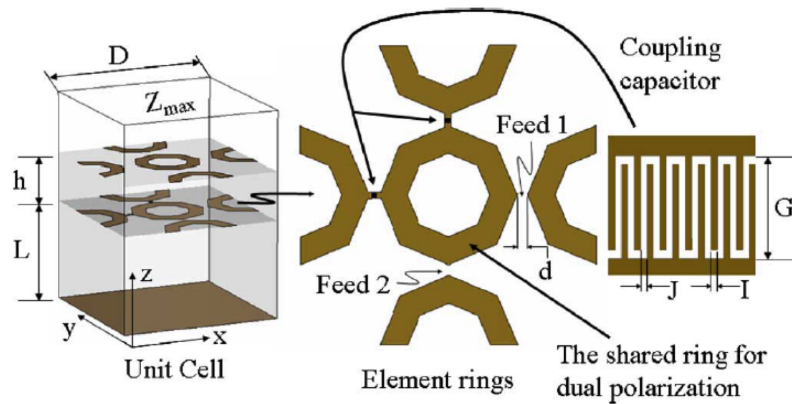


Figure 2.6: Geometry of two-dimensional ORA unit cell [1]

The Octagonal Ring Antenna was proposed as a low profile, high bandwidth structure that does not use multiple dielectric layers in order to stabilize the impedance bandwidth [1,16,49]. Instead a metamaterial superstrate layer is formed by placing a layer of conductive rings above the element layer.

Figure 2.6 depicts a model of the unit cell of the ORA Array. The model consists of an active radiating layer, two conducting layers and a passive superstrate layer made of a meta material that improves the impedance-matching over wide scan angles. Dual polarization is achieved by positioning three rings orthogonally, with one ring shared by the neighbouring orthogonal element.

The ORA demonstrated a stable cross polarization within a scan range of  $\pm 45^\circ$  and a bandwidth 3.3:1 [1].

## 2.5.3 Log-Periodic Sparse Aperture Array

In contrast to the other MFAA topologies, the Log-Periodic Sparse Array (LPDA) design, under development at Cavendish Laboratories at the University of Cambridge, proposes a sparse rather than dense arrangement of the antenna elements. It is argued that when using a sparse array, the sensitivity at the lower frequencies is maximized by maximizing the effective aperture of the array without changing the system noise temperature [50,51]. A random arrangement of the elements would ensure that grating lobes and mutual coupling effects are cancelled out [52,53].

The LPDA design is a miniaturization of the SKA Log Periodic Antenna (SKALA) element that has been investigated for the Low Frequency Aperture Array (LFAA) of the SKA [50]. A FEKO [54] model and dimensions of the LPDA can be seen in Figure 2.7.

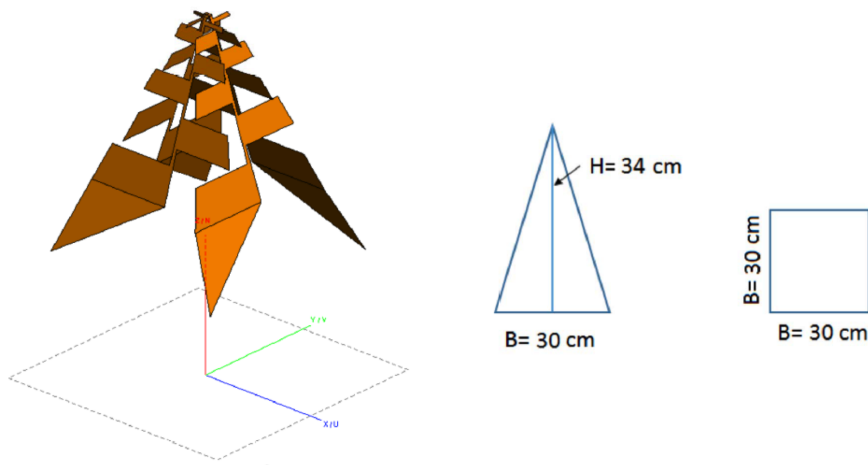


Figure 2.7: FEKO model and dimensions of an LPDA element for MFAA [53]

Current results for the LPDA indicate a bandwidth of roughly 5:1.

## 2.6 Conclusion

This chapter discussed some key concepts on the design and performance evaluation of aperture arrays for radio astronomy. The other candidate topologies for Mid-Frequency Aperture Arrays were also introduced and briefly discussed.

The next chapter delves into the detail of a single-polarized Dense Dipole Array, which forms an important theoretical foundation for the work presented in this dissertation.



## Chapter 3

# The Basic Dense Dipole Array

### 3.1 Introduction

The concept of a simple dipole aperture array for radio astronomy was conceived by J.E. Noordam and J.E.E. Voûte in 1994 in a report entitled *Design Aspects of a Tile Telescope: A possible approach to a Square Kilometre Array Interferometer (SKAI)* [55].

In 1994, the radio astronomy community was beginning to come to the realisation that for certain areas of science, a very large collecting area - a square kilometre - will be required. The report by Noordam and Voûte was therefore written in an attempt to stimulate discussion of the technical and cost implications the development of such a telescope would have.

The following two **Golden Rules** for building and operating the new telescope within a reasonable budget were stated in the report:

1. **No moving Parts.** They are expensive to build, and require too much maintenance.
2. **Keep it flat, i.e. 2-dimensional.** Large 3-dimensional structures require extra digging or building, and are sensitive to wind and gravity.

A concept system consisting of a grid of dipole elements connected through multi-purpose switches was also presented in the report. The multi-purpose switches were intended to create either a short-circuit, open-circuit, capacitance or inductance by means of an electronic signal; the idea being that the topology of the antennas can be changed as needed in order to accommodate a large bandwidth.

The large dipole grid was divided up into  $1\text{m} \times 1\text{m}$  tiles. Each tile would contain the LNA's and electronics required to operate the switches and would then be sealed inside a rubber material in order to make the tiles waterproof. Each tile would have only a single connector at the back. These tiles were therefore intended to be structures that can be mass produced, simply

placed in position and connected to the back-end. Maintenance would consist of simply replacing faulty tiles with new ones. Due to the appearance these antennas were intended to have, the concept antenna was called the “Bathmat” or “Tile Telescope” antenna.

The development of the Dense Dipole Array (DDA) was therefore conceived as an attempt to realise the “Bathmat” concept in collaboration with one of the original authors of the report, J.E. Noordam.

While the use of dipole elements offers a significant simplification of the manufacturing process, the basic dipole element does not offer large enough instantaneous bandwidth. Although the multi-purpose switches mentioned above in theory offered a solution to the bandwidth problem, in reality it proved a challenge to find suitable switches.

Another approach was therefore required to enhance the native bandwidth of a dipole element. This chapter provides details on the theory and the development of a basic wide-band dipole array with single polarization.

In Section 3.2 the theoretical background and basic physics of the DDA is discussed. As an expansion of the theory, Section 3.3 gives the details of the parameter study that was done in order to gain insight into how different parameters affect the performance of the DDA. The optimisation of the design is discussed in Section 3.4, the performance results of a preliminary infinite array are given in Section 3.5 and Section 3.6 concludes.

## 3.2 Theoretical Background

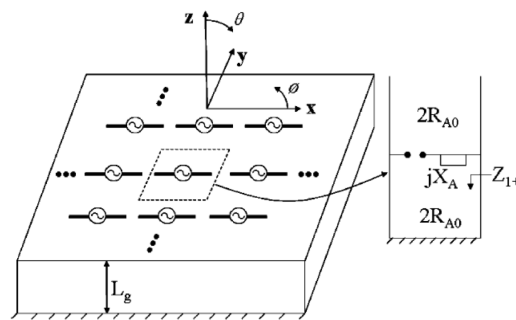


Figure 3.1: An infinite dipole array backed by a ground plane [1]

Figure 3.1 depicts an equivalent circuit model of an infinite array of dipoles backed by a ground plane. This model was developed by Munk in [1] and [13]. The impedance as seen at the terminals of an element in the array can therefore be given by  $Z_A = 2R_{A0} + jX_A$ , where

- $R_{A0}$  is the radiation resistance of the same array when no ground plane is present, and

- $jX_A$  is the reactive part of the antenna impedance and is associated with the evanescent waves above and below the antenna elements.

In the array shown in the figure, each source experiences an inductance effect. This inductance is mostly introduced by the ground plane and, to a lesser extent, by the elements themselves. This inductance can be compensated for by inserting series capacitances between the tips of neighbouring elements resulting in a purely resistive antenna impedance which imitates the infinite current sheet array introduced by Wheeler [11]. Now the antenna impedance is a resistive value which varies only as a function of scan angle.

The series capacitances mentioned above can either be realised by inserting physical capacitors or by increasing the inherent capacitance present between neighbouring elements by careful placement of the array elements.

The array configuration in this project was based on the “gangbuster surface” mentioned in [13], with the exception that the elements are not tilted. A visualisation of this configuration with single polarization can be seen in Figure 3.2.

Figure 3.3 illustrates the basic current distribution on 3 elements of a linear DDA. Assuming the length of the elements is a half-wavelength, the currents on all the elements will flow in the same direction at any given time.

Refer now to element 2 on the figure. Due to the close proximity of the elements, the total current induced on the conductors in the vicinity of element 2 as a result of the incoming plane wave consists of a combination of the current on the element itself and the current on the sections of the neighbouring elements that overlap with element 2.

Since the total power incident on the section surrounding element 2 is still the same as it would have been had the element been isolated, the current induced on the conductors in the vicinity of element 2 is still equal to that of an isolated dipole element. The current seen at the terminals of element 2,  $I_t$  is therefore approximately half that of an isolated dipole (this approximation depends on the level of overlap between neighbouring elements):

$$I_t \approx \frac{I_d}{2}. \quad (3.2.1)$$

The input power of an isolated dipole is given by

$$S_i = \frac{1}{2} I_d^2 Z_d, \quad (3.2.2)$$

where  $Z_d$  is the impedance of an isolated dipole element. Given that the input power delivered to an isolated dipole is identical to that of an element

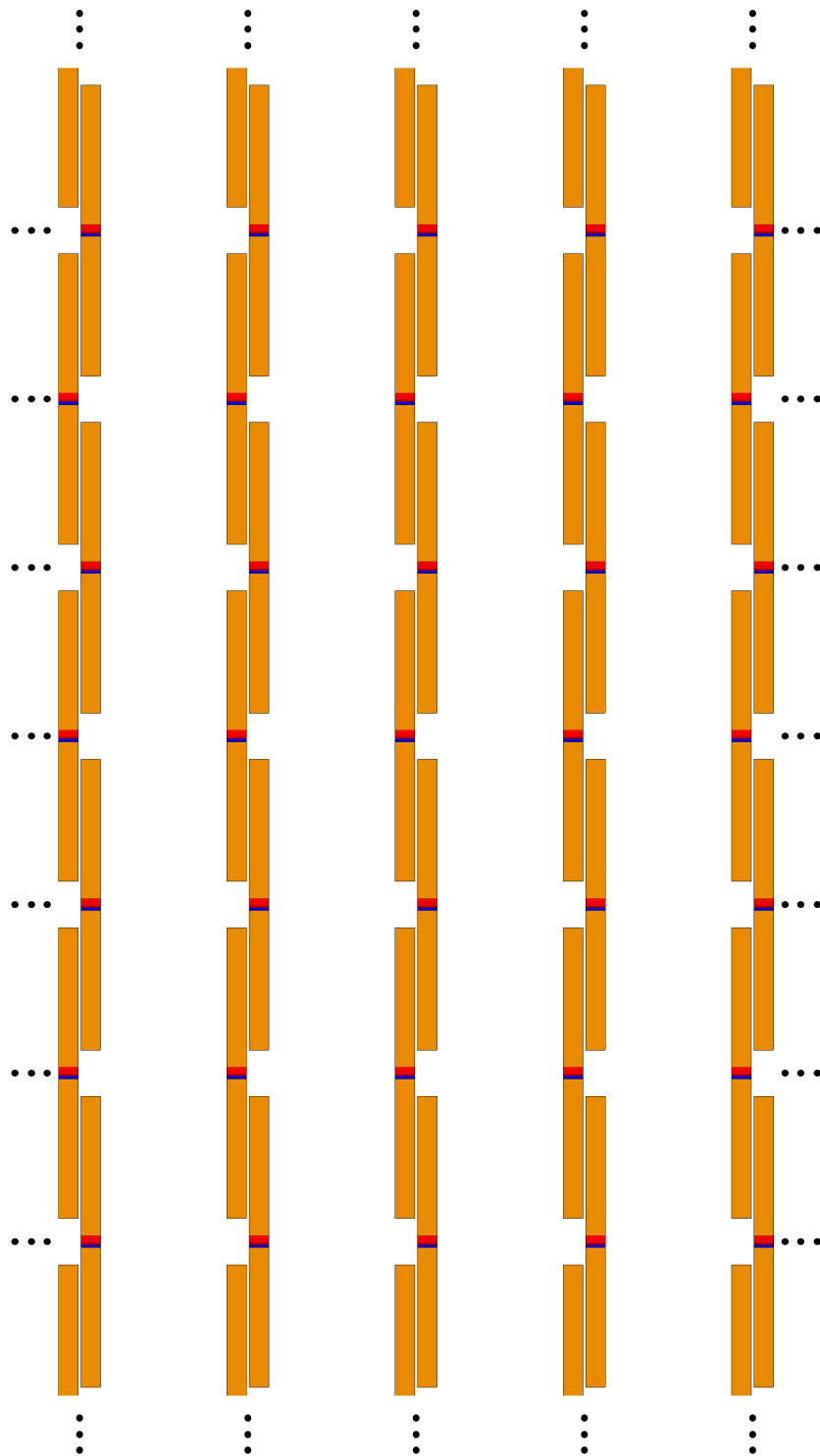


Figure 3.2: Visualisation of a DDA structure with single polarizations

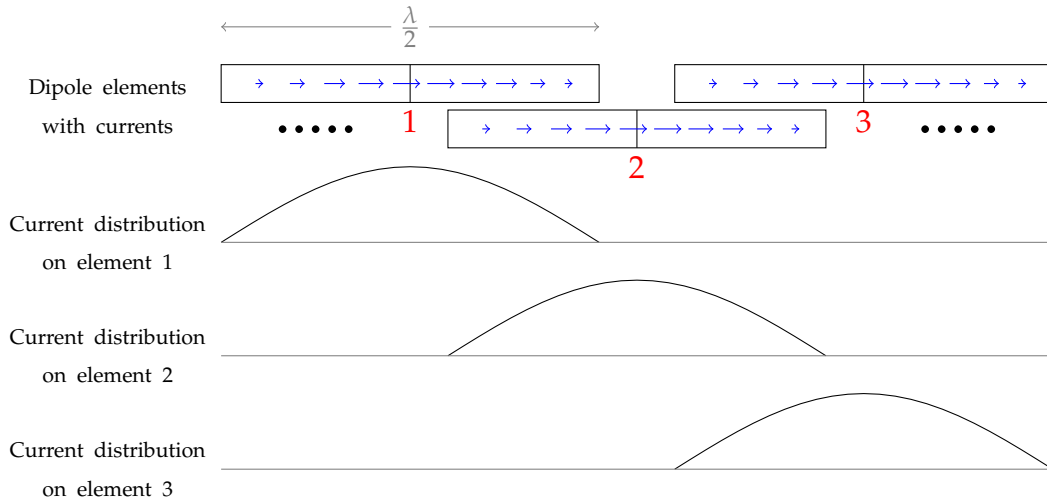


Figure 3.3: Basic current distribution on a linear DDA

in the array,

$$S_i = \frac{1}{2} I_t^2 Z_{in}, \quad (3.2.3)$$

where  $Z_{in}$  is the input impedance of an element in the array. Equations 3.2.1 - 3.2.3 can then be used to find the characteristic impedance of an element in a DDA:

$$\frac{1}{2} I_t^2 Z_{in} = \frac{1}{2} I_d^2 Z_d \quad (3.2.4)$$

$$Z_{in} = \frac{I_d^2}{I_t^2} Z_d \quad (3.2.5)$$

$$Z_{in} \approx \frac{4I_t^2}{I_t^2} Z_d \quad (3.2.6)$$

$$Z_{in} \approx 4Z_d = 300 \Omega \quad (3.2.7)$$

This approach is similar to that used in [56] to determine the characteristic impedance of a folded dipole.

The next section contains the details of the parameter study that was done in order to gain insight into how different parameters affect the performance of the array.

### 3.3 Parameter Study

The aim of this study was to gain understanding of the underlying physics of the DDA and how variation of the different parameters associated with it affects its performance, particularly the impedance bandwidth of the array.

Simulation of an infinite DDA was done in Feko [57] using the periodic boundary condition functionality. For each set of parameters, the active reflection coefficient at broadside was calculated.

An investigation of the impedance behaviour under different scan angles is addressed in Section 3.5.1.2.

Table 3.1 along with Figure 3.4 lists and gives a brief description of the relevant parameters for this study and the range within which they were varied for the study in millimetres.

Table 3.1: Parameters of the DDA

Parameter	Description	Range (mm)
Height	Height of the array above the ground plane.	50 → 150
Length	Length of a dipole element.	100 → 150
Pitch	Spacing between elements.	71 → 138
Tip Gap	Gap between the tips of neighbouring, overlapping elements.	0.3 → 1.5
Width	Width of a dipole element.	3 → 5

#### 3.3.1 Initial Parameter Study

For the initial study, it was decided to first examine the capacitance induced between the tips of neighbouring elements and to see how different methods of adjusting it will affect the bandwidth performance of the array. The spacing between the elements and the gap between the tips was therefore varied, while the height parameter and element length was fixed at  $\frac{\lambda_0}{4}$  and  $\frac{\lambda_0}{2}$  respectively, where  $\lambda_0$  is the wavelength at the centre frequency. The centre frequency was chosen as  $f_0 = 1$  GHz which is the centre frequency of the 500 – 1500 MHz band for which EMBRACE was designed. The series inductance created by the antenna elements themselves were also investigated. This was done by adjusting the width of the elements.

The effect of varying the height above the ground plane as well as the element length is discussed later on.

Figures 3.5 to 3.7 illustrate the results of a tip-capacitance parameter sweep as explained above.

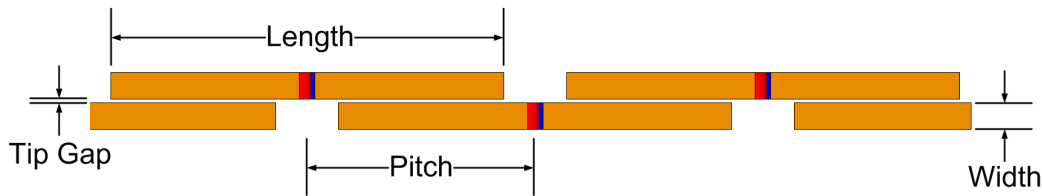


Figure 3.4: Parameters of the DDA

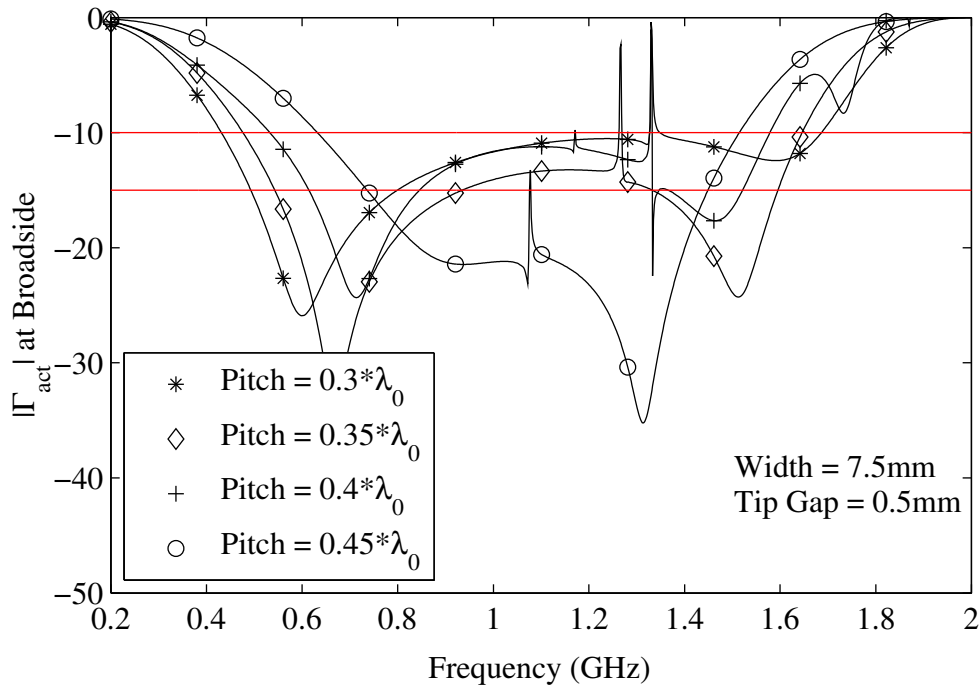


Figure 3.5: Active reflection coefficient at broadside for different pitch values. Element width = 7.5 mm and Tip Gap = 0.5 mm.

It can be seen that increasing the capacitance by either increasing the overlap between elements or decreasing the gap between the tips effectively widens the bandwidth of the array.

The effect of adjusting the series inductance by varying the width of the element can be seen in Figures 3.8 and 3.1.

In Figure 3.8 the element width was increased to 10 mm for the same experiment. The result was surprising in that the increase in element width did not have the effect of increasing the bandwidth as would be expected. Instead it is believed that the effect of adjusting the bandwidth of the element by changing its width negated the compensation achieved by the tip capacitance. This conclusion is further supported by the results in Figure 3.9, where the inter-element spacing and tip gap is fixed at  $0.3\lambda_0$  and 1 mm

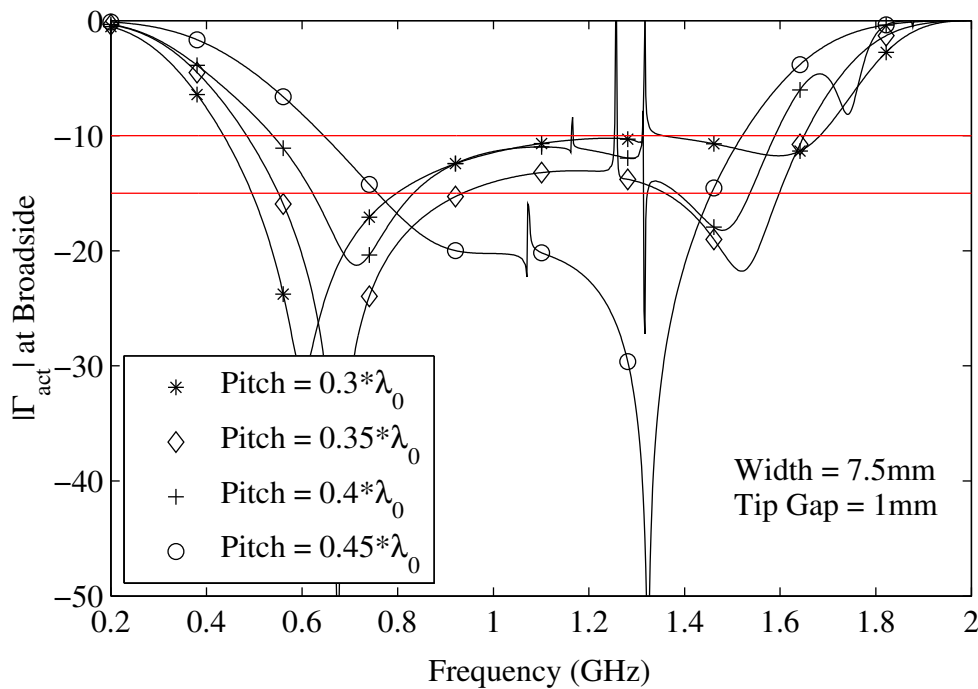


Figure 3.6: Active reflection coefficient at broadside for different element spacings. Element width = 7.5 mm and Tip Gap = 1 mm.

respectively while the element width is adjusted.

From this figure it is clear that adjusting the element width in any one direction does not result in a proportional increase or decrease in bandwidth. It is therefore suggested that there exists an optimal combination of element width, tip-gap and pitch. This realisation gave rise to a more extensive parameter study being performed.

In all the results shown in Figures 3.5 to 3.9, there is a resonance present in the upper part of the pass-band. This resonance is associated with a common-mode current being induced between the ports of neighbouring elements as is explained below.

### In-band Resonances:

Differential- and common-mode properties of balanced networks can be determined by using two single-ended ports to represent each differential (symmetrical) port [58, 59]. This is illustrated in Figure 3.11. The mixed-mode applied- and reflected signals can therefore be written as a function of the single-ended applied- and reflected signals as follows:



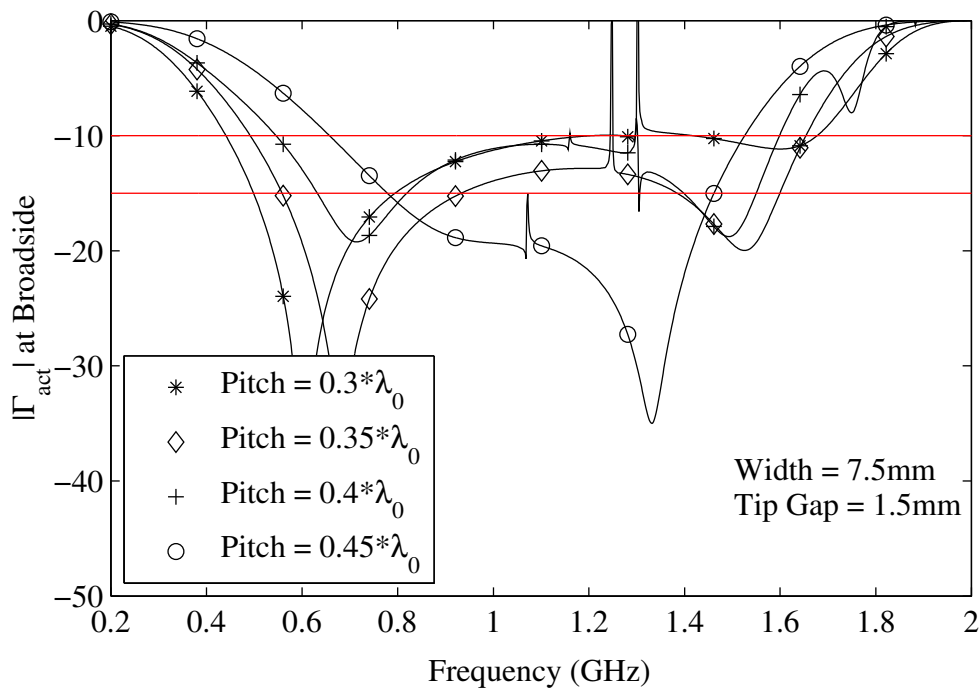


Figure 3.7: Active reflection coefficient at broadside for different element spacings. Element width = 7.5 mm and Tip Gap = 1.5 mm.

$$a_d = \frac{1}{\sqrt{2}} (a_1 - a_2), \quad (3.3.1)$$

$$a_c = \frac{1}{\sqrt{2}} (a_1 + a_2), \quad (3.3.2)$$

$$b_d = \frac{1}{\sqrt{2}} (b_1 - b_2), \quad (3.3.3)$$

$$b_c = \frac{1}{\sqrt{2}} (b_1 + b_2). \quad (3.3.4)$$

The reflection coefficient when a differential-mode signal is applied, but a common-mode signal is reflected can then be expressed as:

$$\Gamma_{cd} = \frac{b_1 + b_2}{a_1 - a_2}. \quad (3.3.5)$$

Also, generally:

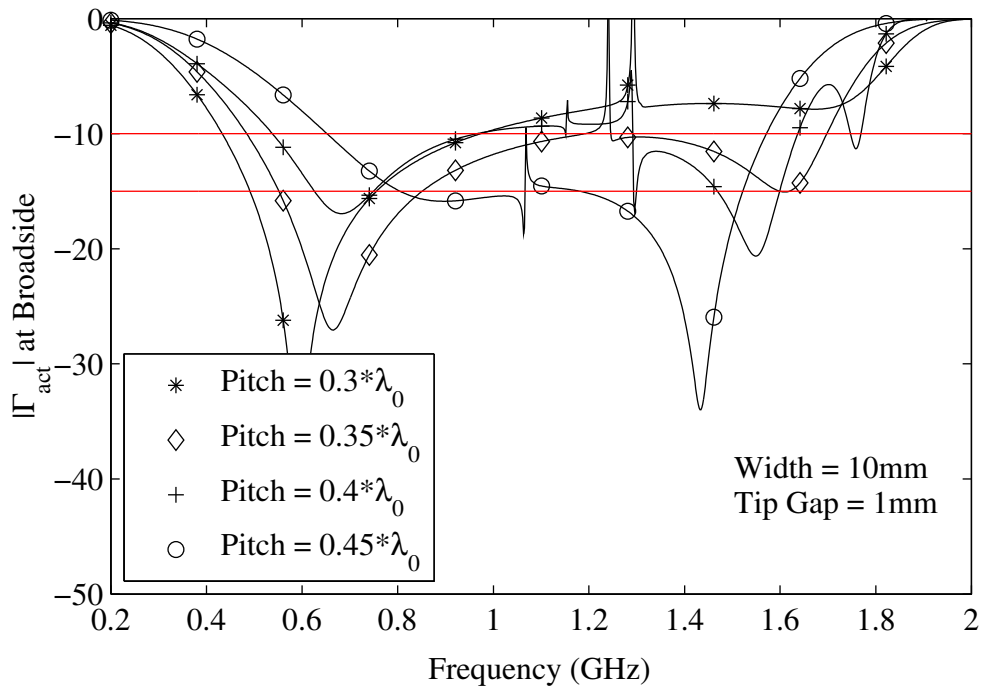


Figure 3.8: Active reflection coefficient at broadside for different element spacings. Element width = 10 mm and Tip Gap = 1 mm.

$$\Gamma = \frac{b}{a} \quad (3.3.6)$$

$$\Gamma = \frac{Z_L - Z_0}{Z_L + Z_0} \quad (3.3.7)$$

so

$$b = a \frac{Z_L - Z_0}{Z_L + Z_0}. \quad (3.3.8)$$

When a perfect differential-mode signal is applied between ports 1 and 2:

$$\begin{aligned} a_1 &= -a_2 \\ \therefore a_1 - a_2 &= 2a_1. \end{aligned} \quad (3.3.9)$$

If there was no common-mode reflection when the differential-mode signal was applied:

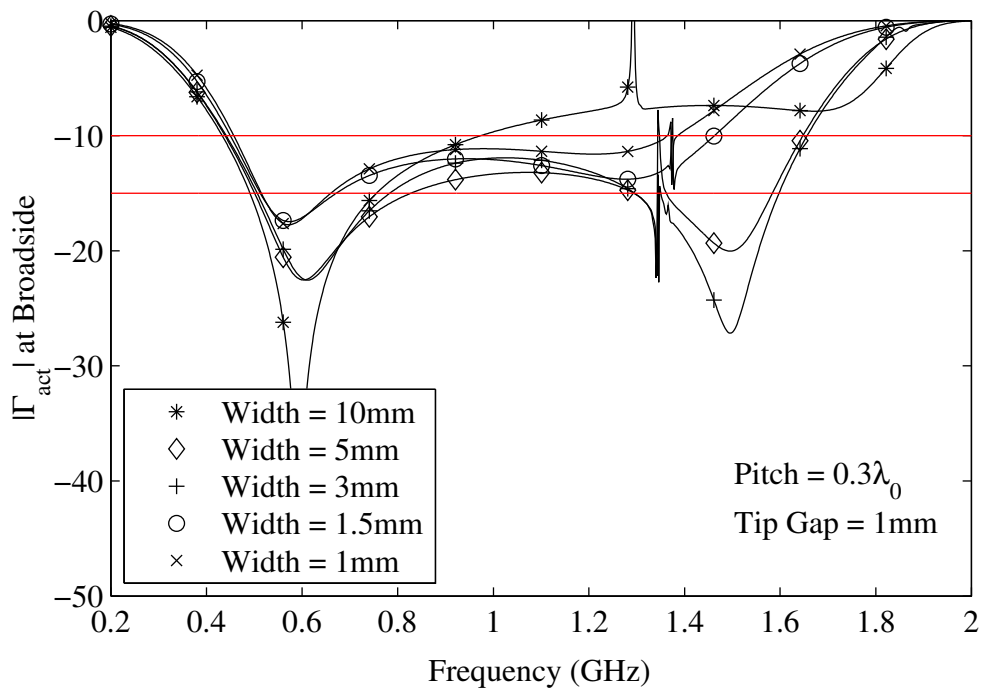


Figure 3.9: Active reflection coefficient at broadside for different element spacings. Element width = 10 mm and Tip Gap = 1 mm.

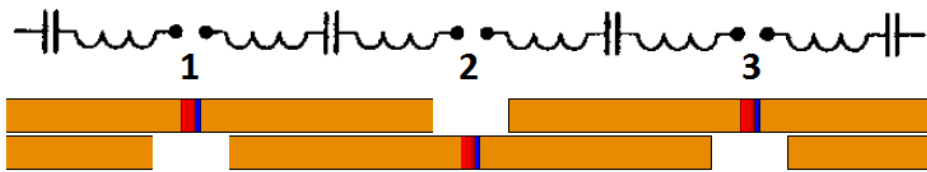


Figure 3.10: Equivalent Circuit

$$\Gamma_{cd} = 0$$

$$\frac{b_1 + b_2}{a_1 - a_2} = 0$$

$$\therefore b_1 + b_2 = 0 \quad (3.3.10)$$

$$\therefore b_1 = -b_2 \quad (3.3.11)$$

Equations 3.3.6 to 3.3.11 now yields:

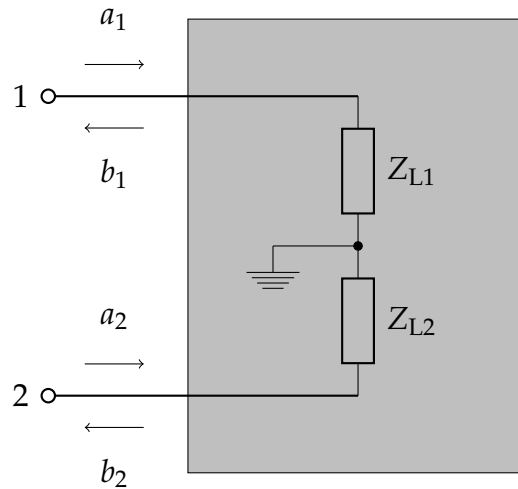


Figure 3.11: Single-Ended 2-port DUT

$$\Gamma_{cd} = \frac{a_1 \frac{Z_{L1} - Z_0}{Z_{L1} + Z_0} - a_1 \frac{Z_{L2} - Z_0}{Z_{L2} + Z_0}}{2a_1} = 0 \quad (3.3.12)$$

$$0 = \frac{Z_{L1} - Z_0}{Z_{L1} + Z_0} - \frac{Z_{L2} - Z_0}{Z_{L2} + Z_0} \quad (3.3.13)$$

$$0 = \frac{2Z_0 (Z_{L1} - Z_{L2})}{(Z_{L1} + Z_0) (Z_{L2} + Z_0)} \quad (3.3.14)$$

From Equation 3.3.14 it follows that in order for there to be no common-mode reflection from an applied differential-mode signal,

$$Z_{L1} - Z_{L2} = 0. \quad (3.3.15)$$

Should  $Z_{L1} - Z_{L2} \neq 0$ , a common-mode reflection will result from a differential-mode signal.

This phenomenon is displayed in Figure 3.12. In the figure,  $|\Delta Z| = |Z_{L1} - Z_{L2}|$ , where  $Z_{L1}$  and  $Z_{L2}$  are single-ended port impedances of two adjoining array elements when a model of the DDA is fed via two back-to-back ports. It can be seen that at the position of the resonance, the difference between  $Z_{L1}$  and  $Z_{L2}$  is non-zero. From the derivation above, this implies that the resonance in the active reflection coefficient can be attributed to the induction of common-mode currents between two adjoining elements.

The frequency at which the resonance occurs is a function of path length and phase difference between two adjoining ports. Chapter 5 discusses this

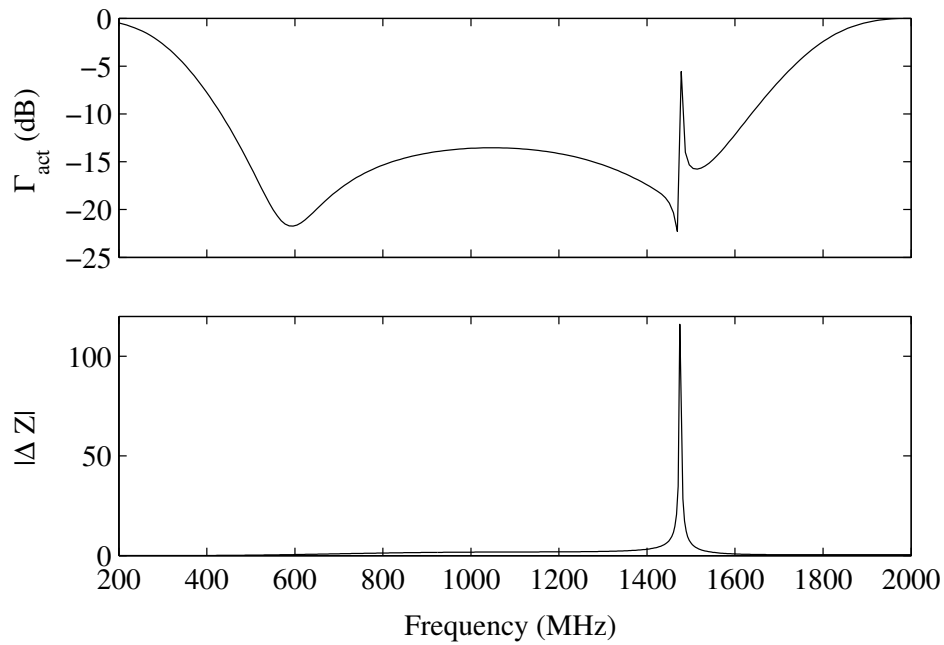


Figure 3.12: Active reflection coefficient vs difference between single-ended port impedances.

phenomenon in more detail and proposes a method that can be used to suppress the common-mode resonance.

### 3.3.2 Full Parameter Study

For the full parameter study, the parameters were varied as indicated in Table 3.1. The full array of raw results are given in Figure 3.13. On the figure, the  $z$ -axis represents the magnitude of the active reflection coefficient at broadside in dB, the  $y$ -axis represents the frequency in GHz, and the  $x$ -axis represents the index number of the dataset. Each dataset corresponds a particular set of parameter values.

Although the surface plot offers a good overview of the full dataset, it is still difficult to use it to draw conclusions from the parameter sweep. Figure 3.14 offers a better view of the data. The top figure is a top-view of the surface plot in Figure 3.13. For simplicity It was decided to use 3 colour levels as indicated in the legend of the figure. Each colour represents either data where  $\Gamma_{\text{act}} < -15$  dB,  $-10$  dB  $< \Gamma_{\text{act}} < -15$  dB, or  $\Gamma_{\text{act}} > -10$  dB.

The other figures show the value of each of the parameters corresponding to the data in the top figure.

Close observation of this representation of the raw parameter sweep results indicated that it might be possible to sort the  $\Gamma_{\text{act}}$  data in a way that a coherent picture of the data is formed when plotting it on a surface plot. It

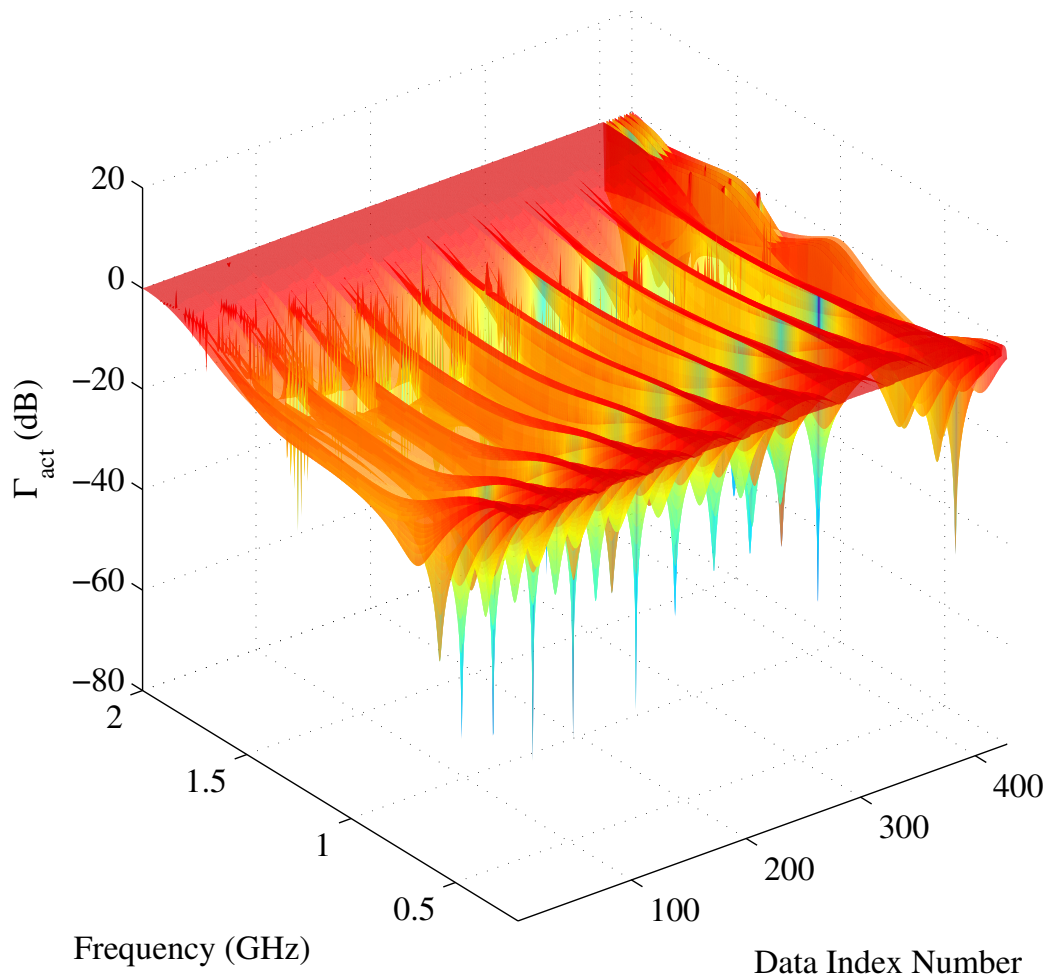


Figure 3.13: Raw results of the full parameter study

was argued that a coherent picture will help to establish whether gradual changes in the parameter set results in certain performance characteristics.

To do this, a coherent picture of combined data emerges by finding the dataset containing the smallest value of  $\Gamma_{act}$  as a starting set and then calculating the cross-correlation between the starting set and all the remaining sets. The inherent nature of the  $\Gamma_{act}$  data meant that a strong cross-correlation between datasets will represent a close match of the data. The dataset with the highest value of cross-correlation with the starting set was placed to the right of the starting set. The second-best match was placed to the left.

After the first three sets were placed, the rest of the datasets were added to either side of the 3 starting sets by finding the dataset among the unplaced sets that has the highest value of cross-correlation with the sets at the edges.

In Figure 3.15 the sorted data and the corresponding parameter values can be seen. The legend was not added to the top figure in order to maintain

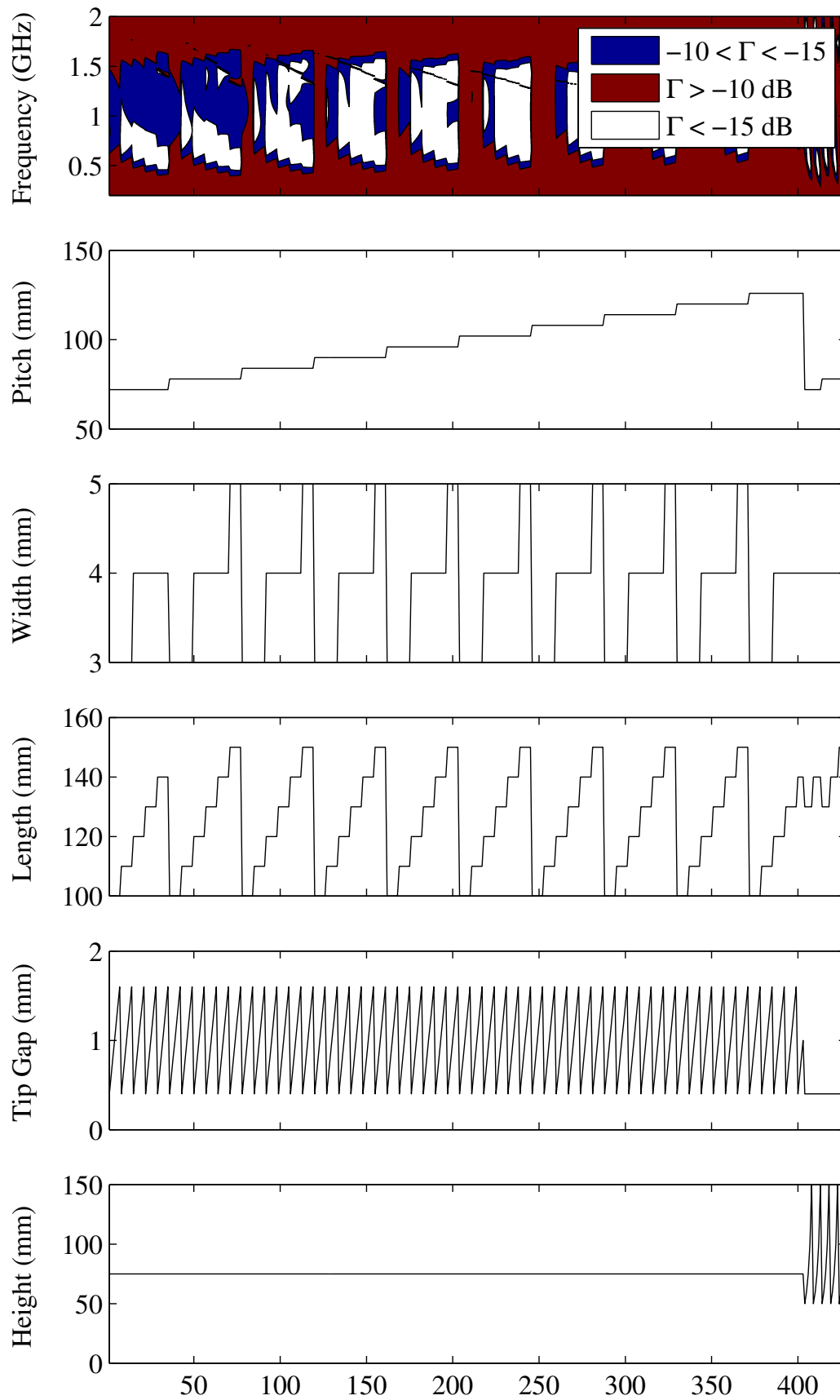


Figure 3.14: Raw results of the full parameter study

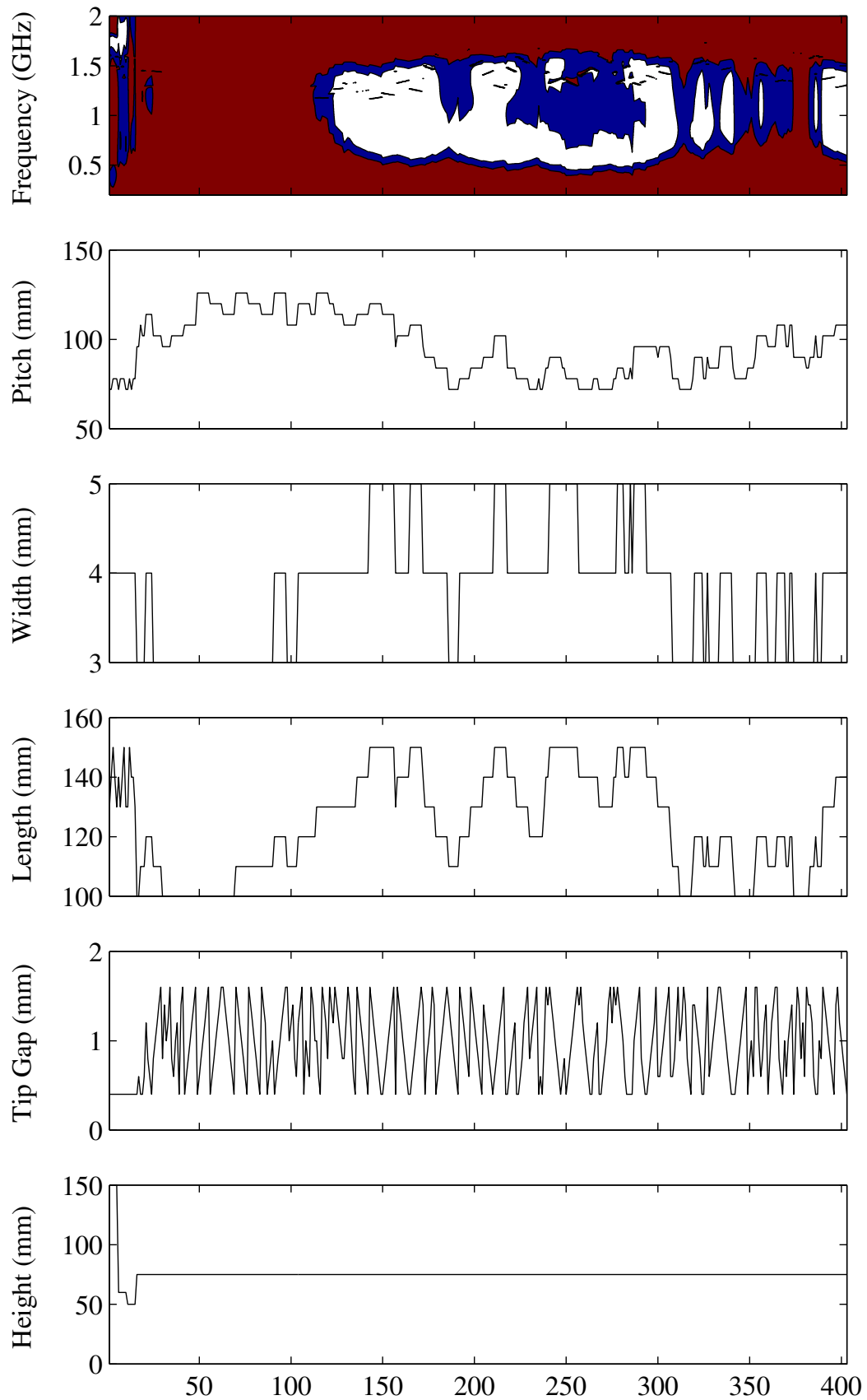


Figure 3.15: Active reflection coefficient data from the parameter sweep, sorted i.t.o. data correlation



a good view of the data, however, the same colour levels were used as in Figure 3.14.

From this figure it is evident that the higher values of pitch seem to result in smaller bandwidth and vice-versa. This confirms the results of the initial parameter study. The element length and the bandwidth also seem to be loosely correlated; however, it should be noted that the pitch is restricted by the element length (the pitch has to be  $> \frac{\text{length}}{2}$  to avoid physical interference between elements). This means that there is loose correlation between the element length and the pitch, which could be what is seen in Figure 3.15.

The results of the correlation sort experiment were therefore inconclusive and it was decided to sort the data in various other ways in an attempt to establish whether any parameters have a direct effect on any aspect of the array performance.

The following performance aspects were identified and the data was sorted according to these criteria:

- Bandwidth with an ‘in-band’ definition of  $\Gamma \leq -10$  dB,
- Bandwidth with an ‘in-band’ definition of  $\Gamma \leq -15$  dB,
- Maximum ‘in-band’ frequency (‘in-band’ defined as  $\Gamma \leq -10$  dB),
- Maximum ‘in-band’ frequency (‘in-band’ defined as  $\Gamma \leq -15$  dB),
- Minimum ‘in-band’ frequency (‘in-band’ defined as  $\Gamma \leq -10$  dB), and
- Minimum ‘in-band’ frequency (‘in-band’ defined as  $\Gamma \leq -15$  dB).

### 3.3.2.1 Bandwidth with an ‘in-band’ definition of $\Gamma \leq -10$ dB

In Figure 3.16 the data is sorted according to bandwidth with an ‘in-band’ definition of  $\Gamma \leq -10$  dB ( $BW_{10\text{dB}}$ ). From this figure it can be seen that the initial conclusion regarding the relationship between pitch and bandwidth is incomplete. A rough correlation is still indicated, but the data would suggest a more complicated relationship between pitch and bandwidth.

Figure 3.17 attempts to provide insight into possibilities of more complex relationships between the bandwidth and the pitch, the width, and the length by plotting the pitch-to-width and pitch-to-length ratios against the sorted data. These ratios seem to provide a better correlation, however, it should be noted that the pitch and length data are already correlated as explained above.

It should also be noted that for wider bandwidths, a smaller percentage of  $\Gamma_{\text{act}}$  falls below  $-15$  dB. It would seem that a trade-off exists between the bandwidth that can be achieved and the ‘depth’ of  $\Gamma_{\text{act}}$ .

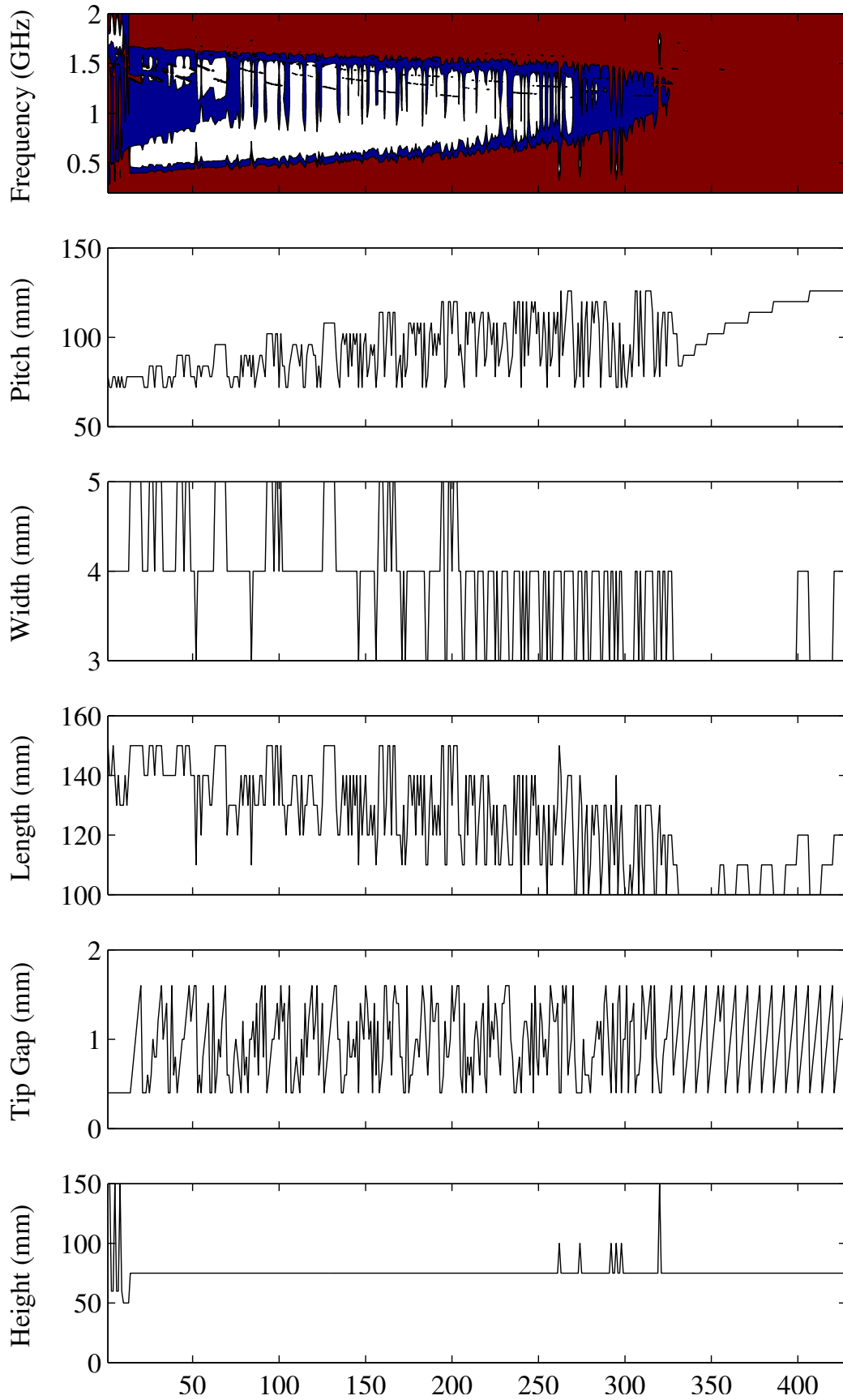


Figure 3.16: Active reflection coefficient data from the parameter sweep, sorted sorted i.t.o. Bandwidth (in-band < -10 dB)

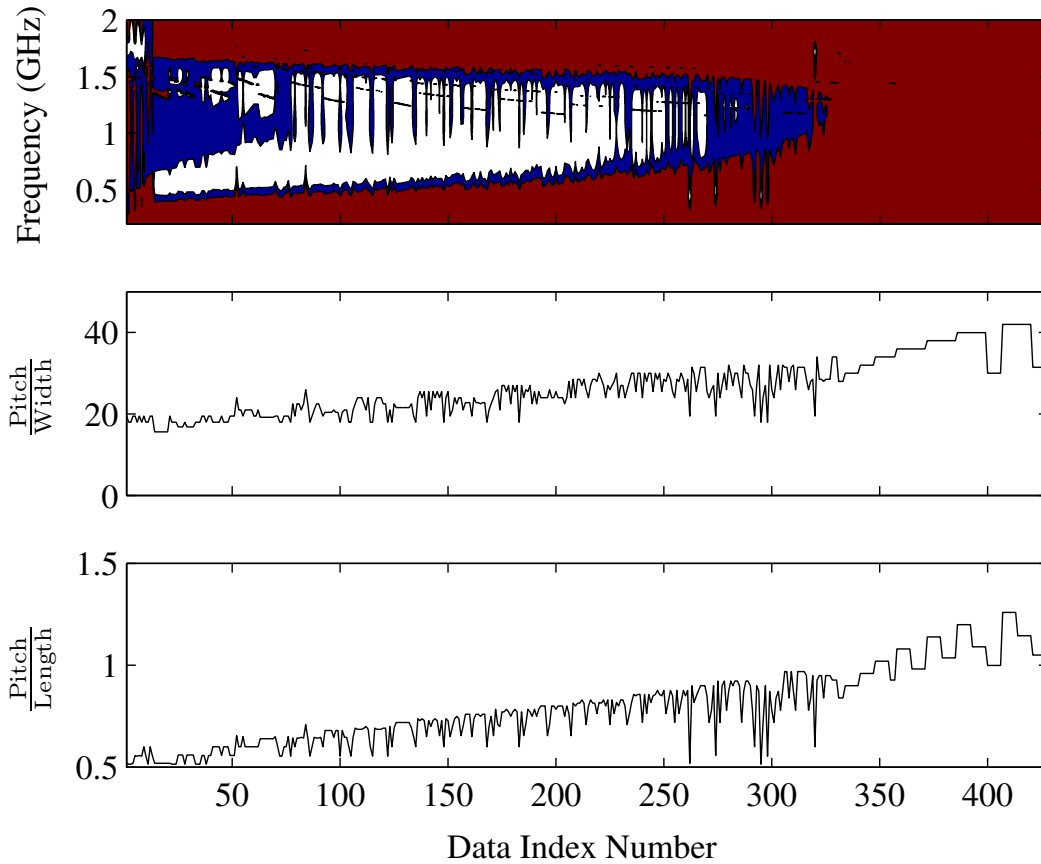


Figure 3.17: Active reflection coefficient data vs relationships between the length, the width and the pitch, sorted i.t.o. Bandwidth (in-band  $\le -10$  dB)

### 3.3.2.2 Bandwidth with an ‘in-band’ definition of $\Gamma \leq -15$ dB

Next, the experiment was repeated, but the ‘in-band’ definition was changed to  $\Gamma \leq -15$  dB ( $BW_{15\text{dB}}$ ). The results can be seen in Figure 3.18. As was the case with the previous experiment, the pitch and the length seem to be loosely correlated with the bandwidth.

Figure 3.19 plots the pitch-to-width and pitch-to-length ratios against the sorted data. It can be seen that a relationship between the ratios of these parameters and the bandwidth is indicated. The inherent relationship between the pitch and the length, however, casts doubt on any conclusion to be drawn from this experiment.

### 3.3.2.3 Maximum ‘in-band’ frequency (‘in-band’ defined as $\Gamma \leq -10$ dB)

Figure 3.20 shows the results for the experiment where the data was sorted according to maximum in-band frequency ( $F_{\text{max}10\text{dB}}$ ), where ‘in-band’ was defined as  $\Gamma \leq -10$  dB.

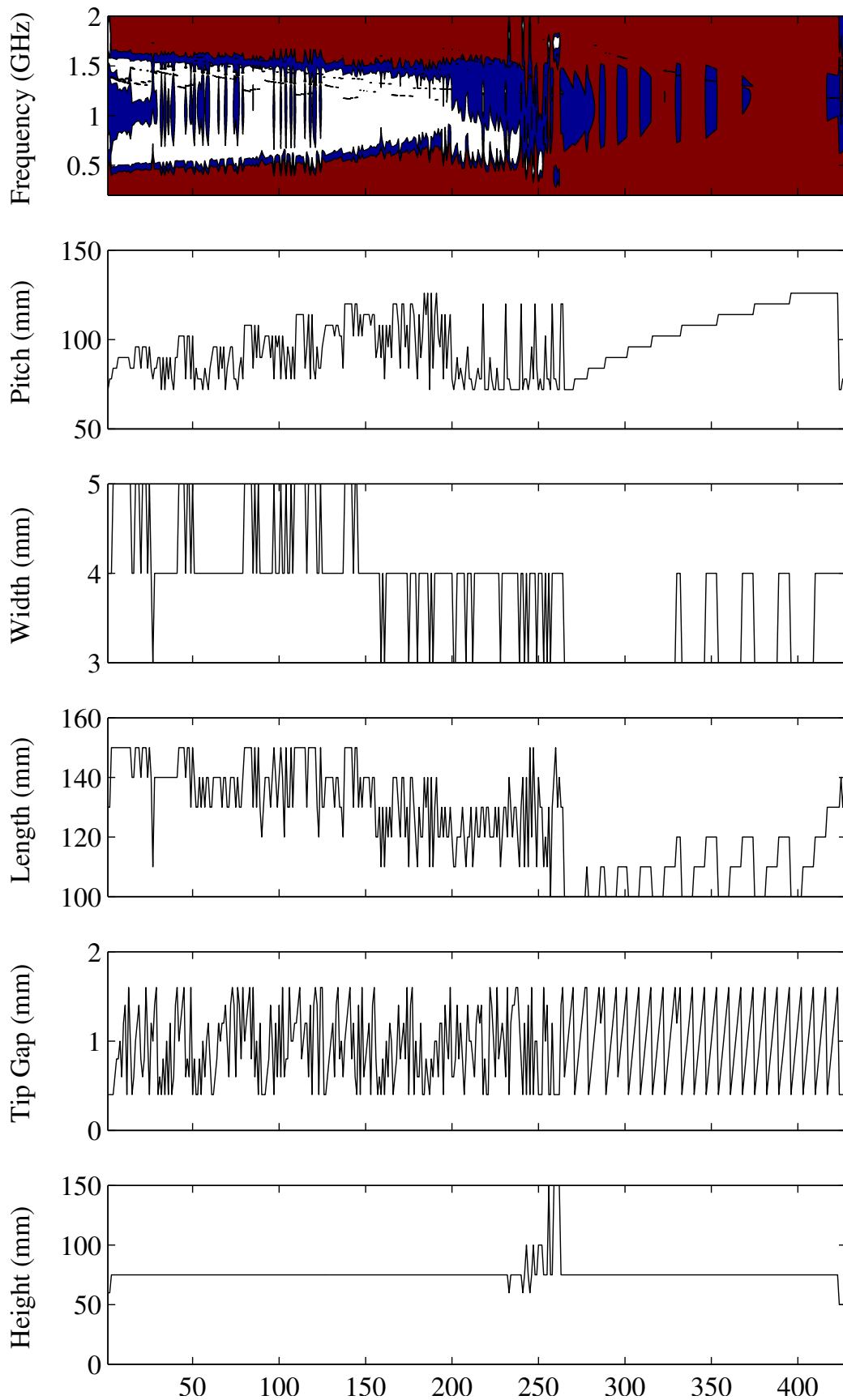


Figure 3.18: Active reflection coefficient data from the parameter sweep, sorted i.t.o. Bandwidth (in-band  $< -15$  dB)

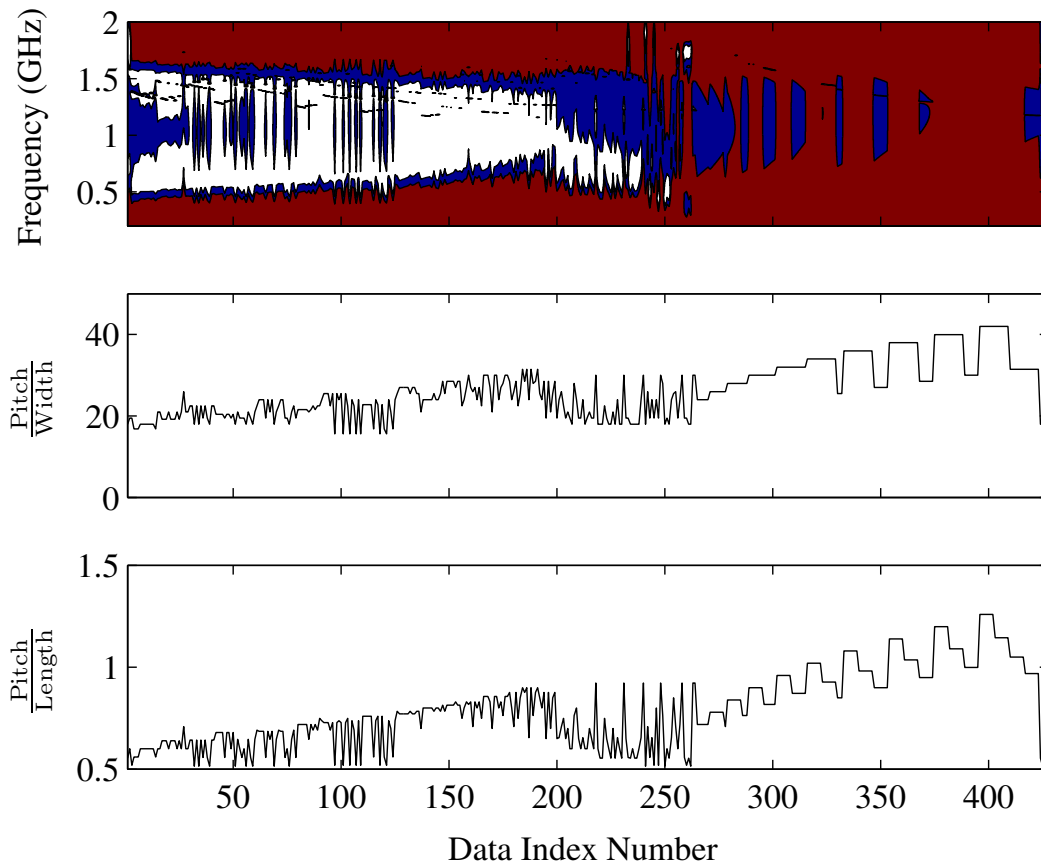


Figure 3.19: Active reflection coefficient data vs relationships between the length, the width and the pitch, sorted i.t.o. Bandwidth (in-band  $-15\text{ dB}$ )

Again the pitch seems to have the greatest effect on the results, however, the “noise” in the pitch data suggests that the results depend on a combination of parameters rather than one single parameter.

As with the previous experiments, the ratios between pitch and width, and pitch and length were also plotted. These plots can be seen in Figure 3.21. A result similar to that of the two bandwidth experiments is displayed, even though the order of the data has changed. This could be attributed to the fact that for the range of parameters chosen for this study, a bigger value for  $F_{\text{max}10\text{dB}}$  is also associated with a greater bandwidth. The experiments are therefore not completely unrelated to one-another.

### 3.3.2.4 Maximum ‘in-band’ frequency (‘in-band’ defined as $\Gamma \leq -15\text{ dB}$ )

Figures 3.22 and 3.23 show the results for the experiment where the data was sorted in terms of maximum in-band frequency  $F_{\text{max}15\text{dB}}$ , with the ‘in-band’ definition set to  $\Gamma \leq -15\text{ dB}$ .

The design parameters on their own seem to be less correlated with the

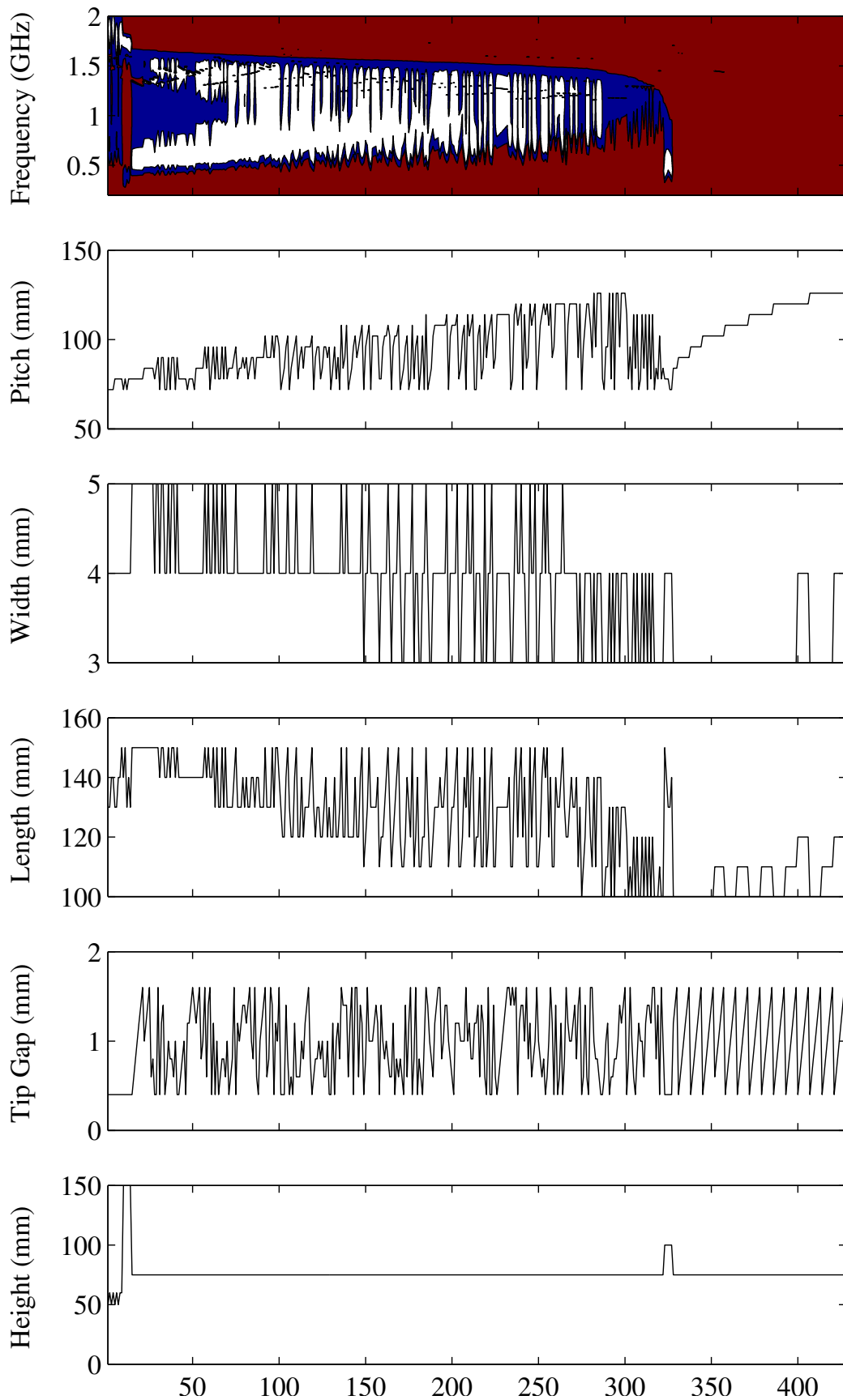


Figure 3.20: Active reflection coefficient data from the parameter sweep, sorted i.t.o.  $F_{\max}$  (in-band  $< -10$  dB)

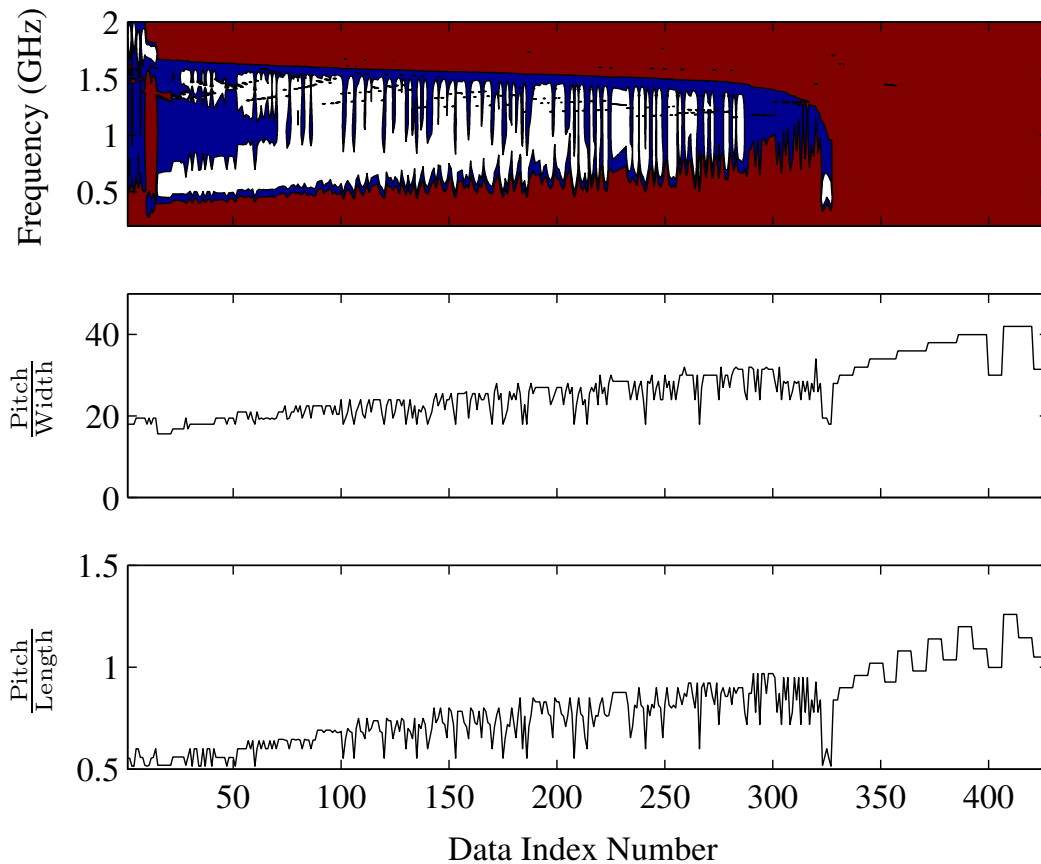


Figure 3.21: Active reflection coefficient data vs relationships between the length, the width and the pitch, sorted i.t.o.  $F_{\max}$  (in-band  $< -10$  dB)

performance characteristic being tested than in the previous experiments, but the pitch-to-width ratio and the pitch-to-length ratios follow the same trend as in the previous experiments, albeit with an even greater deviation. This could be attributed to the much less pronounced relationship between the bandwidth and  $F_{\max 15\text{dB}}$ .

### 3.3.2.5 Minimum ‘in-band’ frequency (‘in-band’ defined as $\Gamma \leq -10$ dB)

The next experiment looked at the minimum in-band frequency where ‘in-band’ is defined as  $\Gamma \leq -10$  dB ( $F_{\min 10\text{dB}}$ ). The results are given in Figures 3.24 and 3.25.

The effect of each single parameter on  $F_{\min 10\text{dB}}$  seem to be close to random, however, the pitch-to-width and pitch-to-length ratios seem to be much more correlated with it. The clear relationship between  $F_{\min 10\text{dB}}$  and  $BW_{10\text{dB}}$  illustrated in the figures should also be noted in this case.

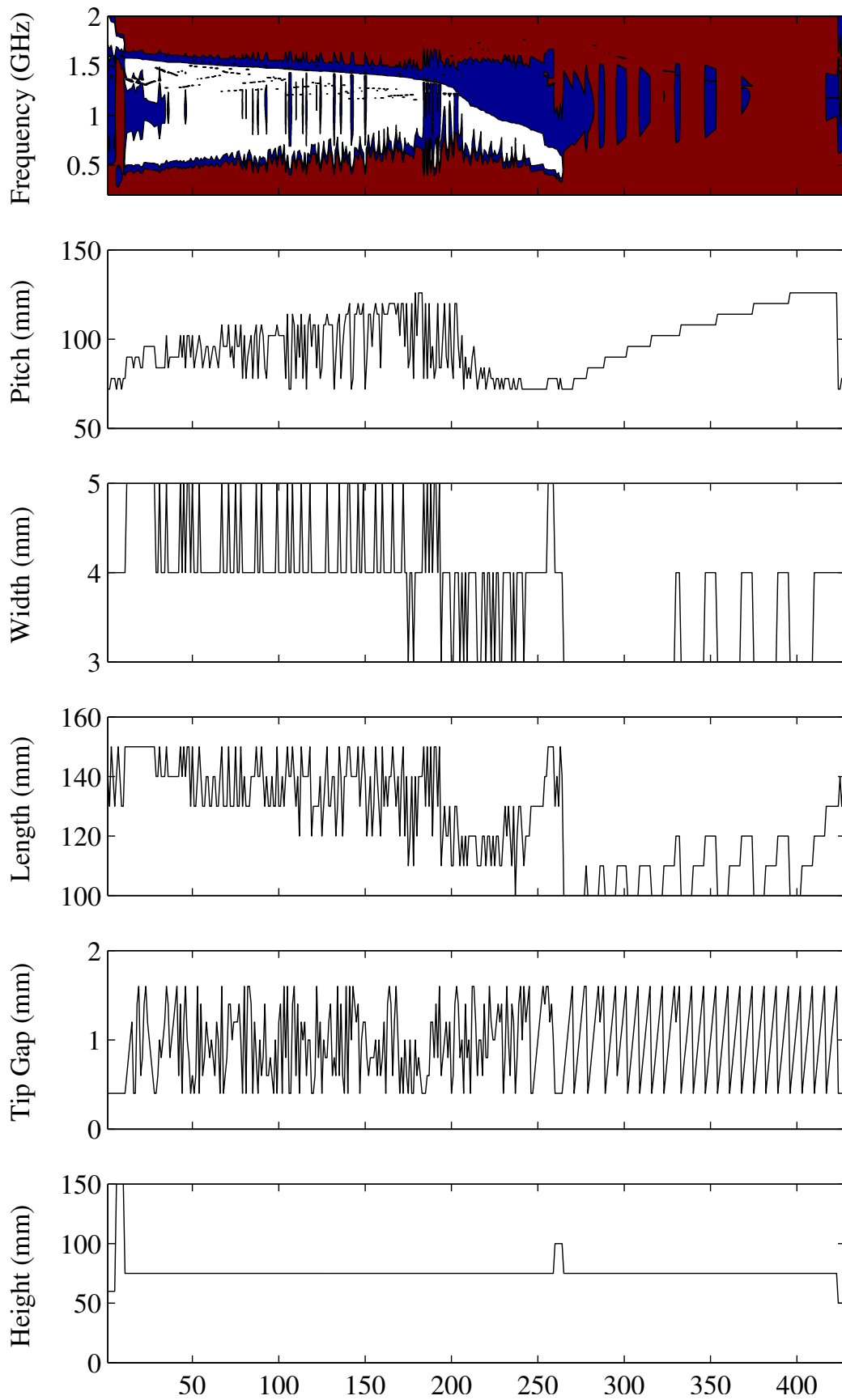


Figure 3.22: Active reflection coefficient data from the parameter sweep, sorted i.t.o.  $F_{\max}$  (in-band  $< -15$  dB)



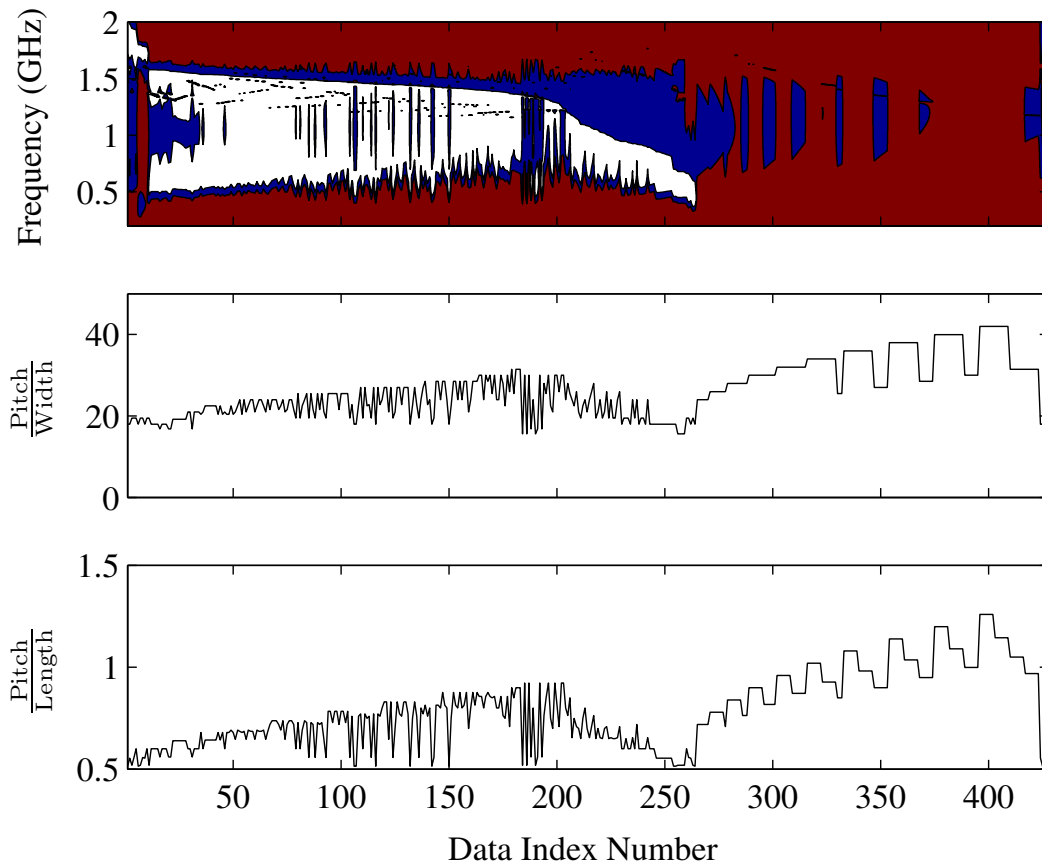


Figure 3.23: Active reflection coefficient data vs relationships between the length, the width and the pitch, sorted i.t.o.  $F_{\max}$  (in-band  $< -15$  dB)

### 3.3.2.6 Minimum ‘in-band’ frequency (‘in-band’ defined as $\Gamma \leq -15$ dB)

The last experiment looks at the minimum in-band frequency with an in-band definition of  $\Gamma \leq -15$  dB ( $F_{\min 15\text{dB}}$ ). With a few exceptions, the data follows roughly the same pattern as that of the  $F_{\min 10\text{dB}}$  experiment. It is therefore reasonable to draw the same conclusions - i.e. no single parameter has an overwhelming effect on the minimum frequency, but the pitch-to-width, and the pitch-to-length ratios seem to be correlated with  $F_{\min 15\text{dB}}$ , possibly due to a correlation between  $F_{\min 15\text{dB}}$  and  $BW_{10\text{dB}}$ .

### 3.3.3 Conclusions drawn from the parameter studies

Both the superficial and the detailed parameter studies have shown that no one single parameter has a clear effect on any aspect of the array performance. This observation is supported by the underlying physics of the structure discussed in Section 3.2.

In the equivalent circuit model of the structure shown in Figure 3.10, the capacitance is due to the close proximity of the overlapping elements. The

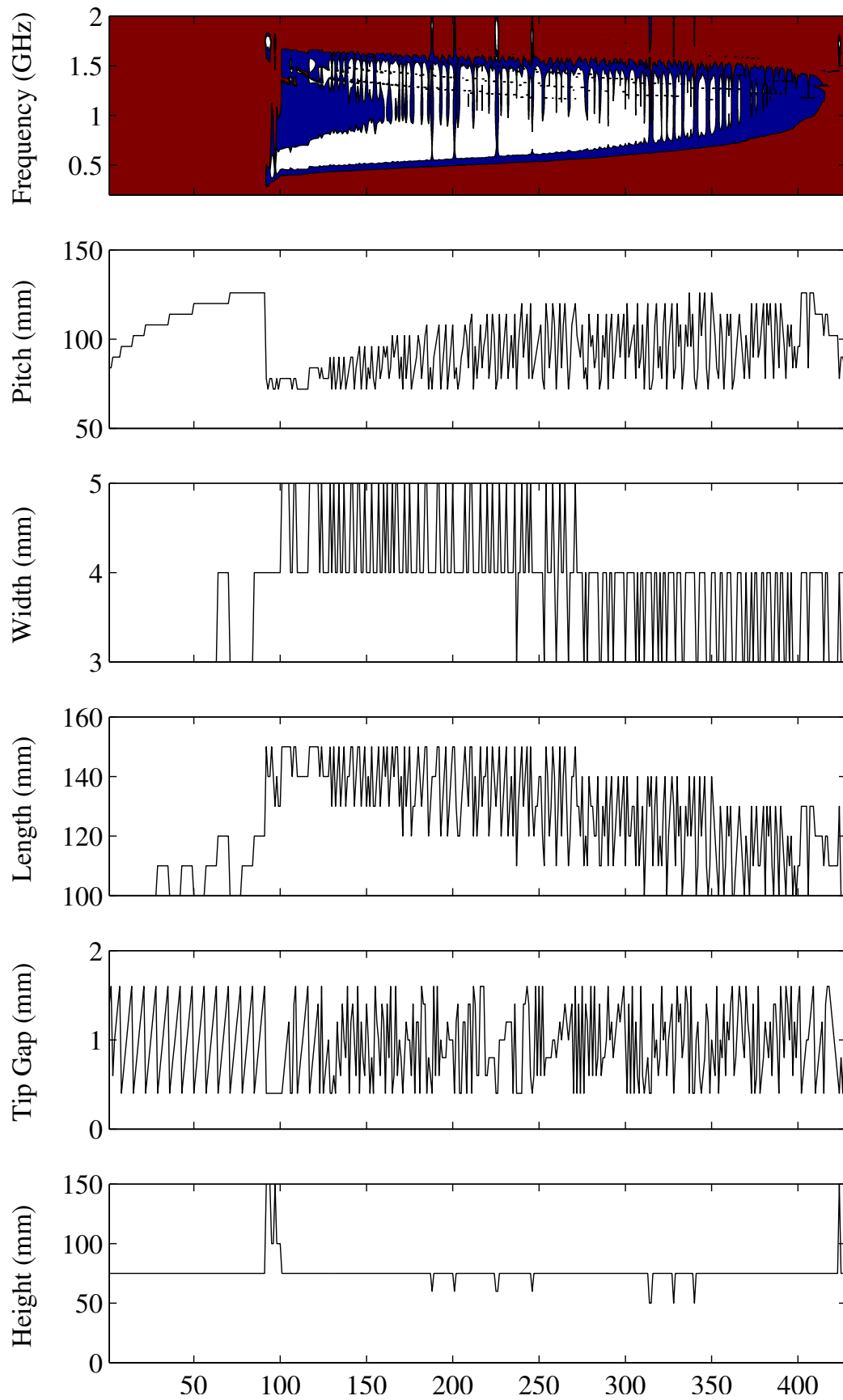


Figure 3.24: Active reflection coefficient data from the parameter sweep, sorted i.t.o.  $F_{min}$  (in-band  $< -10$  dB)

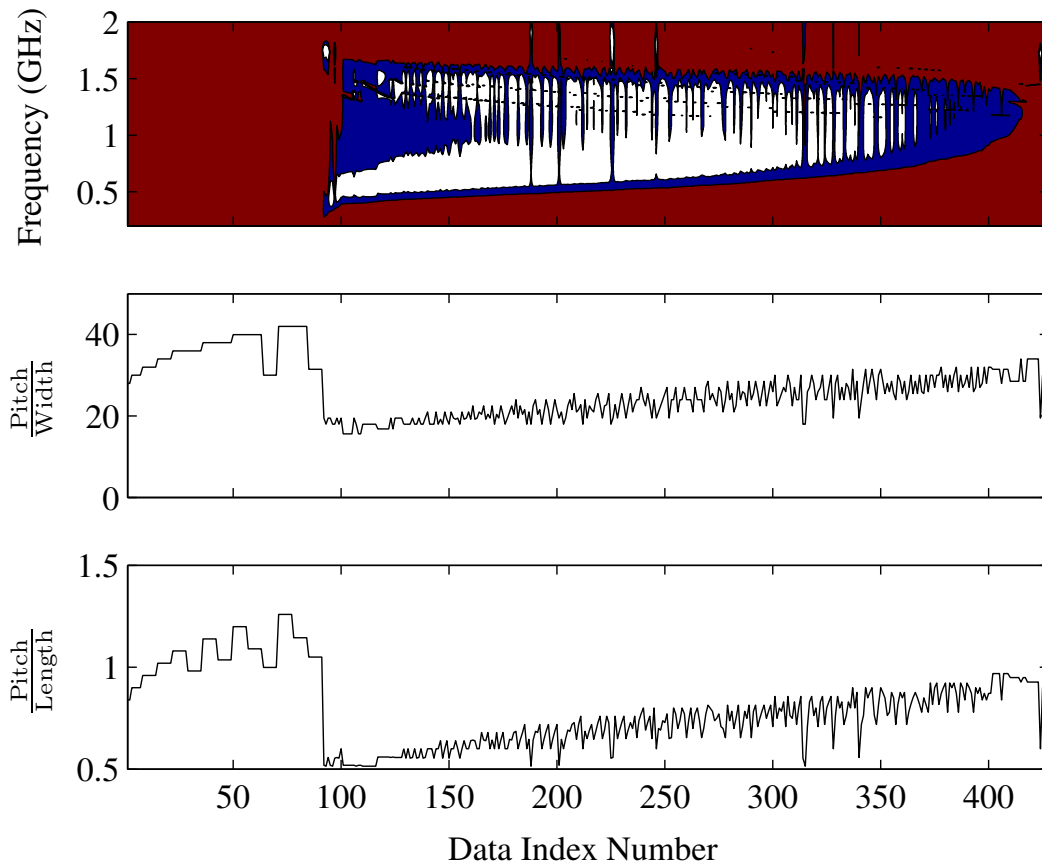


Figure 3.25: Active reflection coefficient data vs relationships between the length, the width and the pitch, sorted i.t.o.  $F_{\min}$  (in-band  $< -10$  dB)

pitch, the width, and the tip-gap will therefore determine the value of the capacitance.

The inductance is due the elements themselves and the ground plane, so the height above the ground plane, the element width and the element length are the parameters that contribute to the value of the inductance.

When taking the restriction the element length imposes on the pitch into account, it is clear that the all the parameters simultaneously establish the balance between the capacitance and the inductance that results in the desired performance. It is therefore safe to conclude that a more sophisticated optimisation procedure is indicated in order to achieve that balance.

The experiments also showed that there exists a trade-off between the bandwidth that can be achieved and the depth of the reflection coefficient which is also in line with the Bode-Fano limits for matching networks [60].

The next section discusses the optimisation procedure that was followed to design a Single-Polarized DDA for the requirements given in Section 2.4.

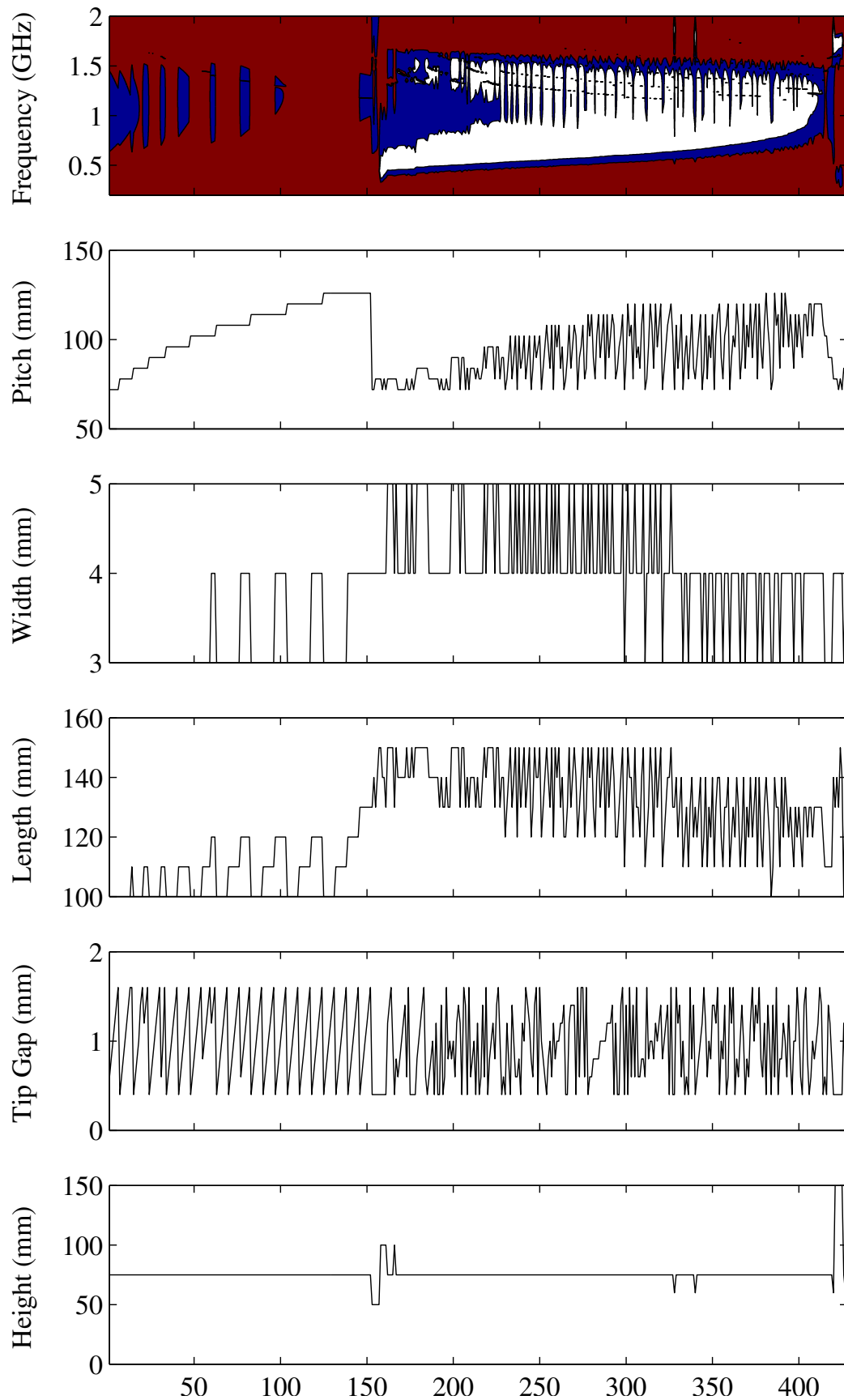


Figure 3.26: Active reflection coefficient data from the parameter sweep, sorted i.t.o.  $F_{min}$  (in-band  $< -15$  dB)

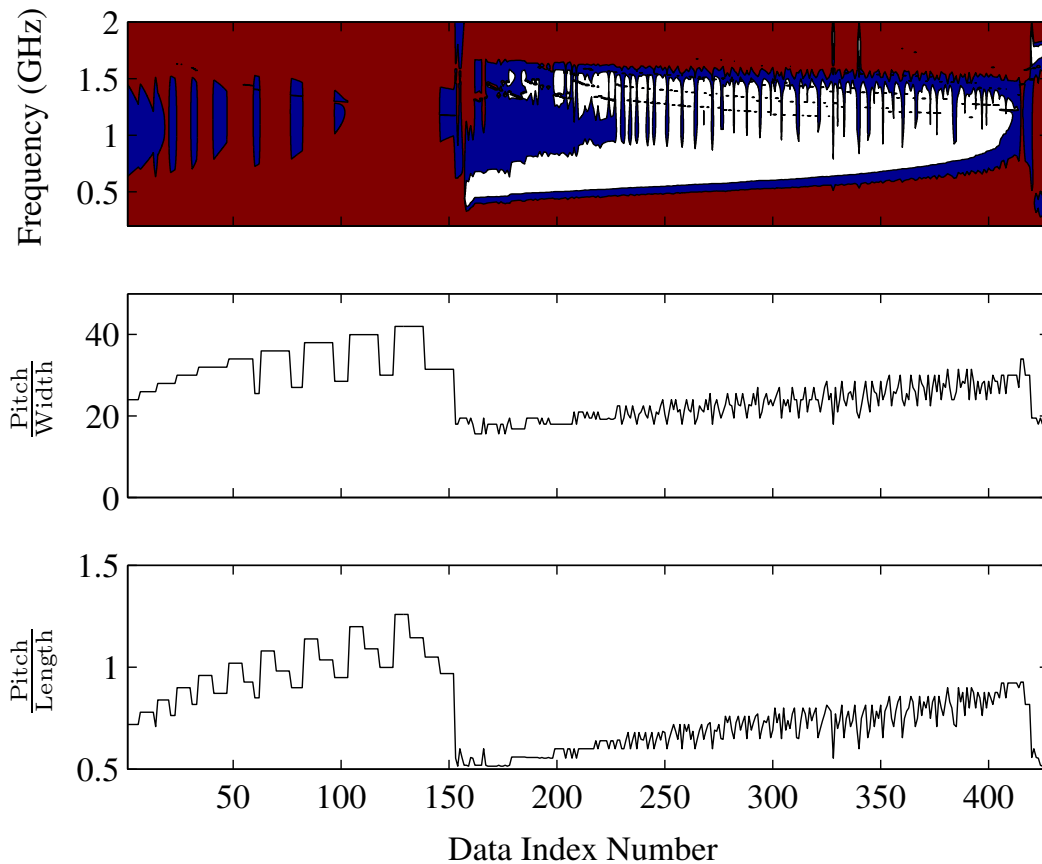


Figure 3.27: Active reflection coefficient data vs relationships between the length, the width and the pitch, sorted i.t.o.  $F_{\min}$  (in-band  $< -15$  dB)

## 3.4 Optimisation

One of the conclusions of the parameter study was that there is evidence of a trade-off between the bandwidth and the depth of  $\Gamma$  in the passband (Bode-Fano limit). It was therefore decided to do two separate optimisations with different goals. This approach would serve as an extension to the parameter study while ensuring that a true optimum parameter set for the desired performance requirements is identified.

### 3.4.1 Optimisation Goals

The two optimisation goals were chosen to firstly test how small  $\Gamma$  can be in the passband if a narrower bandwidth is chosen, and secondly: what the maximum bandwidth is that can be achieved. The goals were therefore chosen as follows:

1. Optimising for a “deep” active reflection coefficient:  
Pass-band defined as  $\Gamma_{\text{act}} \leq -15$  dB for 450 – 1450 MHz

## 2. Optimising for a wider bandwidth:

Pass-band defined as  $\Gamma_{\text{act}} \leq -10$  dB for 400 – 1600 MHz

### 3.4.2 Optimiser Details

Since the focus of this project was antenna design rather than optimisation, it was decided to use one of the built-in optimisers offered by FEKO Version 7.0 [54]. There are three algorithms offered; the Particle Swarm Optimisation (PSO), Genetic Algorithm (GA) and Nelder-Mead Method [61,62]. FEKO can also automatically select a suitable optimisation algorithm from those three depending on the specific problem at hand.

After some experimentation with all the methods offered, it was decided to use the Genetic Algorithm as it offered the fastest convergence for this specific problem.

The parameters, their maximum, minimum and starting values are given in Table 3.2. In order to speed up convergence of the optimiser, the starting values were chosen optimally from the parameter study.

The results of the optimisation are discussed in the next section.

Table 3.2: Details of the optimisation parameters.

Parameter	Minimum Value	Maximum Value	Start Value
Pitch	$0.23\lambda_0$	$0.45\lambda_0$	$0.28\lambda_0$
Width	1 mm	10 mm	4 mm
Length	100 mm	200 mm	140 mm
Tip Gap	0.4 mm	2 mm	0.4 mm
Height	37.5 mm	100 mm	75 mm

### 3.4.3 Optimisation Results

The parameters resulting in an optimum solution for the first optimisation (pass-band defined as  $\Gamma_{\text{act}} \leq -15$  dB for 450 – 1450 MHz) are given in Table 3.3.

Since it is not possible to manufacture an antenna with such fine tolerances, further investigation was done as to how more practical parameter values will affect the performance of the array. This investigation will also reveal any performance degradation that might arise due to manufacturing tolerances. The set of practical values are given in Table 4.1.

The results of a simulation done using the optimum values and the five sets of practical values are given in Figure 3.28. The optimisation mask is also displayed on the figure.

Table 3.3: Optimisation 1 output parameters

Parameter	Value (m)
Pitch	$\lambda_0 \times 2.803205183e-01$
Width	3.990064108e-03
Length	1.377913280e-01
Tip Gap	5.835452225e-04
Height	7.396040911e-02

Table 3.4: Practical values for Optimisation 1

Parameter	Prac 1	Prac 2	Prac 3	Prac 4	Prac 5
Pitch	$0.28\lambda_0$	80 mm	84 mm	84 mm	84 mm
Width	4 mm	4 mm	4 mm	4 mm	4 mm
Length	140 mm	140 mm	140 mm	138 mm	137 mm
Tip Gap	0.6 mm	0.6 mm	0.6 mm	0.6 mm	0.6 mm
Height	75 mm	75 mm	75 mm	75 mm	75 mm

Table 3.5: Optimisation 2 output parameters

Parameter	Value (m)
Pitch	$\lambda_0 \times 2.707934151e-01$
Width	3.943999260e-03
Length	1.437544697e-01
Tip Gap	5.296605827e-04
Height	7.531909957e-02

It can be seen that the optimisation goal was not quite met. This suggests that this structure will not be able to produce such a “deep” reflection coefficient over a large bandwidth, which confirms the observation made in this regard during the parameter study. The results of the five sets of practical values show only small deviations from the optimal parameter set. This suggests that a certain level of immunity against manufacturing tolerances is offered.

Table 3.5 lists the parameters resulting in an optimum solution for the second optimisation (pass-band defined as  $\Gamma_{\text{act}} \leq -10$  dB for 400 – 1600 MHz). The same experimentation with practical values were done as was done with the first optimisation. These practical values are given in Table 3.6, and the results of these simulations are given in Figure 3.29.

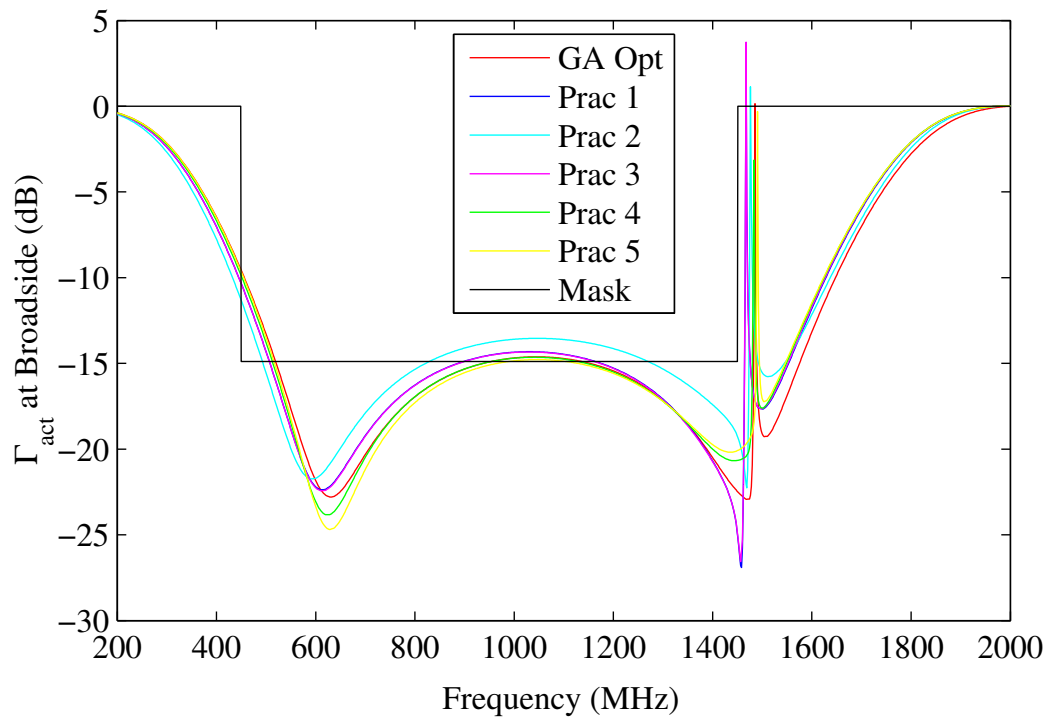


Figure 3.28: Comparison of the active reflection coefficients of the optimal parameter set from Optimization 1 compared to practical parameter values.

Table 3.6: Practical values for Optimisation 2

Parameter	Prac 1	Prac 2	Prac 3
Pitch	78 mm	81 mm	79 mm
Width	4 mm	3.9 mm	3.9 mm
Length	144 mm	144 mm	144 mm
Tip Gap	0.5 mm	0.53 mm	0.53 mm
Height	76 mm	75.3 mm	75.3 mm



The optimiser was much closer to achieving the bandwidth goal set with more lenient in-band reflection coefficient criteria. Furthermore, the same immunity to manufacturing tolerances is observed as with the first optimisation.

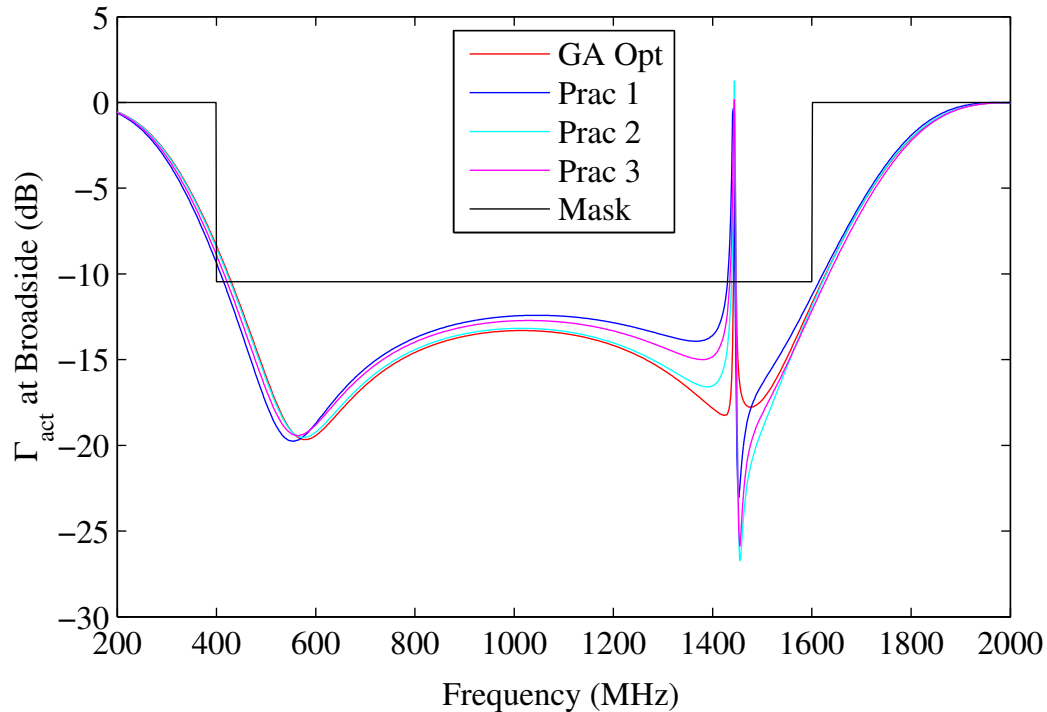


Figure 3.29: Comparison of the active reflection coefficients of the optimal parameter set from Optimisation 2 compared to practical parameter values.

In Figure 3.30, the results of both optimisations are plotted on the same axis. It can be seen that even with slightly different optimisation goals, the results that were achieved are similar. This suggests that these results are as close to a “true optimum” than is likely to be achievable for these specifications. The level of immunity against manufacturing tolerances observed during the whole optimisation process is also displayed again.

### 3.5 Results

Since the difference between the results of the optimisation and the “practical” parameters is small, it was decided to base the reference design on the parameters used for Practical solution 2 of Optimisation 1, given in Table 4.1.

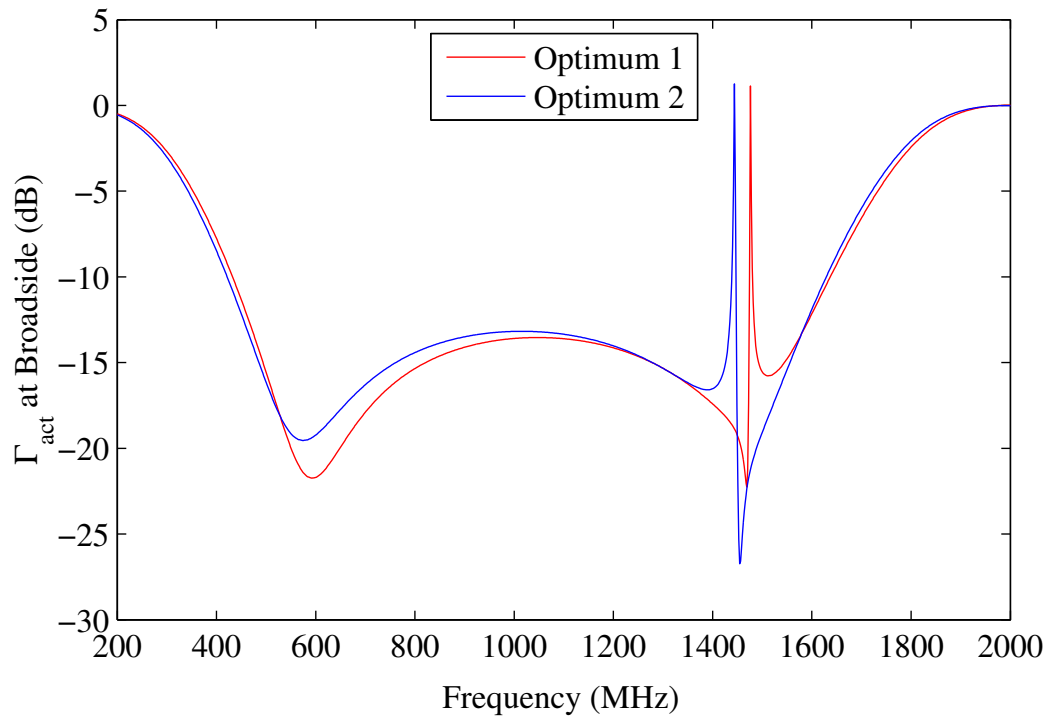


Figure 3.30: Comparison of the active reflection coefficient at broadside of Optimisation 1 and Optimisation 2.

### 3.5.1 Impedance Bandwidth

The results of the parameter study indicated a trade-off between the depth of the reflection coefficient and the bandwidth that can be achieved. It was therefore decided to use an in-band definition of  $-10$  dB for the remainder of the design process. This definition is also in line with the other MFAA candidate topologies [1, 52].

#### 3.5.1.1 Broadside

Figure 3.31 shows the active reflection coefficient of the infinite array at broadside. The frequency range is seen to be from 432 MHz to 1.637 GHz, which translates to a bandwidth of approximately  $3.8 : 1$ . This bandwidth compares well with the  $\approx 3.8 : 1$  bandwidth achieved in simulation results of the ORA in [1].

#### 3.5.1.2 Scan Performance

The next set of experiments were done to investigate the effect of scanning on the active reflection coefficient of the array. Two experiments were done; the first experiment scanned along the  $E$ -plane, and the second scanned along the  $H$ -plane.

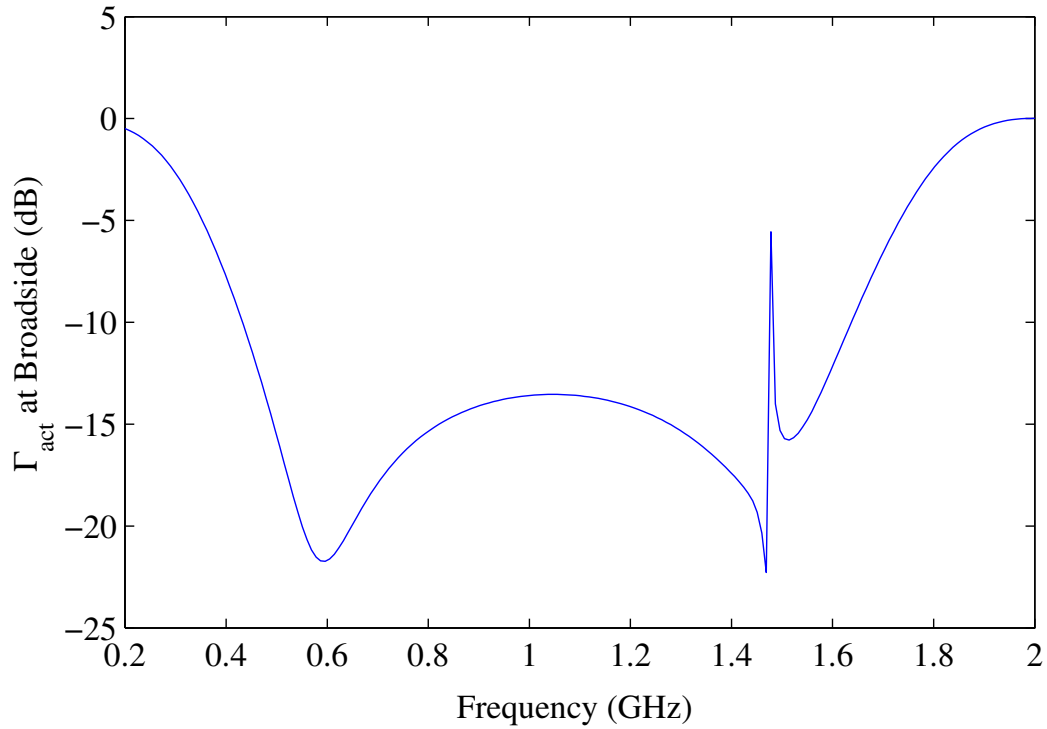


Figure 3.31: Active reflection coefficient at broadside for an infinite single polarized DDA

The active antenna impedance  $Z_{\text{act}}(\theta, \phi)$  for each scan angle was calculated by using a plane wave excitation from the angle in question. This was achieved by determining the open-circuit voltage  $V_{\text{oc}}$  and short-circuit current  $I_{\text{sc}}$  for each angle of incidence and then calculating  $Z_{\text{act}}(\theta, \phi)$  as follows:

$$Z_{\text{act}}(\theta, \phi) = \frac{V_{\text{oc}}(\theta, \phi)}{I_{\text{sc}}(\theta, \phi)}. \quad (3.5.1)$$

These impedance values were then used to determine the active reflection coefficient  $\Gamma_{\text{act}}(\theta, \phi)$  for corresponding scan angle.

### E-plane Scan:

A visualisation of the  $E$ -plane scan range is illustrated in Figure 3.33. This figure shows a unit cell of a single polarized DDA with blue arrows indicating the direction of propagation for a specific data set, and red arrows indicating the polarization. The  $E$ -plane in this model is located on the  $\phi = 90^\circ$  axis, while the scan range is along the  $\theta$  axis, from  $-85^\circ$  to  $85^\circ$ , with  $\theta = 0$  at broadside.

The results are shown in Figure 3.33. The figure has the same “top-view” format that was used in the parameter-study. The  $y$ -axis shows the frequency and the  $x$ -axis the scan angle. The same colour mapping was used

as with the parameter study results and is also indicated on the Figure. All the in-band data is therefore indicated by the blue and white sections, while the brown sections are out of band.

Since the structure is a symmetric, periodic structure, the results are symmetrical around the  $\theta = 0$  axis. It is also clear that the whole in-band frequency range shifts to a higher frequency as the scan angle increases. This is because the relative size of the array elements seen by the incoming wave-front decreases as the scan angle increases. At the same time, the relative inter-element spacing seen by the incoming wave becomes less optimum for wide-band operation. This will lead to a decrease in bandwidth as the scan angle increases. When the scan angle increases to approximately  $60^\circ$  off bore-sight, the active impedance of the antenna elements become almost entirely reactive, resulting in the bulk of the energy being stored instead of radiated.

As the beam is steered, the relative phase difference between the elements change, which will result in the frequency at which the common-mode resonance occur changing. This phenomenon can also be seen in the figure.

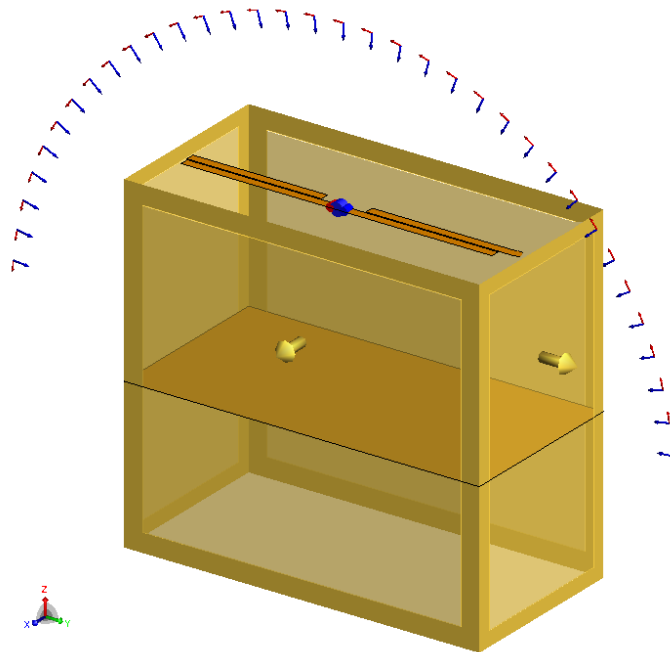


Figure 3.32: Visualisation of the tested scan range along the  $E$ -plane.

### H-plane Scan:

Figure 3.34 illustrates the scan range along the  $H$ -plane. The direction of propagation is again indicated using blue arrows while the red arrows

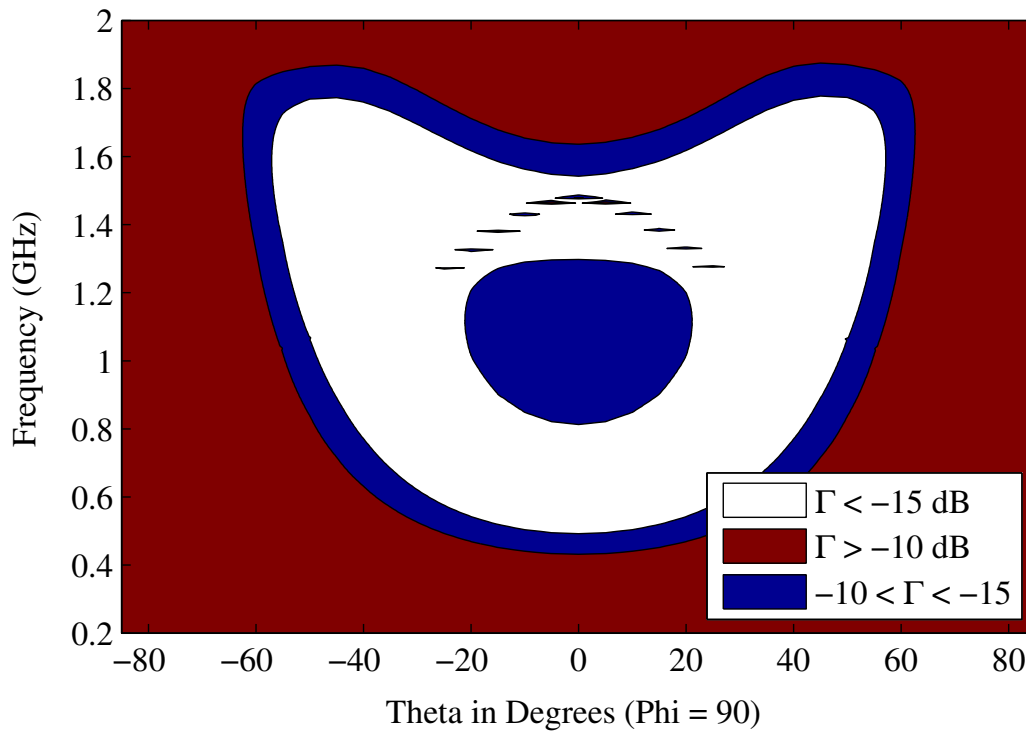


Figure 3.33: Active reflection coefficient for various scan angles along the  $E$ -plane

indicate the polarization, as was the case with the previous experiment. For this model, the  $H$ -plane is located on the  $\phi = 0^\circ$  axis, while the scan range is along the  $\theta$  axis from  $-85^\circ$  to  $85^\circ$  again, with  $\theta = 0$  at broadside.

The results can be seen in Figure 3.35. When scanning along the  $H$ -plane, the relative size of the elements seen by the incoming wave does not change, however, the relative inter-element spacing along the  $x$ -axis does change. This results in a reduction in bandwidth as soon as the relative inter element spacing becomes sub-optimal for wideband operation. As the scan angle approaches the horizon, the size of the aperture seen by the incoming wave will decrease until only a linear array is seen instead of a planar one. This will decrease the bandwidth to that of a single dipole.

Along the  $H$ -plane, the act of scanning does not change the relative phase difference between the connected elements (i.e. the elements along the  $y$ -axis), which means that the frequency at which the common-mode resonance occurs remains unchanged.

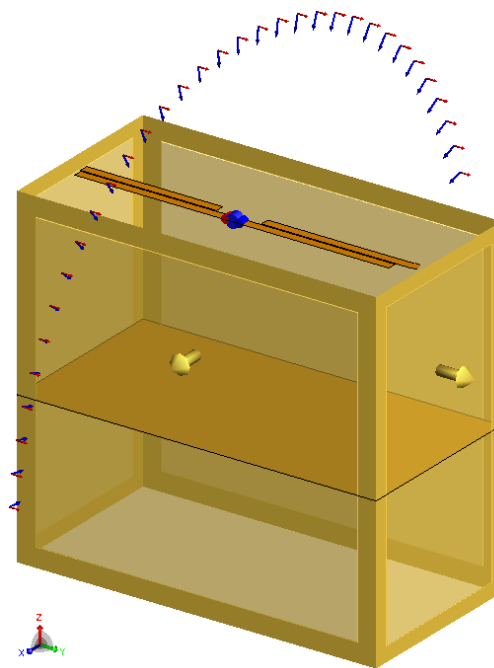


Figure 3.34: Visualisation of the tested scan range along the  $H$ -plane.

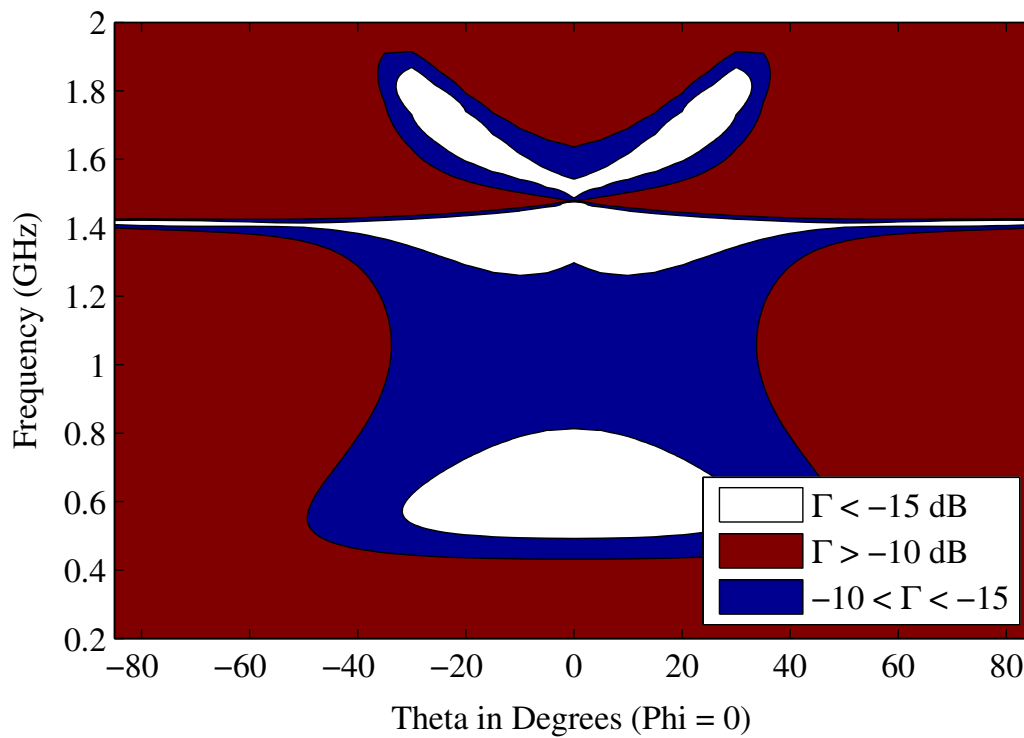


Figure 3.35: Active reflection coefficient for various scan angles along the  $H$ -plane

## 3.5.2 Gain Performance

### 3.5.2.1 Scan Loss

The performance of the array across its entire scan- and frequency range is difficult to judge since the size of the final array is still unknown and the array is at this stage assumed to be infinite. This infinite approximation is reasonable since the final array is likely to consist of thousands of elements.

For a very large array, the radiation pattern is completely dominated by the array factor [13]. The performance of the array in terms of radiation characteristics is therefore restricted by the appearance of grating lobes at large scan angles. The appearance of grating lobes is determined by the inter-element spacing as follows:

$$d_{max} = \frac{\lambda_{min}}{1 + \sin(\theta_{max})} \quad (3.5.2)$$

where  $d_{max}$  is the maximum allowed spacing between elements in order to avoid grating lobes,  $\lambda_{min}$  is the wavelength associated with the maximum in-band frequency, and  $\theta_{max}$  is the specified maximum scan angle.

From equation 3.5.2, it is clear that an array can be designed with the specific aim to avoid grating lobes, should the physical size of the array elements allow it. Since an integral part of the design of the DDA is that the elements are placed in a dense arrangement, the criteria for avoiding grating lobes set out are automatically met along both the  $E$ -plane and  $H$ -plane.

A more reasonable metric for judging the gain performance of the DDA would be the *scan loss*, which Bhattacharyya defines as “the relative gain loss in dB with respect to the broadside scan” in [22]. The scan loss at a specific scan angle  $\theta_0$  can then be calculated as a function of the co-polar gain at broadside,  $G^{co}(0, \phi)$  and the co-polar gain at  $\theta_0$ ,  $G^{co}(\theta_0, \phi)$ :

$$\text{Scan loss at } \theta_0 = 20 \log \left| \frac{G^{co}(0, \phi)}{G^{co}(\theta_0, \phi)} \right|. \quad (3.5.3)$$

Figure 3.36 depicts the scan loss at  $\theta_0 = 45^\circ$  along the  $E$ -plane and the  $H$ -plane for an infinite array. The embedded element pattern calculated using the periodic boundary condition functionality in FEKO was used for this calculation to ensure that gain variations caused by mutual coupling is taken into account.

The scan loss along the  $E$ -plane is higher than that of the  $H$ -plane because the radiation pattern of a halfwave dipole along the  $E$ -plane has a null at  $\theta = 90$ . The gain therefore reduces more rapidly with scan angle along the  $E$ -plane than it does along the  $H$ -plane. It should be noted that the scan loss across the in-band range in the  $E$ -plane is still below 5 dB which is in line with other AA designs [63].

The scan loss along both axes also reach 0 dB at certain frequencies. This has to do with the relative height of the elements above the ground plane.

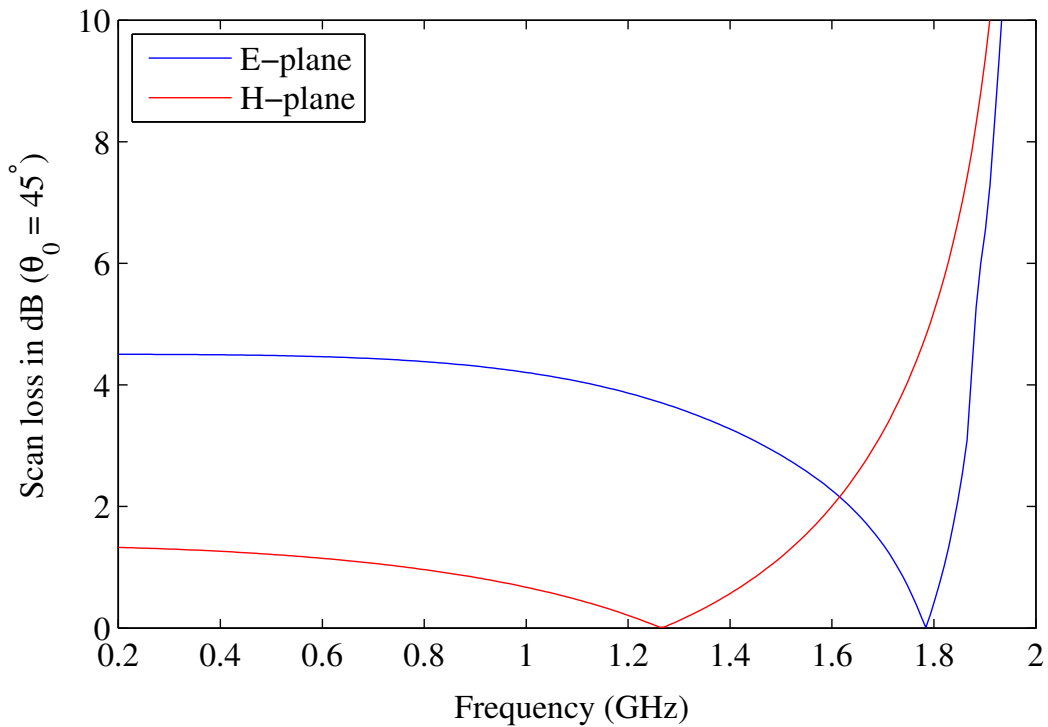


Figure 3.36: Scan loss for  $\theta_0 = 45^\circ$ , on the  $E$ -plane and  $H$ -plane

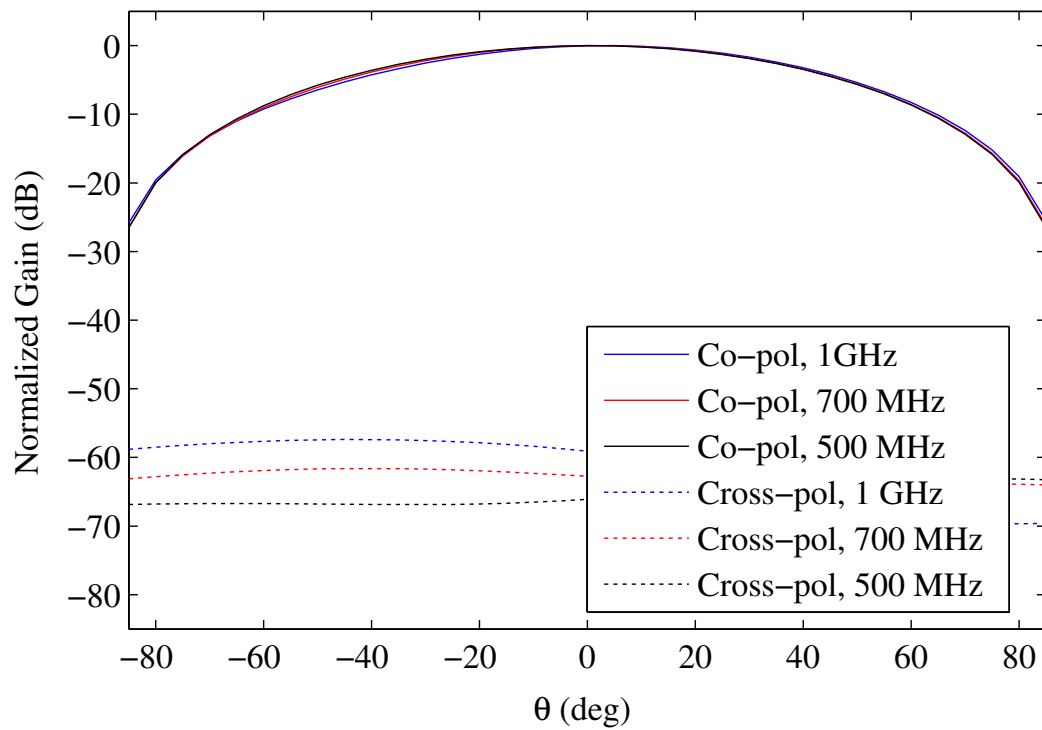
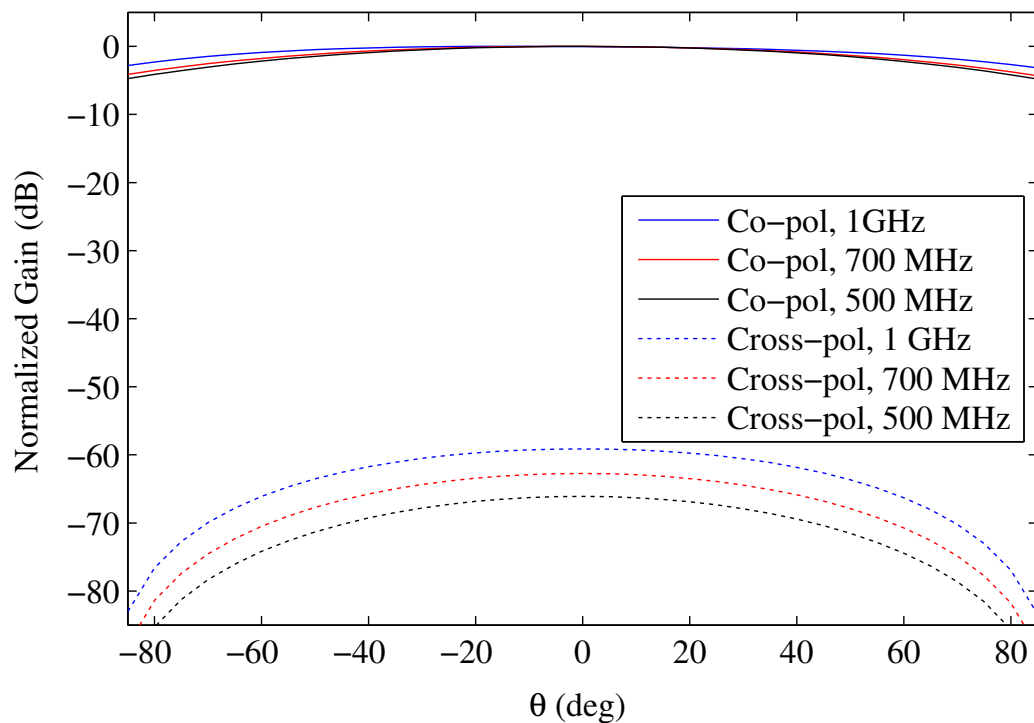
For this design, the antenna elements are  $\lambda/4$  above the ground plane at 1 GHz. This means that for  $f < 1$  GHz, the antenna elements are  $< \lambda/4$  above the ground plane, and for  $f > 1$  GHz, the elements are  $> \lambda/4$  above the ground plane. When dipole elements are  $> \lambda/4$  above the ground plane, the radiation pattern starts to flatten out to develop additional lobes (scalping) [56]. This flattening of the radiation pattern will result in a 0 dB scan loss at a specific frequency that is a function of  $\phi$ .

### 3.5.2.2 Cross-Polarization

Another important metric in terms of the radiation performance of an antenna is the cross polarization performance. Since this is a single polarized array, it was decided to express the cross polarization performance in terms of normalized co-polar and cross-polar gain of the embedded element for scan angles  $-90^\circ \leq \theta \leq 90^\circ$  along the  $E$ -plane,  $H$ -plane and  $D$ -plane, at 3 different frequencies.

The results are shown in Figures 4.15a, 4.15b and 4.14c for the  $E$ -plane,  $H$ -plane and  $D$ -plane respectively. It can be seen that good cross-polarization performance is demonstrated in all three planes for a scan range of  $-45^\circ \leq \theta \leq 45^\circ$ . The cross-polarization performance is also in line with that of other AA designs [1, 64].



Figure 3.37: Co-polar and cross-polar gain patterns along the *E*-plane.Figure 3.38: Co-polar and cross-polar gain patterns along the *H*-plane.

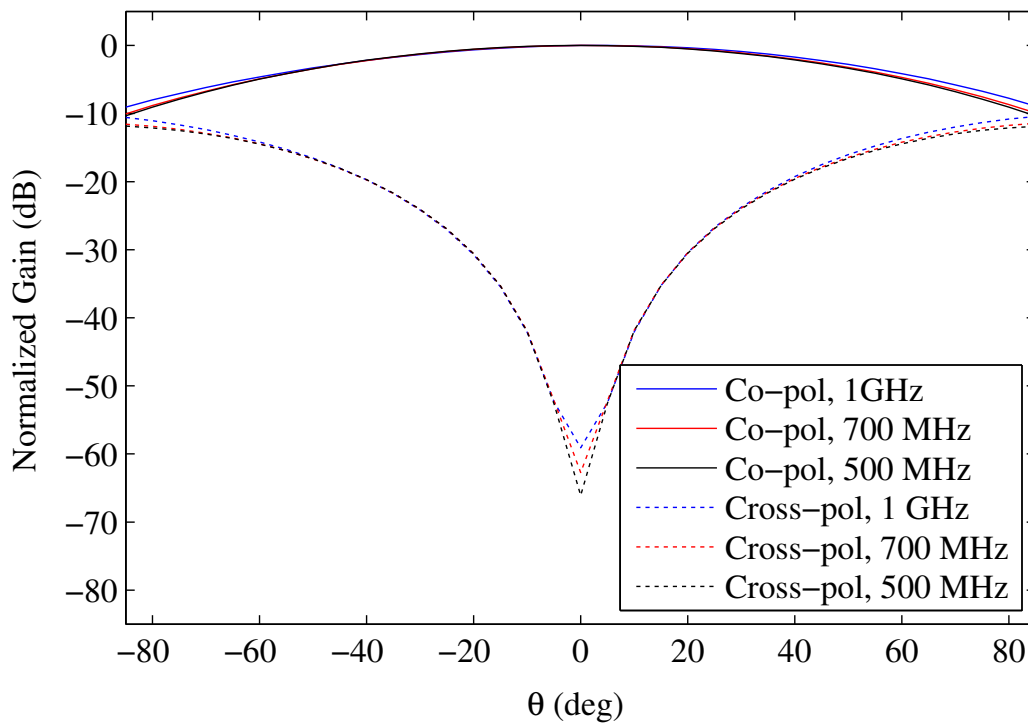


Figure 3.39: Co-polar and cross-polar gain patterns along the  $D$ -plane.

## 3.6 Conclusions

The basic Dense Dipole Array was introduced in this chapter. The theory of how the structure manages to offer considerable bandwidth improvement was discussed followed by an extensive parameter study. An optimal parameter set for single polarized DDA was established using a Genetic Algorithm optimiser. The optimal design was also shown to be relatively immune to manufacturing tolerances.

Finally, results of an optimal design using practically implementable design parameters were analysed and data illustrating the impedance bandwidth as well as the gain performance across a wide scan range was shown. It was demonstrated that the Single Polarized DDA offers performance comparable to other designs intended for MFAA.

## Chapter 4

# The Dual-Polarized DDA

### 4.1 Introduction

As was explained in Section 2.4, a system capable of recovering the polarization information and intensity of incident fields is of paramount importance in Radio Astronomy [21]. In this chapter, the single-polarized DDA introduced in Chapter 3 is therefore expanded to include a second, orthogonal polarization.

The geometry of the dual-polarized structure is introduced in Section 4.2. Section 4.3 provides details on the optimisation procedure and discussed the difficulties encountered with the optimisation. The results are given in Section 4.4 and Section 4.5 concludes.

### 4.2 Geometry

The characteristic impedance of the array elements was calculated in Chapter 3 as  $300 \Omega$ . Due to impedance limitations of commonly used low-loss transmission lines [65], it was seen that it would be difficult to design a feed structure with a characteristic impedance of  $300 \Omega$ . Combining the elements in parallel pairs of 2 will reduce the impedance requirements of the feed to  $150 \Omega$ . A side-effect of this is that the two elements are now effectively “beam-formed” to broadside, potentially compromising the scan performance of the array. However, it also halves the required number of receiver chains resulting in a significant cost saving on system level. It was therefore decided to investigate the level to which the scan performance is compromised to determine whether the potential cost saving is justified.

This parallel feed structure and the fact that the elements overlap necessitated a dual-layer arrangement in order to accommodate two polarizations. In practice, this means that the two polarizations will be etched on either side of a PCB.

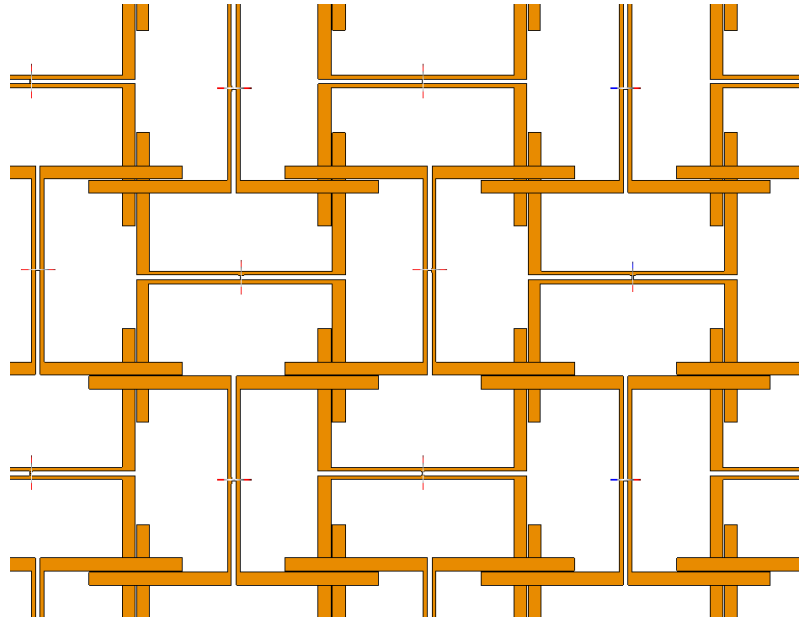


Figure 4.1: A Dense Dipole Array Prototype

A visualisation of the dual-polarized DDA can be seen in Figure 4.1. It will be shown in Section 4.4 that even though elements of opposing polarizations also overlap, their orthogonality ensures sufficient isolation between the two polarizations.

It should be noted that the new layout offers multiple current paths of differing lengths between neighbouring elements. This will result in common-mode resonances begin present at multiple frequencies. Since the design of the common-mode suppressing feed described in Chapter 5 is expected to filter out these resonances, their presence was not judged to negatively affect the performance of the system.

### 4.3 Optimisation

The optimisation procedure and goals that were used for the single polarized DDA were slightly adapted for the dual-polarized case: instead of running two optimisations trading off between bandwidth and the depth of the reflection coefficient, only a single optimisation was run. The linear active reflection coefficient for broadside radiation of an element in an infinite array was optimised. The goals were set to optimise for a frequency band of 450 – 1500 MHz, with a pass-band definition of  $\Gamma_{\text{act}} \leq -10$  dB. The Genetic Algorithm was used again, and the active reflection coefficient of the resulting optimal parameter set was compared to that of three sets of practical values in order to establish whether manufacturing tolerances are likely to have a dramatic effect on the array performance. The parameter values

Table 4.1: Optimal and practical parameters values for the dual-polarized DDA

Parameter	Optimal	Prac 1	Prac 2	Prac 3
Pitch	90.71593247188205 mm	90 mm	90 mm	89 mm
Width	5.781474768171120 mm	5.8 mm	5.9 mm	6 mm
Length	133.4301546381774 mm	130 mm	133 mm	133 mm
Tip Gap	0.664539963682219 mm	0.65 mm	0.65 mm	0.6 mm
Height	77.39205199484446 mm	77.4 mm	75 mm	78 mm

determined by the optimiser as well as the three sets of practical values are given in Table 4.1.

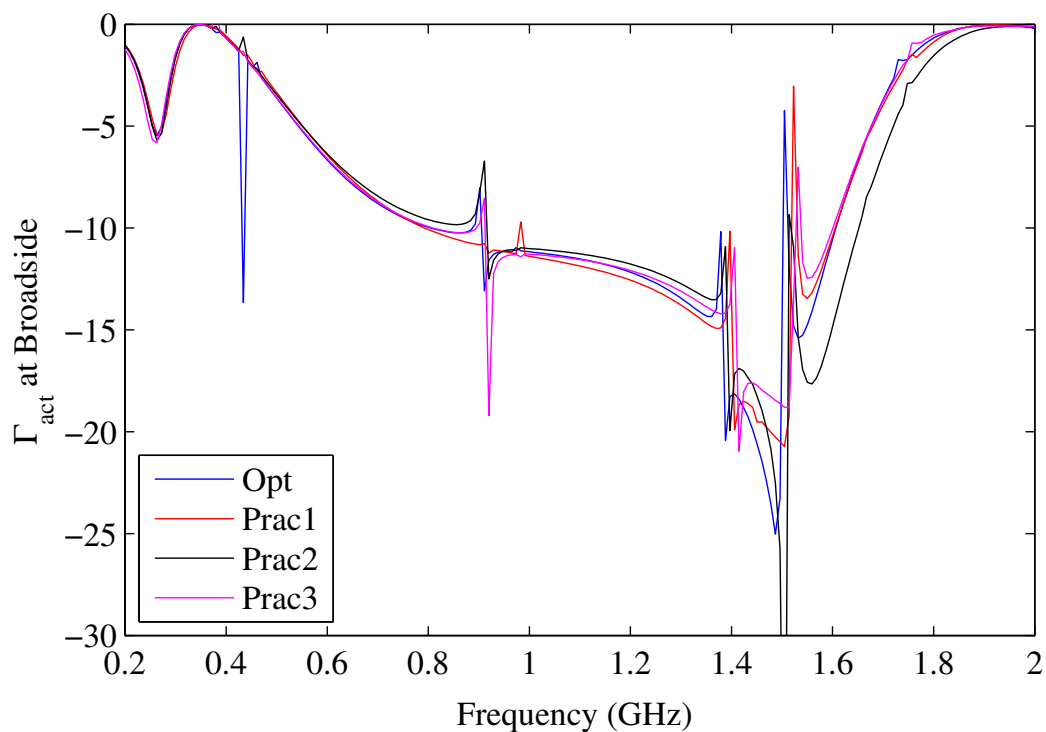


Figure 4.2: Active reflection coefficient for the optimal- and three practical parameter sets.

The active reflection coefficient at broadside of the array with these four sets of parameters is given in Figure 4.2. As was the case with the single-polarized array, there is not a significant difference in the results of the four simulations. The previous conclusion made regarding the relative immunity of the DDA against manufacturing tolerances is therefore also valid for the dual-polarized case.

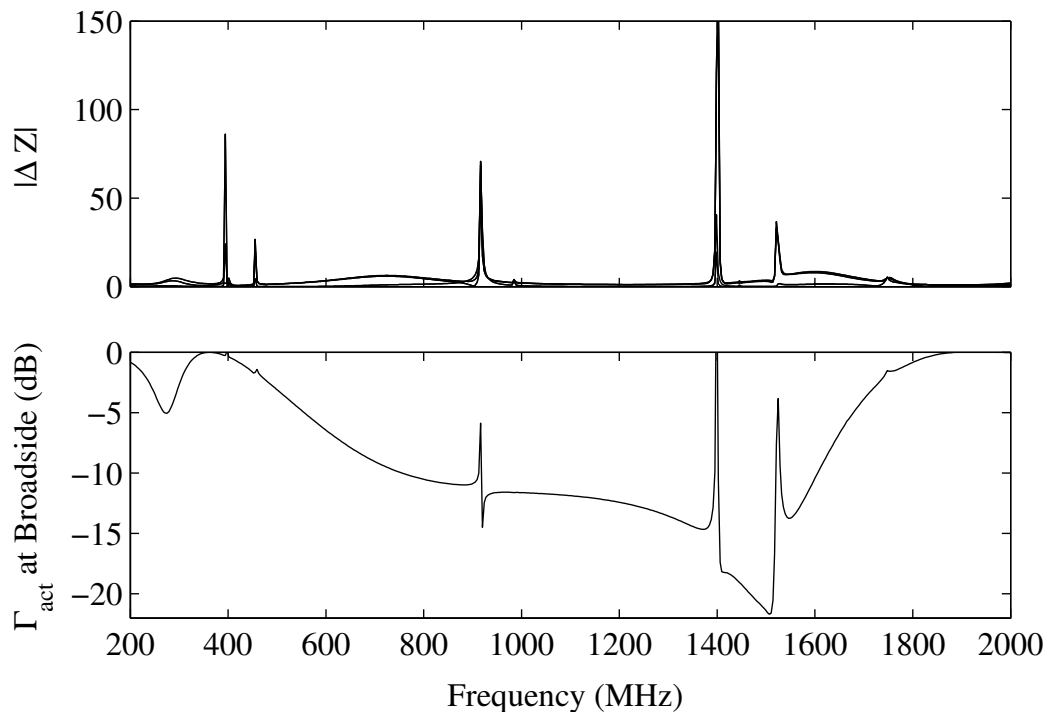


Figure 4.3: Active reflection coefficient vs difference between single-ended port impedances.

In Section 4.2 it was explained that this geometry allows for the creation of  $360^\circ$  current paths at multiple frequencies, and as a result there are multiple common-mode resonances present. In Section 3.3.1, it was shown that when the differential active impedances at the port of each element in the array are represented by two back-to-back, single-ended impedances, the difference between the single-ended active impedances of neighbouring, connected elements will determine whether common-mode currents are induced. In short,  $\Gamma_{cd} \neq 0$  when  $Z_{SEn} - Z_{SEm} \neq 0$ . Figure 4.3 shows the difference between one of the single-ended impedances of an element and all the single-ended impedances of the neighbouring elements in a unit cell along with the active reflection coefficient. All the results are for broadside radiation. It can be seen that at each frequency where  $|\Delta Z| \neq 0$ , there is a resonance in  $\Gamma_{act}$ . The resonances can therefore be attributed to the induction of common-mode currents, even if the array is fed via an ideal differential port.

The frequency range offered for this solution is seen to be from around 790 MHz to 1610 MHz, varying slightly for the four different solutions presented. This translates to a bandwidth of approximately 2:1 which is quite a reduction from the 3.8:1 that was achieved with the single-polarized case.

This performance penalty could be attributed to the optimiser struggling to optimise around the common-mode resonances. From Figure 4.2 it can be

seen that for the optimal case, the first resonance occurs at 434 MHz, where the magnitude of  $\Gamma_{act}$  suddenly falls to -13.66 dB. This flags a false positive within the optimiser that the lower frequency goal has been met. The upper frequency is at 1605 MHz which is also inside the prescribed band, resulting in a false optimal parameter set being identified.

Future work planned on this topic includes either identifying a method by which the optimiser can be forced to optimise around the resonances, or to include the common-mode (CM) filter, which is the topic of Chapter 5, in the optimisation. These CM filters were excluded from the optimisations due to the dramatic increase in CPU-time their inclusion triggered. It was therefore not deemed practical to attempt to find an optimal solution with the CM filter included in the simulation model.

Detailed investigations into optimisation methods fall outside the scope of this dissertation, so it was decided to continue verifying other aspects of the design using the sub-optimal parameter set. The optimisation exercise did however indicate that there are similarities between the basic shape of the dual-polarized  $\Gamma_{act}$  and that of the single-polarized  $\Gamma_{act}$ . This suggests that similar bandwidth performance could be realised should a true optimal solution be found.

Since starting with an optimal parameter set will necessarily result in worsening impedance performance with scan angle, it was hypothesized that starting with a sub-optimal parameter set might result in an improvement of the overall impedance scan performance. In theory, the change in relative element length and pitch seen by the incoming wave-front could improve the overall relationship between the design parameters, resulting in improved performance for off-broadside scan angles. This theory is elaborated upon in Section 4.4.1.2.

In the next section, simulation results of the dual-polarized DDA will be discussed in more detail.

## 4.4 Results

As was stated in the previous section, the differences between the optimal results and that of the three practical parameter sets were minimal. It was therefore decided to base the reference design for the dual-polarized DDA on practical parameter set 1.

### 4.4.1 Impedance Bandwidth

#### 4.4.1.1 Broadside

The active reflection coefficient of the infinite array can be seen in Figure 4.4. As was stated above, a bandwidth of approximately 2:1 has been achieved.

It is believed that with an improved optimisation strategy the achievable bandwidth can be improved.

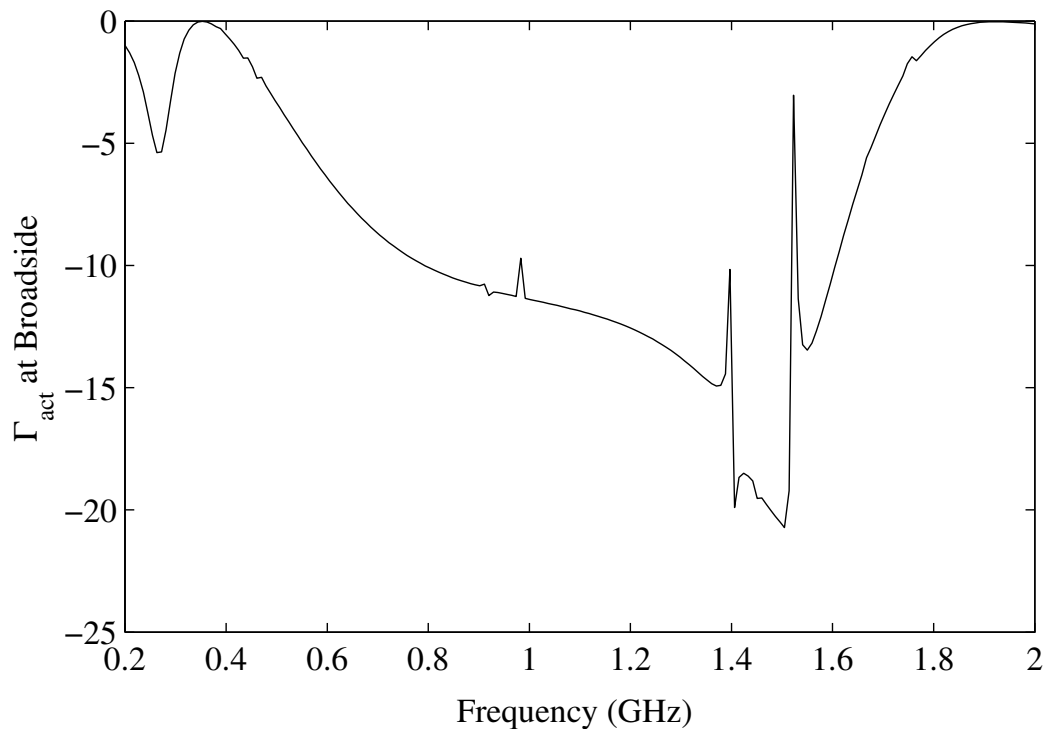


Figure 4.4: Active reflection coefficient at broadside

#### 4.4.1.2 Scan Performance

As with the single-polarized DDA, the effect scanning along the  $E$ -plane and  $H$ -plane has on the active reflection coefficient was also investigated. The same method that was used in Section 3.5.1.2 to determine the active reflection coefficient using incident plane waves was used again. Since the structure is dual-polarized, the two experiments were adapted to include data illustrating both the co- and cross-polar scan performance.

For each experiment, a visualisation of the scan range is given. The figures show a unit cell of a dual-polarized DDA with blue arrows indicating the direction of propagation for a specific data set, and red arrows indicating the polarization. Due to the geometrical constraints of the dual-polarized DDA, each unit cell contains 4 parallel pairs of overlapping dipole elements. In each case, the pair of elements highlighted in green indicates the pair of elements under investigation, which will have either co- or cross-polar orientation with regard to the incoming wave-front. The periodic boundary boxes are not displayed in order to improve visibility of the actual array surface.



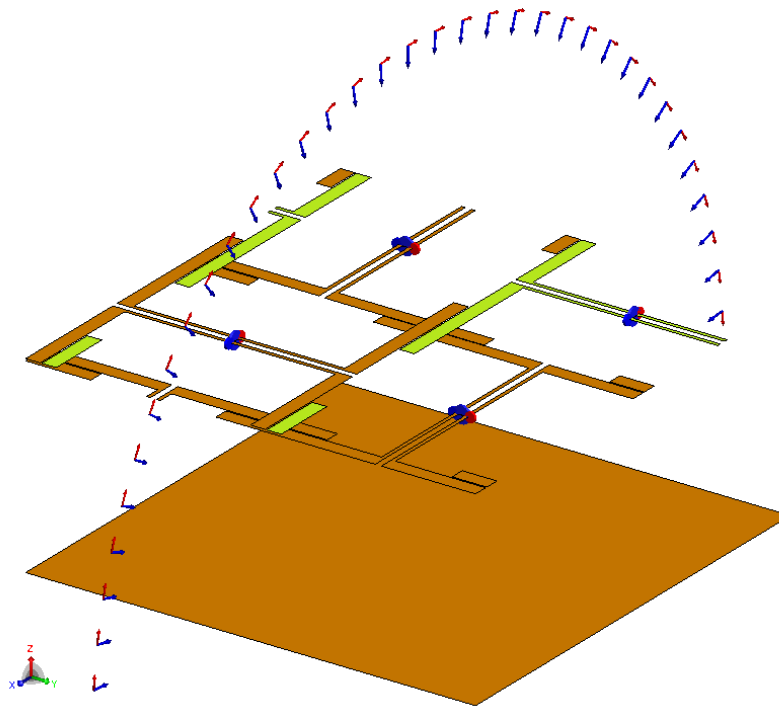
**E-plane Scan:**

Figure 4.5: Visualisation of the tested scan range along the  $E$ -plane, with a co-polarized incoming wave-front.

The visualisation of the incoming wave-front relative to the element pair under investigation for the co-polar  $E$ -plane scan is shown in Figure 4.5, and the results are shown in Figure 4.6. For the results, the same “top-view” format that was used in Chapter 3 is used again, but the resolution was improved to include an intermediate level where  $-10 \text{ dB} \leq \Gamma \leq -7.5 \text{ dB}$ . The colour mapping is indicated on the figure. As with the single-polarized case, the  $y$ -axis shows the frequency and the  $x$ -axis the scan angle.

It can be seen that the bandwidth performance is relatively stable across a scan range within  $\approx 45^\circ$  off zenith. A further increase in scan angle results in a decrease in bandwidth to the higher section of the broadside in-band frequency range. This phenomenon was also displayed with the single-polarized case and is because the relative size of the array elements seen by the incoming wave-front decreases as the scan angle increases. The centre-frequency of the array will therefore increase accordingly, resulting in the shift towards a higher frequency band. The relative inter-element spacing seen by the incoming wave-front also decreases as the scan angle increases.

In the case of the single-polarized array, the array design parameters were close to optimal, which is not the case for this specific dual-polarized

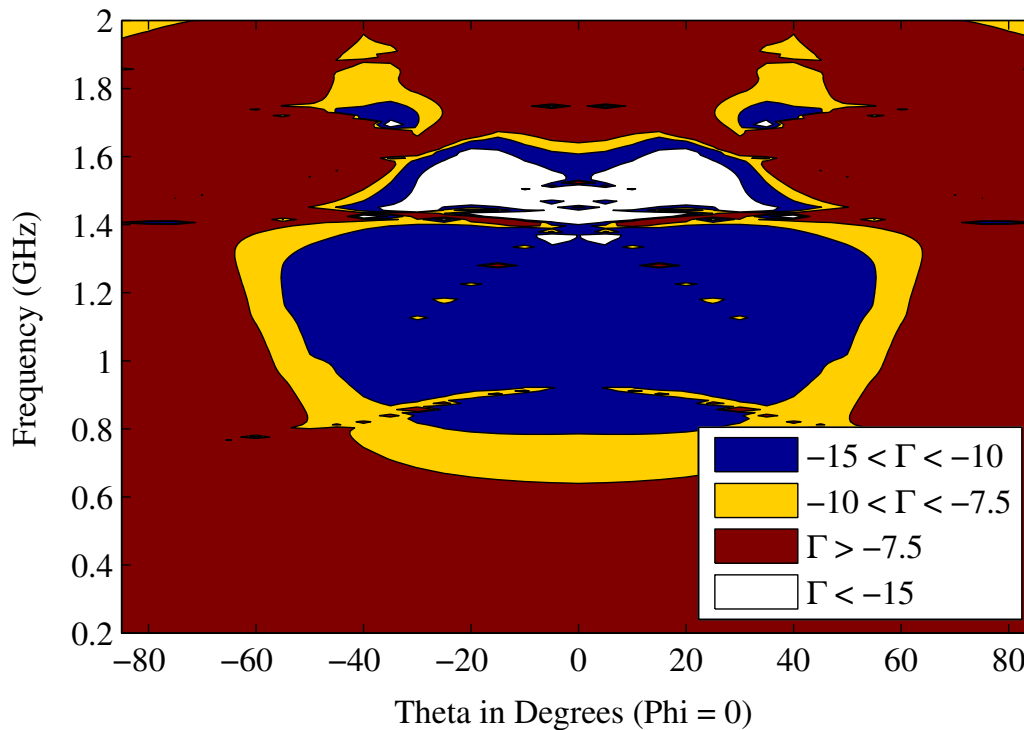


Figure 4.6: Active reflection coefficient for various scan angles along the  $E$ -plane, with a co-polarized incoming wave-front.

array as was explained in Section 4.3. For the optimal case, when scanning along the  $E$ -plane, the change in relative element length and pitch will in each case result in a sub-optimal arrangement for off-broadside scan angles. When starting with a sub-optimal parameter set, scanning will not necessarily result in worsening performance, as the act of scanning might actually improve the relationship between the design parameters.

This phenomenon is observed in Figure 4.6. When scanning off-broadside, the lower cut-off is not affected as rapidly with scan angle as in the optimised case. The upper cut-off increases up to  $\approx 20^\circ$  off broadside, and then rapidly decreases until it seems to stabilise at  $\approx 45^\circ$ . These results suggest that should the array design parameters be optimized at an off-broadside scan angle, even though it will result in a performance penalty at broadside, the overall scan performance might be an improvement above that of the broadside-optimized case. Future work planned on the project includes a more rigorous investigation of this theory.

The visualisation of the incoming wave-front relative to the element pair under investigation for the cross-polar  $E$ -plane scan is shown in Figure 4.7, and the results are shown in Figure 4.8. For good performance, the array should be “blind” to incoming signals that are cross-polarized, meaning that the currents and voltages seen at the ports of the cross-polarized ele-

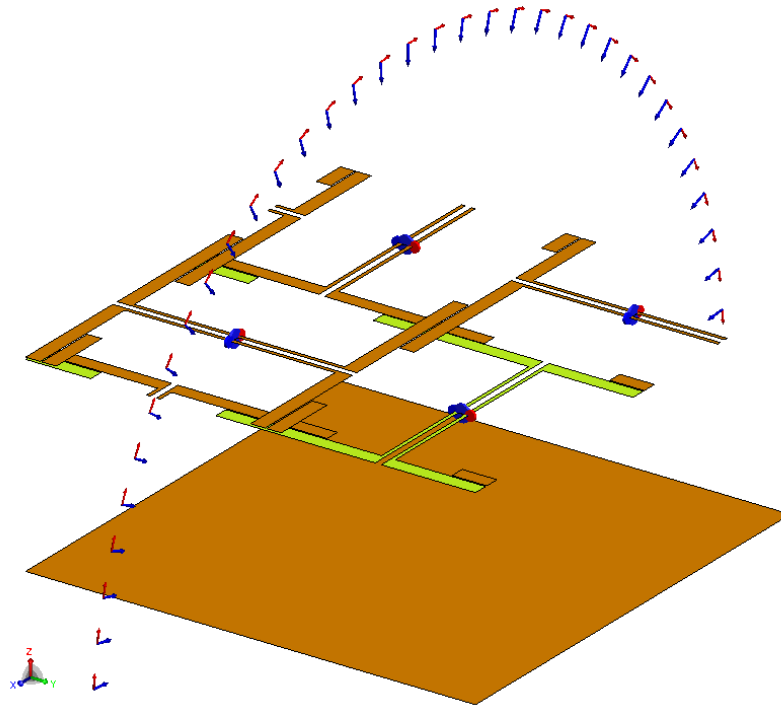


Figure 4.7: Visualisation of the tested scan range along the  $E$ -plane, with a cross-polarized incoming wave-front.

ments should result in an impedance mismatch with the receiver chain. In Figure 4.8, a higher  $\Gamma$  is therefore associated with better performance. It can be seen that, apart from the common-mode resonances which manifests itself as spots or thin strips of “good” performance in this image format, most of the cross-polarized signals will be mismatched to the receiver.

### H-plane Scan:

The visualisation of the incoming wave-front relative to the element pair under investigation for the co-polar  $H$ -plane scan is shown in Figure 4.9, and the results are shown in Figure 4.10. In this case, the relative element length seen by the incoming wave-front does not change, but the inter-element spacing along the  $y$ -axis does. As was displayed in Chapter 3, the performance of the array is dependent on the overall relationship between design parameters. Since the starting point in this case is sub-optimal, and the relative length-pitch relationship is altered as a result of scanning, the performance degradation with scan-angle happens at a faster rate compared to that of the  $E$ -plane scan.

Figures 4.11 and 4.12 depict the visualisation of the incoming wave-front relative to the element pair under investigation for the cross-polar  $H$ -plane scan, and the results of the cross-polar  $H$ -plane scan respectively. As was the case with the cross-polar  $E$ -plane scan, the desirable result is that the

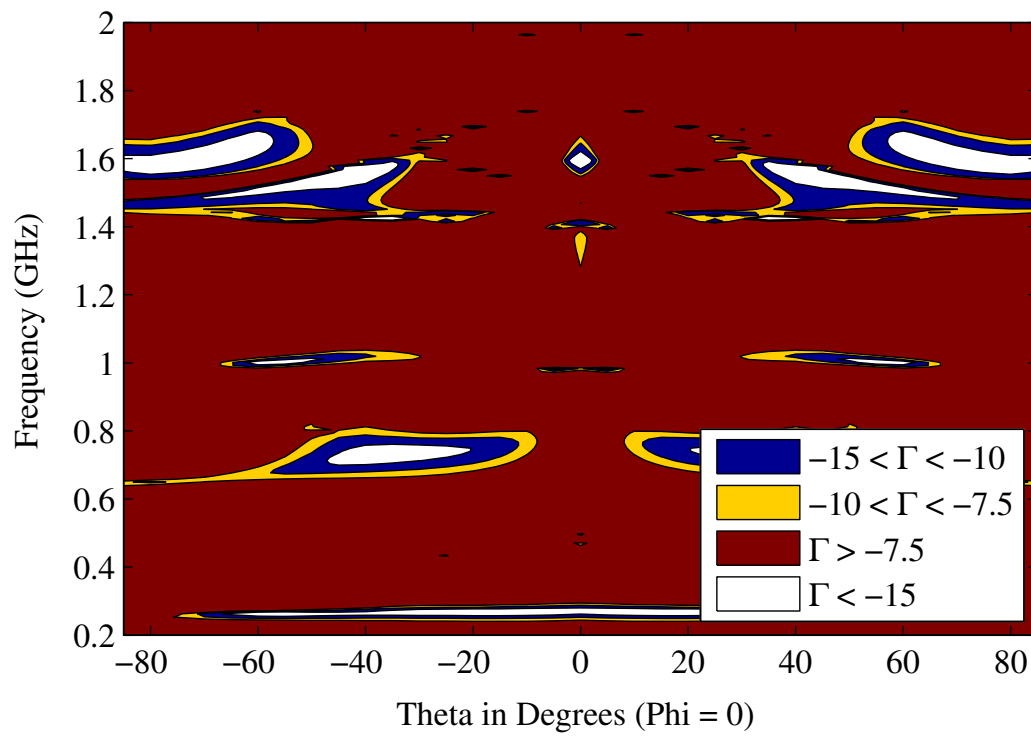


Figure 4.8: Active reflection coefficient for various scan angles along the  $E$ -plane, with a cross-polarized incoming wave-front.

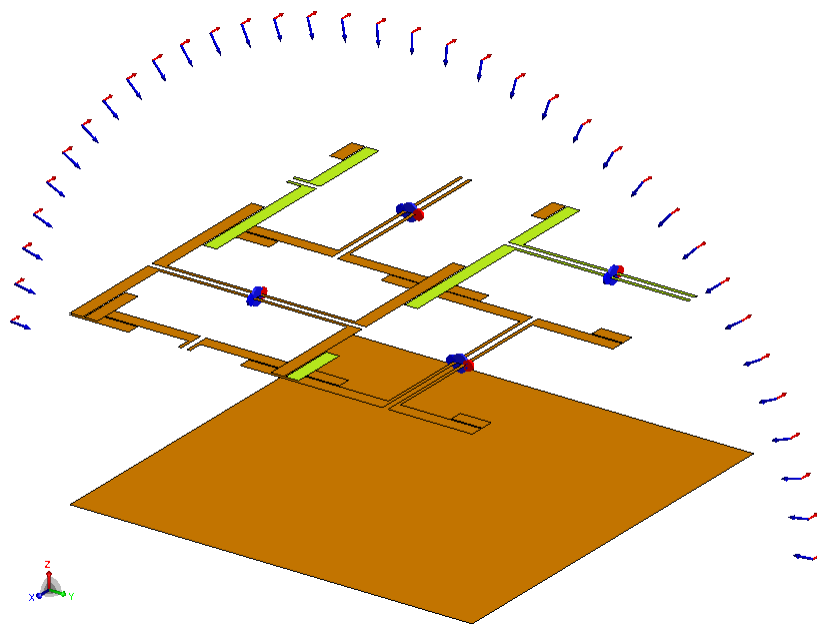


Figure 4.9: Visualisation of the tested scan range along the  $H$ -plane, with a co-polarized incoming wave-front.

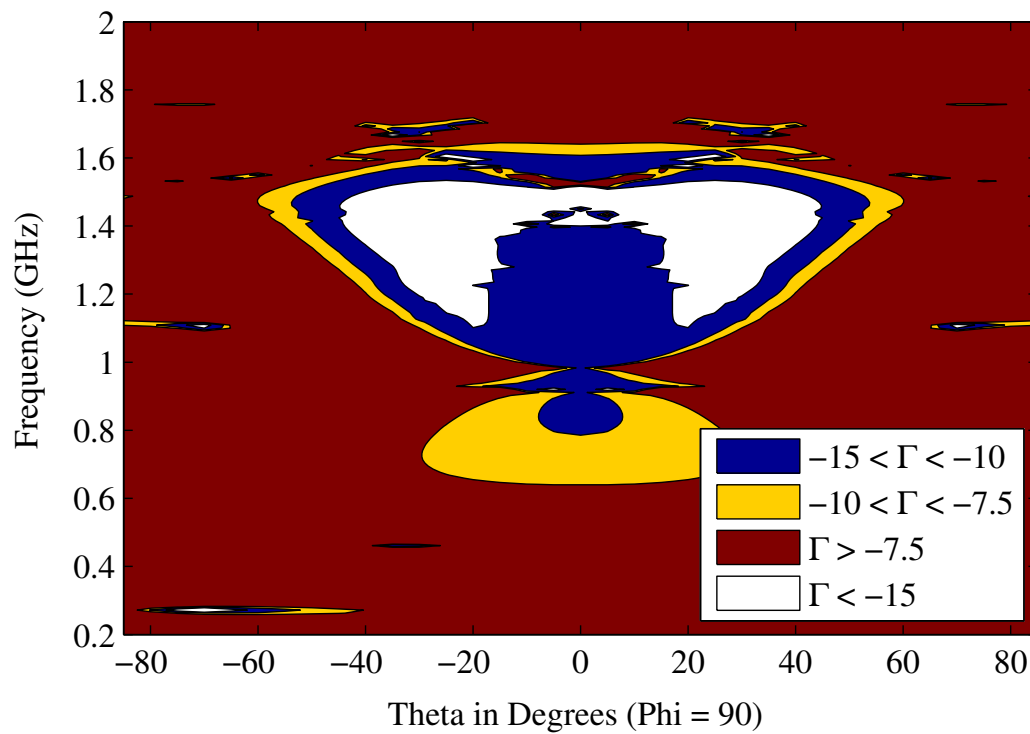


Figure 4.10: Active reflection coefficient for various scan angles along the  $H$ -plane, with a co-polarized incoming wave-front.

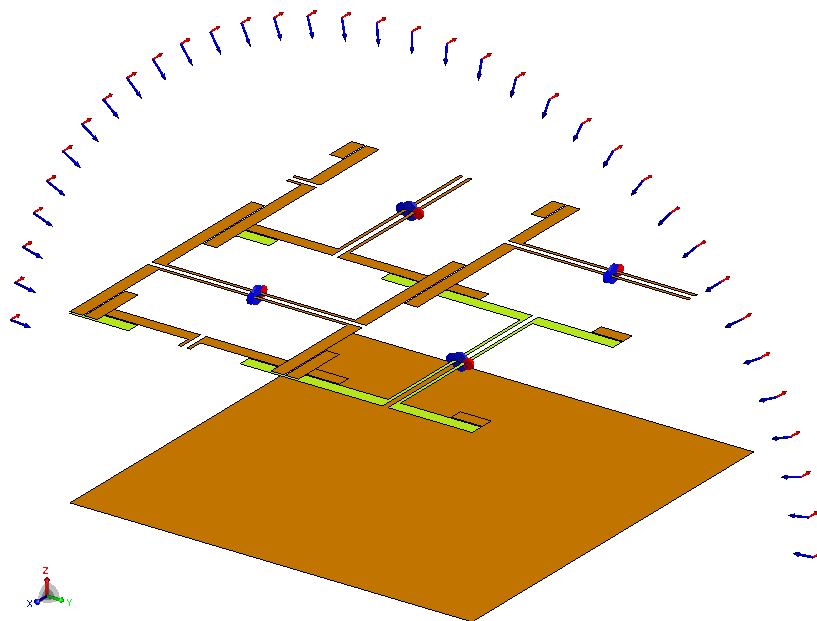


Figure 4.11: Visualisation of the tested scan range along the  $H$ -plane, with a cross-polarized incoming wave-front.

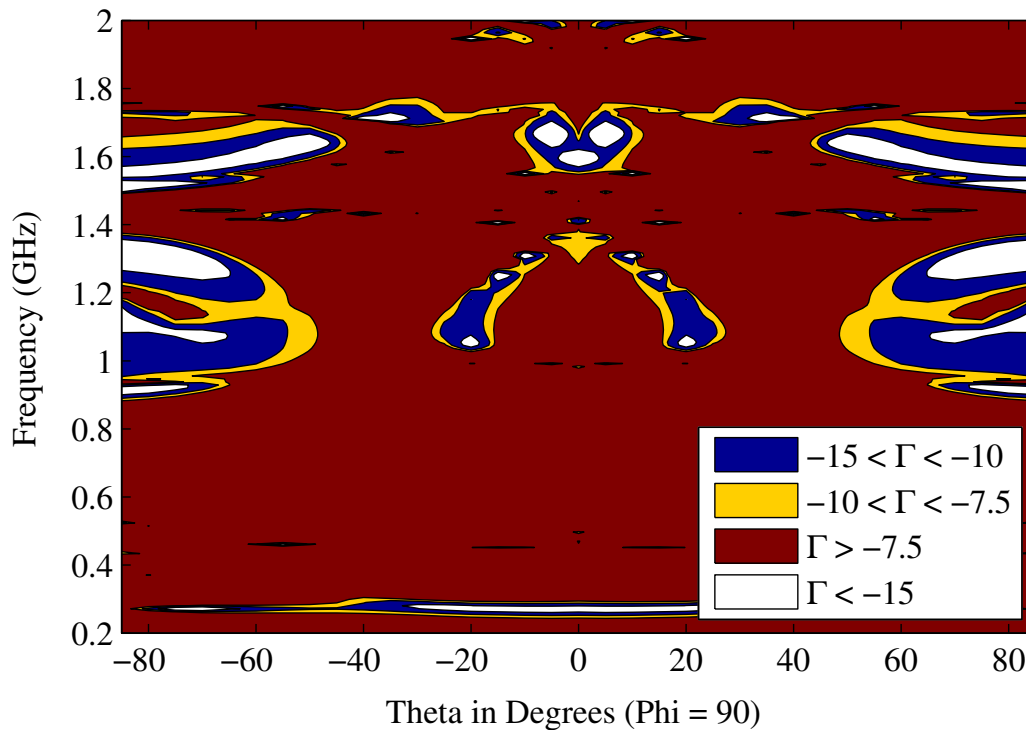


Figure 4.12: Active reflection coefficient for various scan angles along the  $H$ -plane, with a cross-polarized incoming wave-front.

currents and voltages induced at the ports of the elements due to a cross-polar incoming wave, should result in an impedance mismatch between the antenna and the receiver.

From the figure, it is clear that for a scan range of  $-45^\circ \leq \theta \leq 45^\circ$ , the impedance attributed to the cross-polar incoming wave seem to be adequately mismatched to that of the receiver. Some common-mode resonances are also present.

When the scan angle is increased to above  $\approx 45^\circ$  from zenith, the resultant array impedance become better matched to the receiver. This is because the thin feed-lines are perceived to be the antenna-elements by the incoming wave-front. Closer to zenith, the phase difference of the signal received by neighbouring elements of the same polarization orientation is small enough to allow for currents induced on the feed lines to cancel out. When the scan angle increases towards the horizon, the phase of the currents induced on neighbouring elements will not allow for the same level of cancellation.

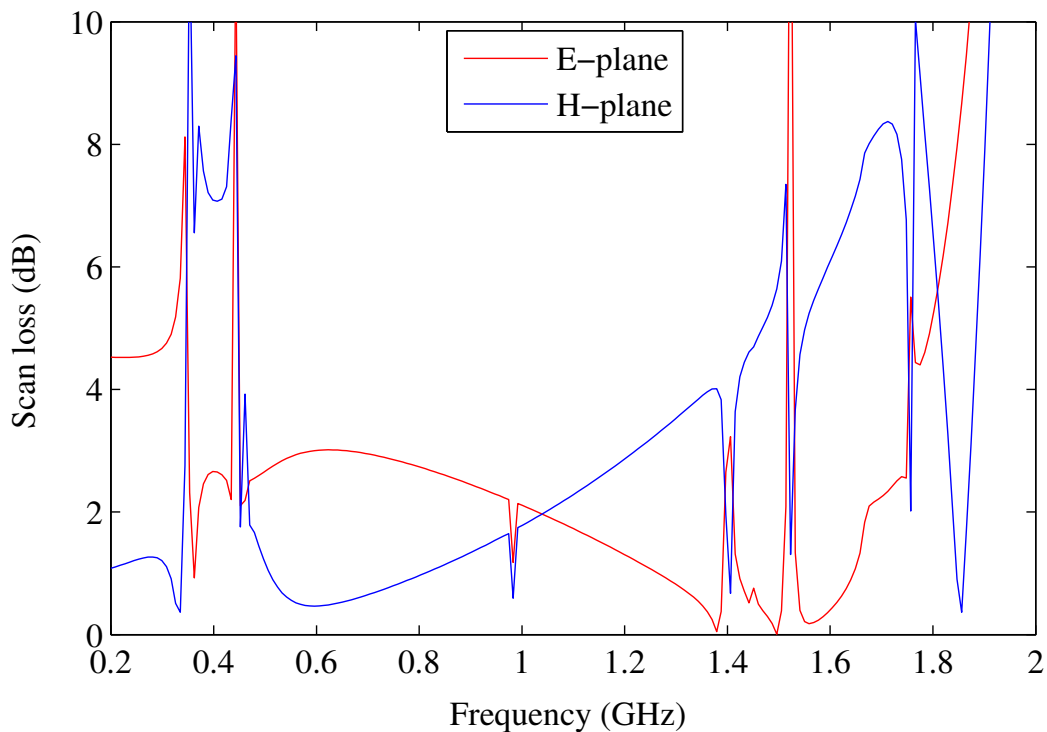


Figure 4.13: Scan loss for  $\theta_0 = 45^\circ$ , on the  $E$ -plane and  $H$ -plane

## 4.4.2 Gain Performance

### 4.4.2.1 Scan Loss

As explained in Section 3.5.2.1, the radiation pattern of a large array is completely dominated by the array factor. As a result, the scan loss would be a more sensible metric with which scan performance can be measured. In this case the performance penalty of the co-polar gain of the embedded element is measured when scanning to  $45^\circ$  off broadside along both the  $E$ - and  $H$ -planes. An angle of  $45^\circ$  was chosen in order to compare the results with that of other AA topologies [63].

The results are shown in Figure 4.13. The discontinuities that can be observed correspond to the frequencies where common-mode resonances are observed either at  $\theta = 0^\circ$  or  $\theta = 45^\circ$ . It can be seen, bar the CM resonances, that the  $E$ -plane scan loss is below 5 dB across all the in-band frequencies. This is in line with the scan loss of other AA designs [63] where a loss of between 2 dB and 5 dB is demonstrated at a scan angle of  $45^\circ$ .

For the  $H$ -plane scan, the radiation pattern is relatively flat across the hemisphere at lower frequencies, since the ground plane at these frequencies is closer than  $\frac{\lambda}{4}$  from the array surface. As a result, the scan-loss will also be relatively low. At higher frequencies, the array surface is higher than  $\frac{\lambda}{4}$  above the ground plane, resulting in a radiation pattern that is not

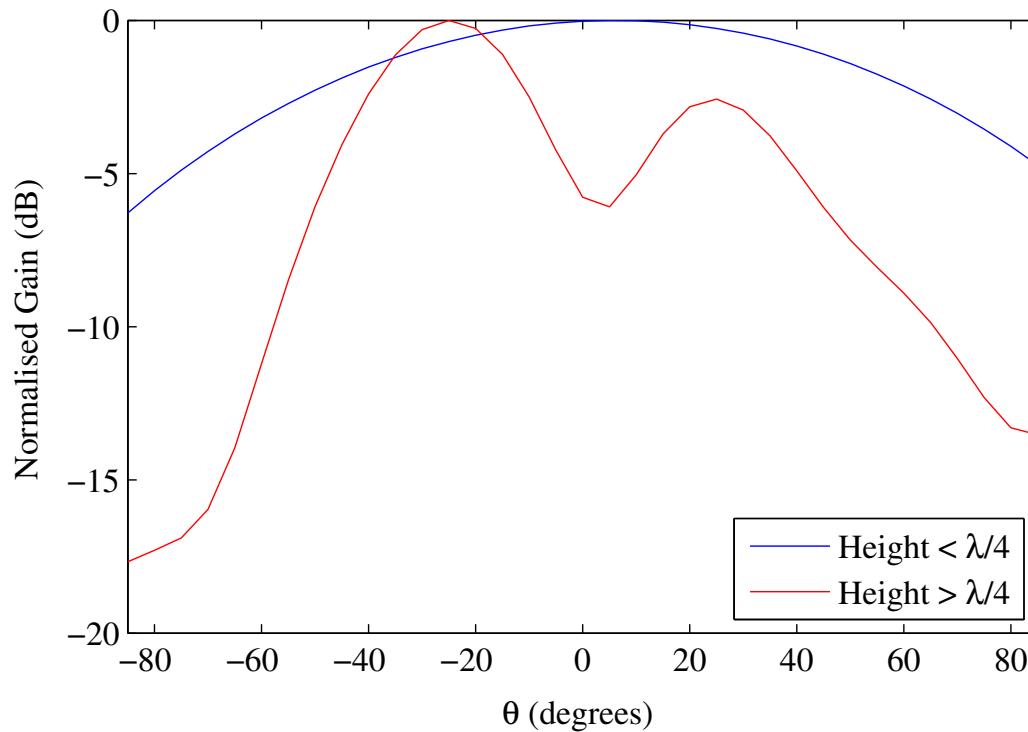


Figure 4.14: Normalised co-polar H-plane gain pattern for two relative ground plane heights

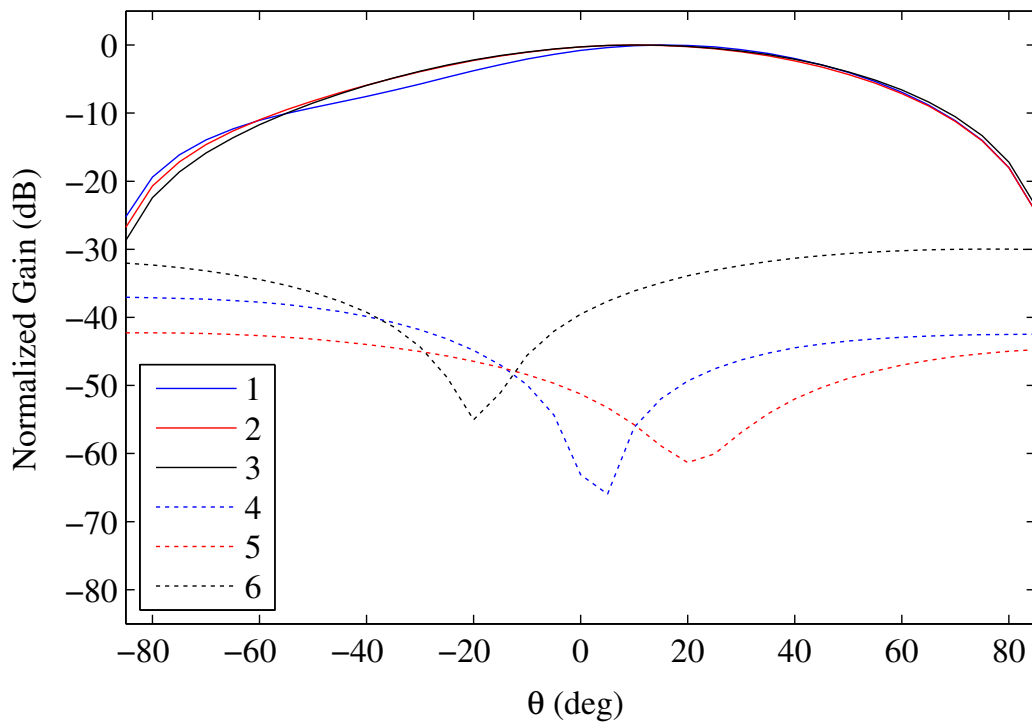
flat across the  $H$ -plane any more. This phenomenon can be seen in Figure 4.14.

The observation regarding the relative distance between the ground plane and the array surface is true for both the  $E$ -plane and  $H$ -plane axes, however it is more pronounced along the  $H$ -plane since the beam is relatively flat across the hemisphere compared to that of the  $E$ -plane at lower frequencies.

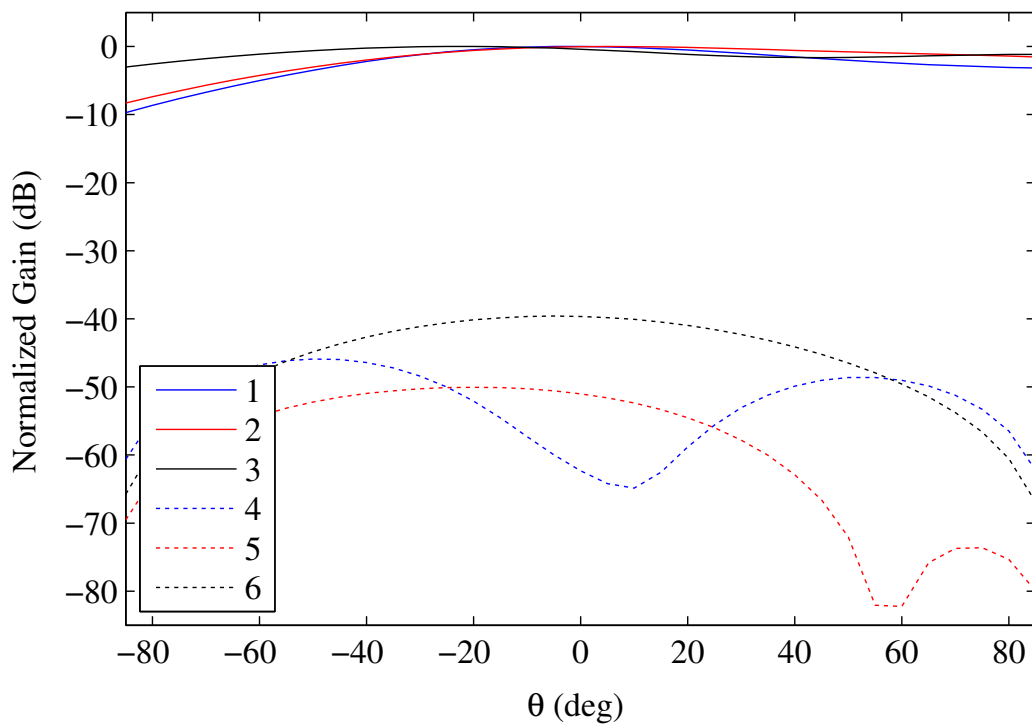
#### 4.4.2.2 Cross-Polarization

Figures 4.15a, 4.15b and 4.15c illustrate the co-polar and cross-polar gain of the embedded element for scan angles of  $-85^\circ \leq \theta \leq 85^\circ$  along the  $E$ -plane,  $H$ -plane and  $D$ -plane respectively, at 3 different frequencies. It can be seen that good cross-polarization performance is demonstrated in all three planes for a scan range of  $-45^\circ \leq \theta \leq 45^\circ$ . The cross-polarization performance demonstrated in these figures are also in line with that of other AA designs [1,64].

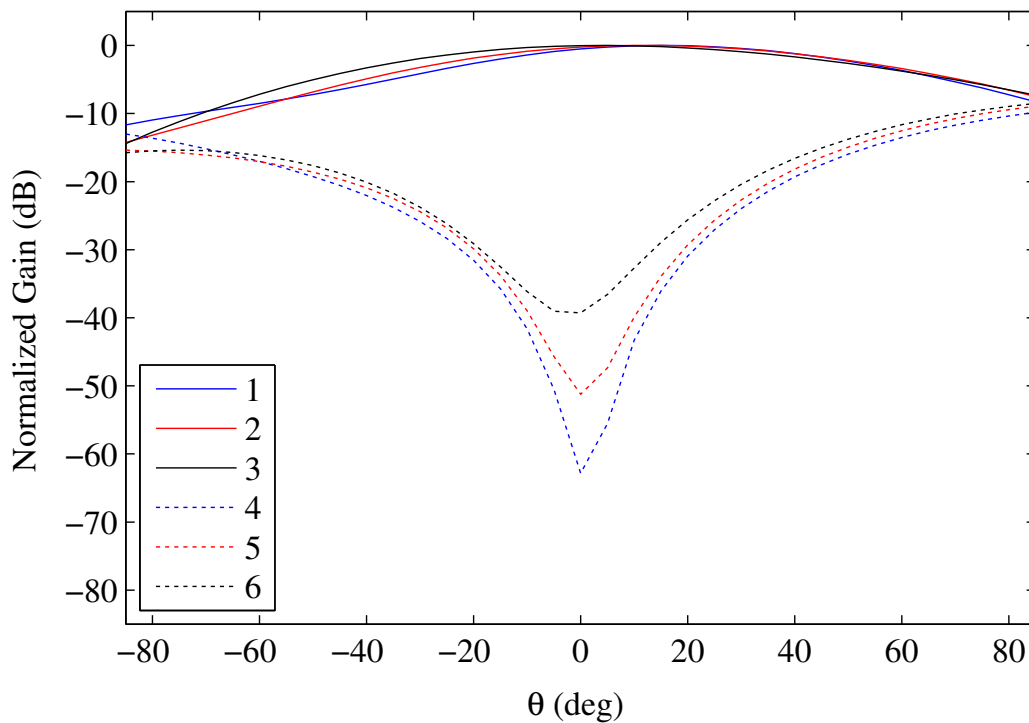




(a) E-plane



(b) H-plane



(c) D-plane

Figure 4.14: Normalised co-polar and cross-polar gain patterns for an embedded element in an infinite array. The trace indices for all three plots are as follows: (1) Co-pol at 1 GHz, (2) Co-pol at 700 MHz, (3) Co-pol at 500 MHz, (4) Cross-pol at 1 GHz, (5) Cross-pol at 700 MHz, (6) Cross-pol at 500 MHz

## 4.5 Conclusion

The dual-polarized DDA was introduced in this chapter. The structure is an expansion of the single-polarized DDA to include a second, orthogonal polarization. The elements were also combined in pairs of 2 in order to reduce the characteristic impedance of the array to accommodate the characteristic impedance limits posed by typical low loss transmission lines. While doing this might limit the scan range, especially along the  $E$ -plane, it was decided that the potential cost-saving on system level justified further investigation into this solution.

The optimisation of the dual-polarized structure proved to be challenging since the optimiser struggled to optimise around the common-mode resonances. It was therefore decided to address the optimisation issues as part of a future project and to continue verifying other aspects of the design using the sub-optimal parameter set.

The results of the active reflection coefficient as a function of frequency

and scan-angle of the sub-optimal design suggested that better scan performance could be obtained if the structure is optimised for off-broadside impedance performance. This hypothesis will be explored as part of with the optimisation study planned for the near future.

The scan loss and cross-polarization performance displayed were in line with other AA designs.

## Chapter 5

# The Common-Mode Suppressing Feed

### 5.1 Introduction

In a dense antenna array, such as the Dense Dipole Array (DDA), the spacing between antenna elements is closer than  $\frac{\lambda}{2}$ . The individual elements are also connected to one another, either directly [66, 67] or capacitively [1, 68]. The combination of the inter-element spacing of  $\frac{\lambda}{2}$  and the fact that the antenna elements are connected provide for current-paths to be created that frequently result in the introduction of common-mode currents at the feed of each antenna element. This phenomenon is illustrated in Figure 5.1.

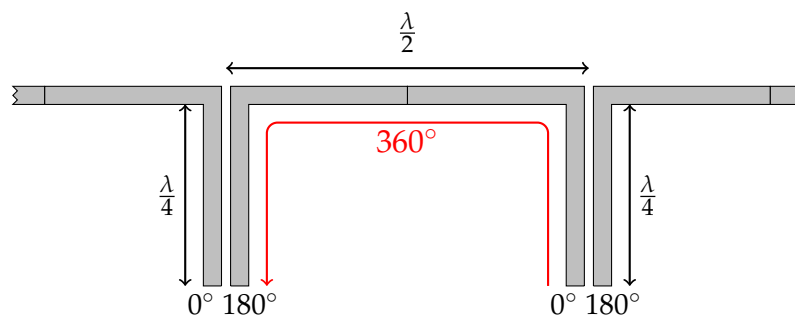


Figure 5.1: Fields in a Microstrip-Slotline Transition During Differential Mode Operation

The individual antenna elements are fed differentially, which means that the each dipole leg is excited  $180^\circ$  out of phase with its partner. Since the elements are placed  $\frac{\lambda}{2}$  from their neighbours, and are typically also placed  $\frac{\lambda}{4}$  above a reflector, a  $360^\circ$  current path is formed between the  $0^\circ$  leg of one element and the  $180^\circ$  leg of its neighbour at a certain frequency, that gives

rise to a common-mode resonance at that frequency. During scanning operations, the relative phase-shift between neighbouring elements is adjusted, altering the frequency at which this common-mode resonance will occur. This was seen in Figures 3.33 and 3.35 in Chapter 3. The length of the feed lines will also directly affect the frequency of the resonance as shown in Figure 5.2, where a single polarized DDA is fed by lines of varying lengths. Since so many factors influence the frequency at which the resonance occurs, it is difficult to design a broadband scanning array around it.

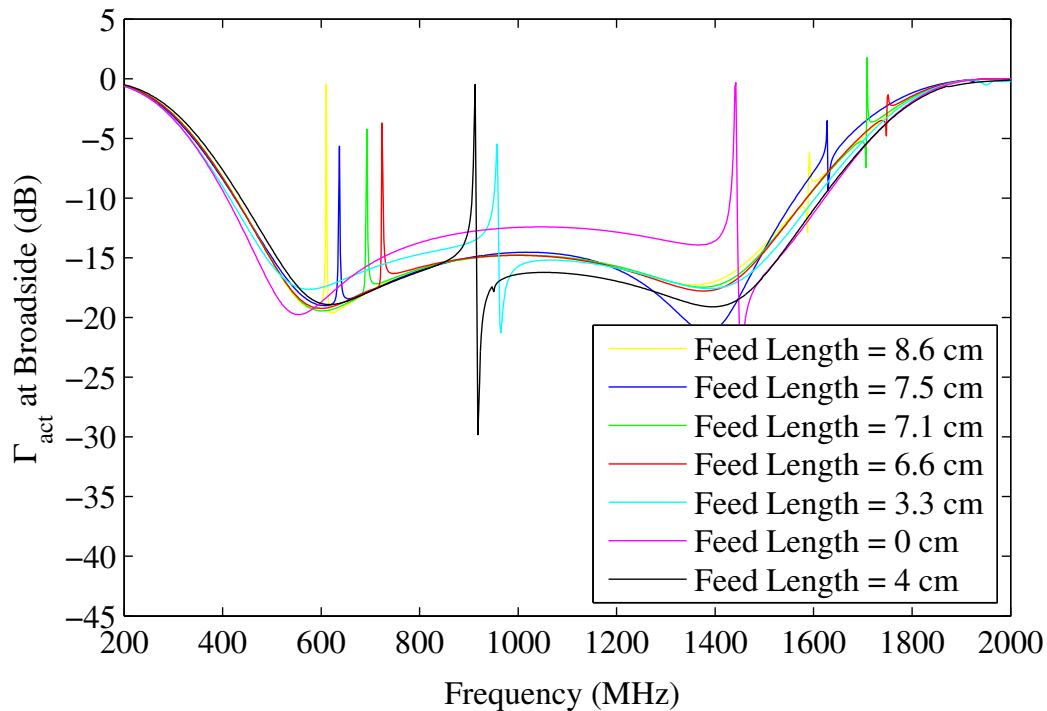


Figure 5.2: Active reflection coefficient at for a single-polarized DDA with varying feed lengths

Cavallo et al. proposed a solution to this problem in [17] consisting of a  $180^\circ$  microstrip loop that couples to a slot, that in turn couples to an identical  $180^\circ$  microstrip loop again. This method proved very effective in cancelling out common-mode currents over a wide bandwidth; however, since the  $180^\circ$  phase-shift between the two ports of the differential feed is “hard-wired” as a microstrip line, the two ports will only have  $180^\circ$  phase-shift at a very specific frequency. As a result, the differential-mode bandwidth of this solution is quite narrow. Another draw-back of this design is that continuous current-paths in the order of a wavelength still exist when the inter-element spacing is close to  $\frac{\lambda}{2}$ . This continuous current path will therefore still give rise to common-mode propagation at certain frequencies.

In this project, the original design by Cavallo et al. is adapted to widen the differential-mode bandwidth and to address the continuous current path that occurs at an inter-element spacing of  $\frac{\lambda}{2}$ .

Section 5.2 provides the theoretical background into the field theory involved in the design being presented. The design of the feed network is discussed in Section 5.3. Section 5.4 gives a mathematical background into the measurement procedure that was followed. The results of the simulations and measurements are given in Section 5.5 and Section 5.6 concludes.

## 5.2 Theoretical Background

Reviewing the basic, “narrowband” transition between a single microstrip line and a slotline will aid in the understanding of how energy is transferred between these two types of transmission lines. The transition consists of two quarter wavelength stubs placed orthogonally to one another. This configuration can be seen in Figure 5.3.

Figure 5.3a illustrates the magnetic fields induced by the current in the microstrip line, with Figure 5.3b illustrating the resultant electric field in the plane of the slot. For simplicity, the discontinuity in the  $H$ -fields due to the transition from an air-dielectric to that of the substrate is ignored. In the Figures,  $z = 0$  is in the plane of the slot, and  $x = 0$  is in the centre of the microstrip. From the two figures, it is clear that only the  $z$ -component of the  $H$ -field ( $H_z$ ) will result in an  $E$ -field in the plane of the slot.

It can be shown that the balance of the decrease of the field-strength and the increase in the  $z$ -component with distance from the conductor will result in a maximum  $H_z$ -field at  $x = h$ , where  $h$  is the height of the substrate [65].

When another microstrip ending in a quarter wave stub is added below the slot-plane as illustrated in Figures 5.4 and 5.5, the strength of the  $E$ -field induced in the slot will be determined by the sum of the  $H_z$ -fields of both conductors. The phase relationship between the currents in the two conductors at the transition will therefore determine the strength of the  $E$ -field in the slot.

Figure 5.4 depicts the situation where the two currents are in-phase at the transition. It can be seen that the resultant  $H_z$ -fields will add constructively to induce an  $E$ -field that will propagate along the slotline.

In the second case, shown in Figure 5.5, where the currents are  $180^\circ$  out of phase with one another at the transition, the  $H_z$  fields will cancel, resulting in no  $E$ -field being induced.

An equivalent circuit diagram demonstrating the energy transfer via electromagnetic fields in this symmetrical model can be adapted from models proposed by Knorr [69] and Schüppert [70]. This model can be seen in Figure 5.6. The virtual short-circuit of the model in [70] is represented by a transformer with winding ratio  $n$ .

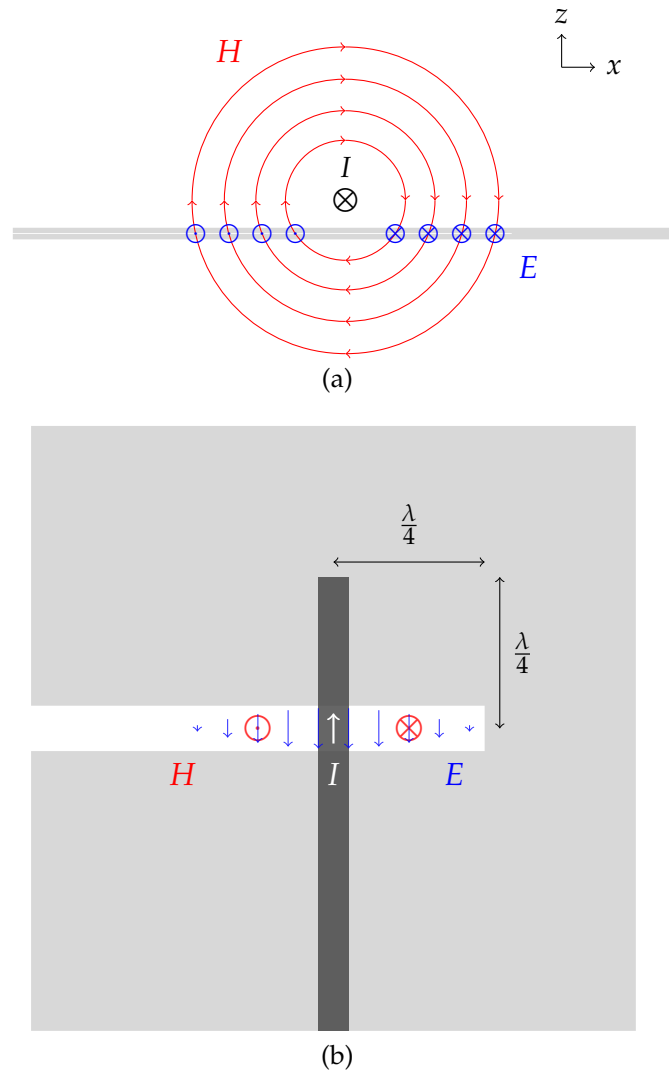


Figure 5.3: The Basic Microstrip-Slotline Transition: (a) Side View; (b) Top View.

Assume now that the two microstrip lines in Figure 5.6 are the two lines of a differential pair.  $I_D$  indicates the differential-mode and  $I_C$  the common-mode components of the total current in the differential pair. It can be seen that the two components of  $I_D$  add in-phase and the two components of  $I_C$  cancel. Only the differential component of the current will therefore be coupled to the slotline, while the common-mode component will be suppressed.

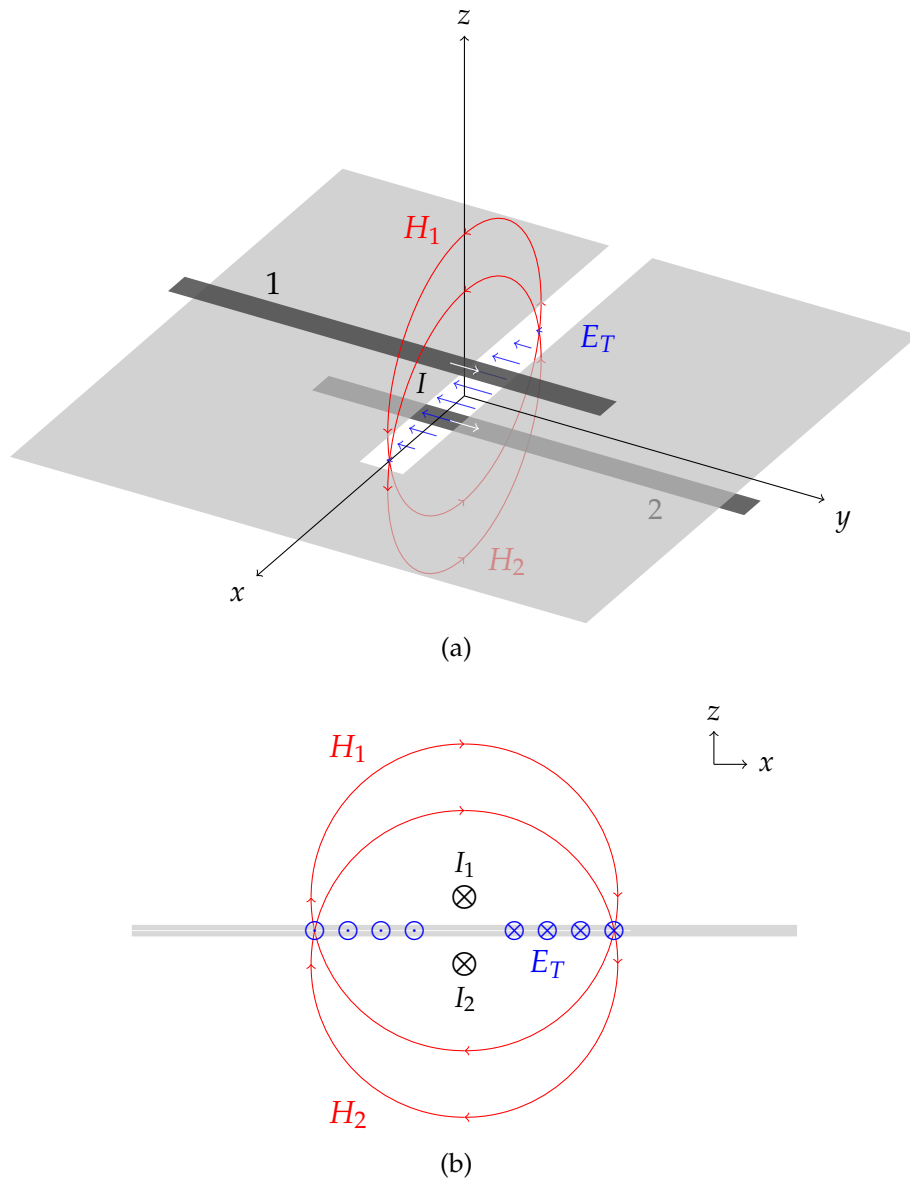


Figure 5.4: Fields due to in-phase currents in a Symmetrical Microstrip-Slotline Transition: (a) 3D View; (b) Side View.



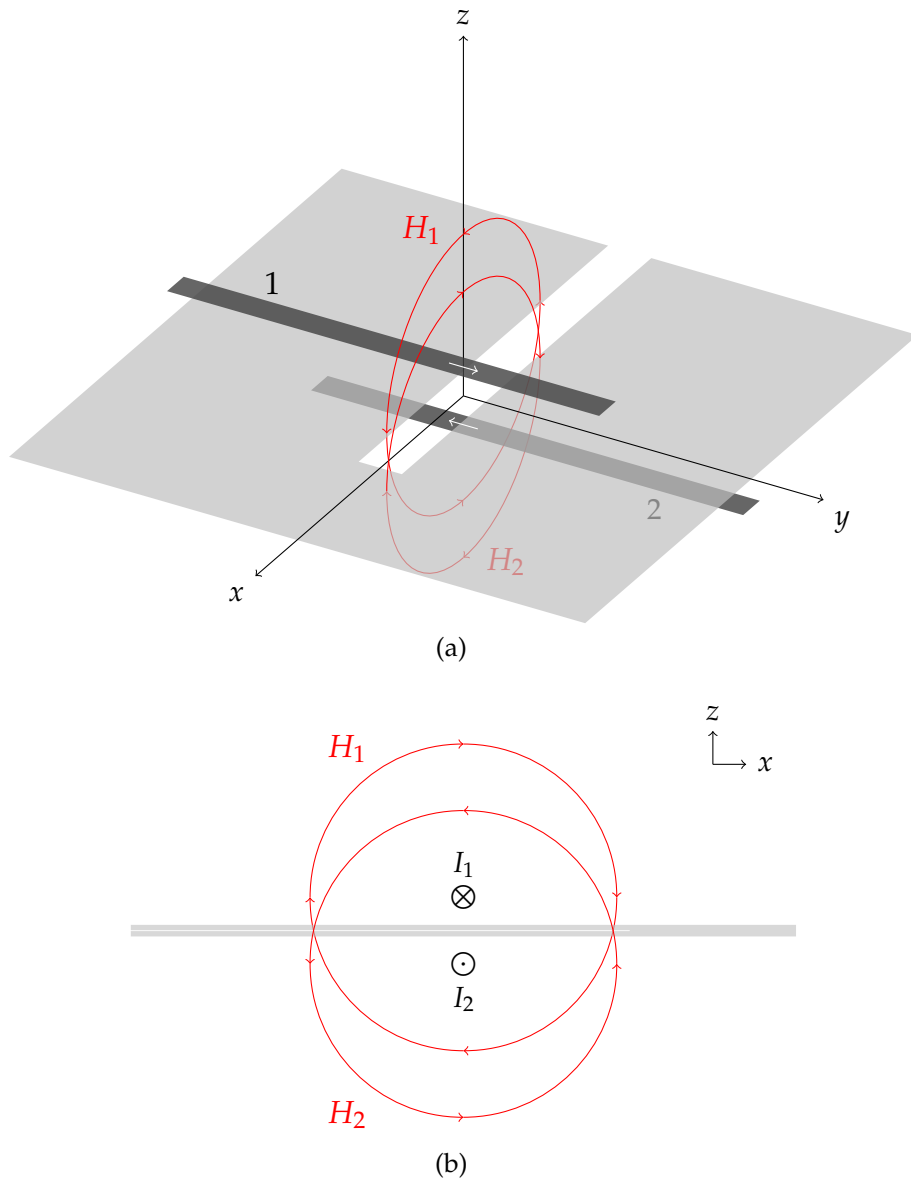


Figure 5.5: Fields due to 180° out of phase currents in a Symmetrical Microstrip-Slotline Transition: (a) 3D View; (b) Side View.

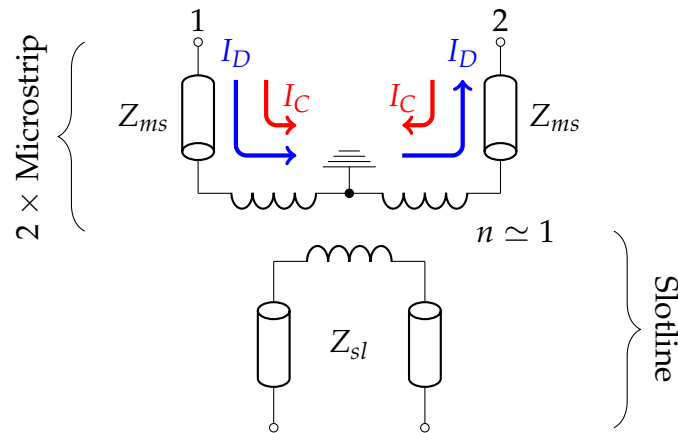


Figure 5.6: Equivalent circuit of a symmetrical Microstrip-Slotline Transition

Table 5.1: Antenna Specifications

Parameter	Value
Frequency Range	450 – 1450MHz
Center Frequency	1000MHz
Active Reflection Coefficient	$\leq -10\text{dB}$
Differential Reference Impedance	$150\Omega$

### 5.3 Feed Network Design

In order to improve the differential-mode bandwidth of the feed designed by Cavallo et al. in [17], the approach to bandwidth improvement for microstrip-slotline transitions by using radial/circular stubs [42,65,70–72] was followed and combined with the theory elaborated upon in Section 5.2.

The network was designed to serve as a feed for a printed antenna array with specifications given in Table 5.1. From these specifications, the requirements for the feed network were derived to ensure a comfortable overlap with additional room for error. The desired specifications for the feed network can be seen in Table 5.2.

The network consists of two back-to-back, symmetrical, wide-band, microstrip-slotline transitions. The differential microstrip lines at opposite sides of the ground plane have been split up before being guided around the slotline stub. This ensures that at the transition the differential-mode portion of the current appears to be in-phase as in Figure 5.4, while the common-mode portion appears to be  $180^\circ$  out of phase as in Figure 5.5. Since the wide-band transition is designed to imitate a  $\frac{\lambda_0}{4}$  stub for both the microstrip and slotline across all in-band frequencies, the phase difference

Table 5.2: Feed Network Specifications

Parameter	Target Value
Differential-Mode Frequency Range	400 – 1600MHz
Center Frequency	1000MHz
Differential Reference Impedance	150Ω
Differential-Mode Reflection ( $S_{d1d1}$ )	$\leq -15\text{dB}$
Differential-Mode Transmission ( $S_{d2d1}$ )	$\geq -1\text{dB}$
Common-Mode Transmission ( $S_{c2c1}$ )	$\leq -20\text{dB}$

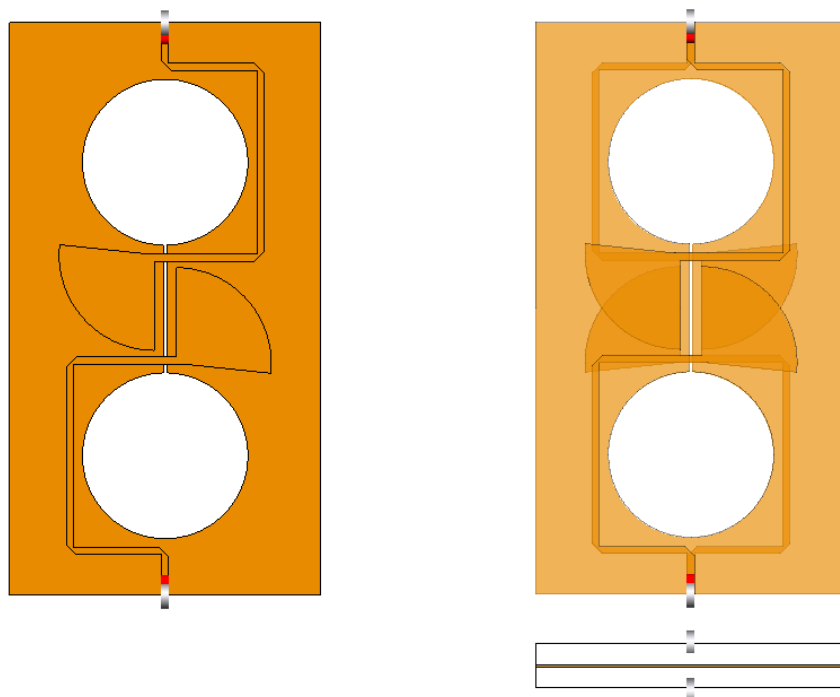


Figure 5.7: Detailed Feed Design (See text for more details)

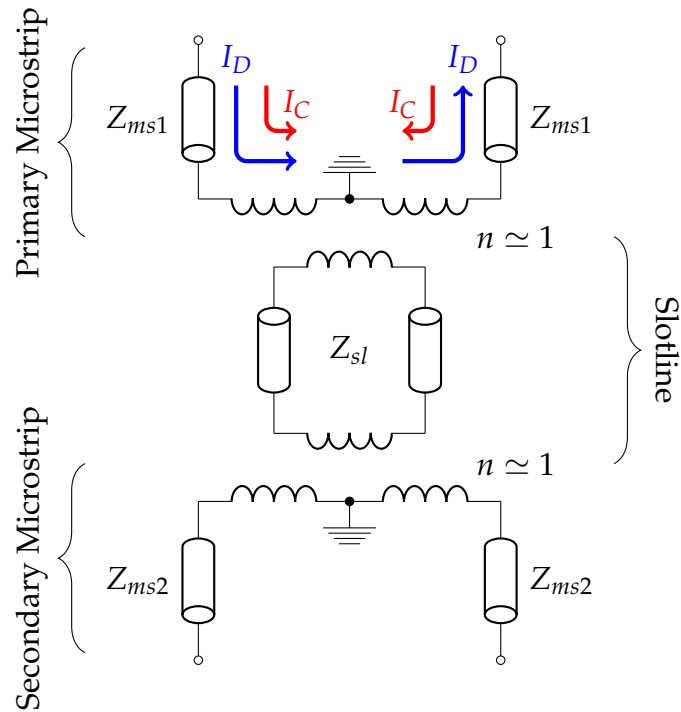


Figure 5.8: Equivalent Circuit Model of the Feed Network

between the differential-mode portion and the common-mode portion of the current will stay the same across all in-band frequencies over the entire scan range.

Since the design is intended to serve as a feed network for the DDA, the outer dimensions of the feed board were chosen to allow the feed boards to serve as mechanical support between the array and the ground plane. This printed array will be placed at  $\frac{\lambda_0}{4}$  (75mm) above a ground plane and the spacing between the elements is 80mm. More details on how this design is used to feed the DDA is given in Chapter 6.

Figure 5.7 gives an overview of the symmetrical design of the feed network. The figure on the left shows a model of the design, and the figure on the right is a transparent view of the same model. Below the transparent model is a side view showing the details of the differential feed arrangement.

The equivalent circuit model of the network is depicted in Figure 5.8. As explained in Section 5.2, the energy from the differential-mode currents in the primary microstrip pair will be transferred to the slot, while that of the common-mode currents will be suppressed. Only the differential-mode energy will therefore propagate along the slotline and will be transferred onto the secondary microstrip pair.

Figure 5.9 shows a step-by-step reduction of the equivalent circuit of Figure 5.8. This reduction is helpful in determining the characteristic impedances

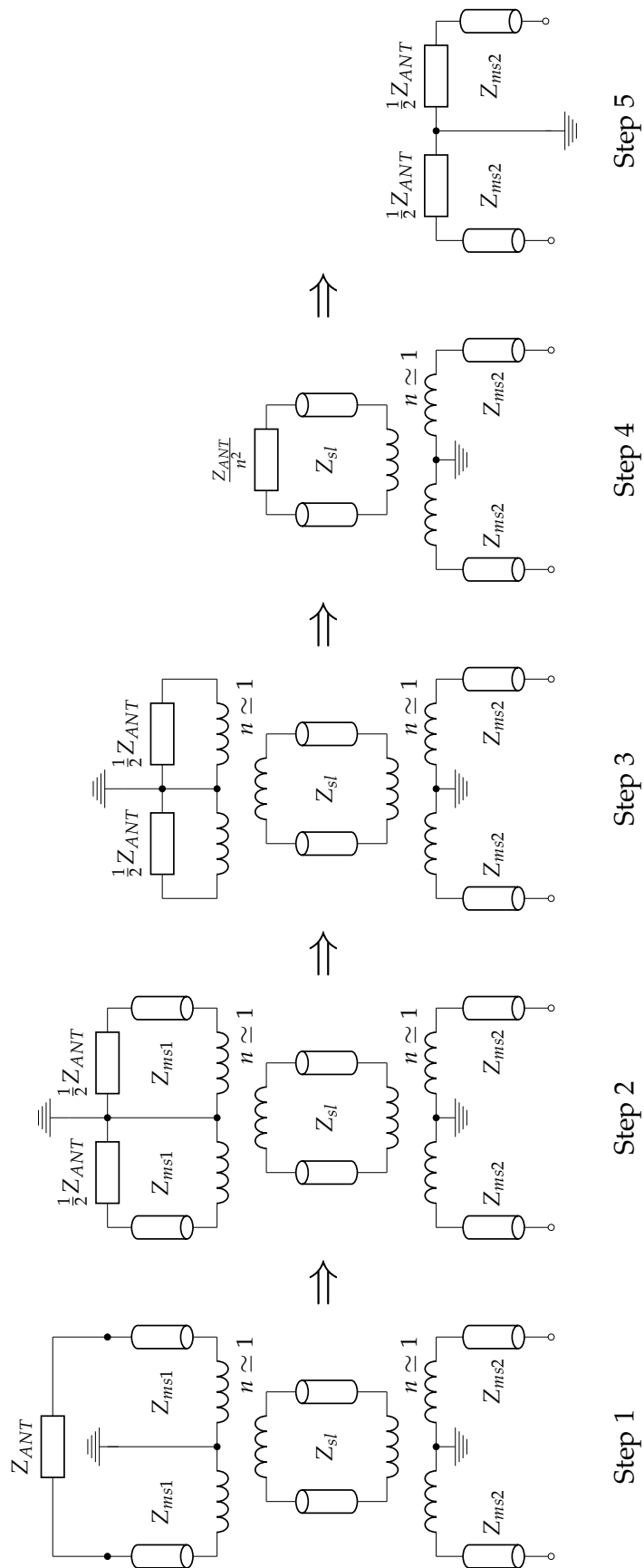


Figure 5.9: Equivalent Circuit Transformation Steps for Differential-Mode Impedance Matching

for the transmission lines in each section of the feed network to ensure maximum power transfer. For this figure, the following definitions apply:

- $Z_{ANT}$  is the differential impedance of the antenna element,
- $Z_{ms1}$  is the characteristic impedance of the primary microstrip line,
- $Z_{sl}$  is the characteristic impedance of the slotline,
- $Z_{ms2}$  is the characteristic impedance of the secondary microstrip line, and
- $n$  is the transformation coefficient of the transformer. In most cases it is reasonable to assume that  $n = 1$ ; however, techniques exist that can be used to calculate  $n$  [21,73].

Step 1 shows the equivalent circuit given in Figure 5.8 with the differential active impedance of an element in the antenna array added. In Step 2, the differential antenna impedance is divided up into two single-ended (SE) halves ( $Z_{ms1} = \frac{1}{2}Z_{ANT}$ ). Step 3 refers those SE impedances to directly before the first microstrip-slotline transition. In Step 4, the impedance is referred to the secondary winding of the transformer. Under differential-mode operation, the currents in both the primary windings will be flowing in the same direction. As a result, when the two SE impedances of the primary winding are referred to the secondary winding, the sum of the two SE impedances divided by  $n^2$  will be seen at the terminals of the secondary winding ( $Z_{sl} = \frac{Z_{ANT}}{n^2}$ ). Step 5 refers the impedance seen by the slot to the secondary microstrip pair. Note that the microstrip side of the microstrip-slotline transition acts as the primary winding. When the impedance is therefore referred from the secondary to the primary winding, the  $n^2$  term will cancel. It follows that the SE impedances seen by the secondary microstrip is then given by  $Z_{ms2} = \frac{1}{2}Z_{ANT}$ .

Following the steps set out above, the resultant characteristic impedances can be summarized as follows:

$$Z_{ms1} = \frac{1}{2}Z_{ANT}, \quad (5.3.1)$$

$$Z_{sl} = \frac{1}{n^2}Z_{ANT}, \quad (5.3.2)$$

$$Z_{ms2} = \frac{1}{2}Z_{ANT}. \quad (5.3.3)$$

The PCB was etched on Rogers 4003C [74] ( $\epsilon_r = 3.38$ ) and using equations 5.3.1-5.3.3, the dimensions, as defined in Figure 5.10 were determined. These dimensions are given in Table 5.3.

The design was simulated using the commercial MoM Simulator FEKO [54] before it was manufactured. A photograph of the manufactured prototype can be seen in Figure 5.11.

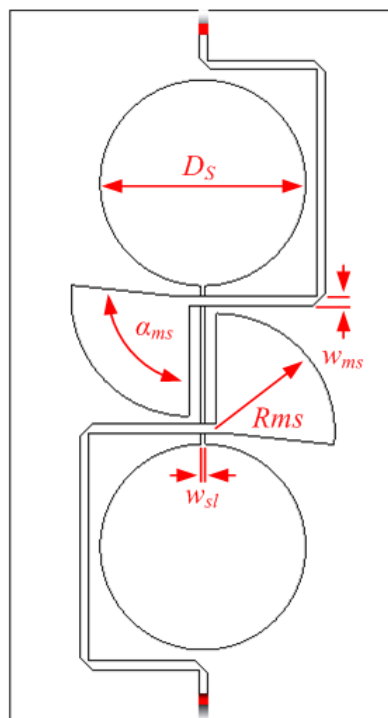


Figure 5.10: Dimensions

Table 5.3: Feed Network Specifications

Dimension	Description	Value
$D_s$	Diameter of Slotline Stub	18.7mm
$R_{ms}$	Radius of Microstrip Stub	10.8mm
$w_{ms}$	Width of Microstrip lines	0.8mm
$w_{sl}$	Width of Slotline	0.4mm
$\alpha_{ms}$	Flare angle of Microstrip stub	$96^\circ$
$\epsilon_r$	Dielectric Constant of Substrate	3.38
$h$	Height of Substrate (per layer)	0.8mm

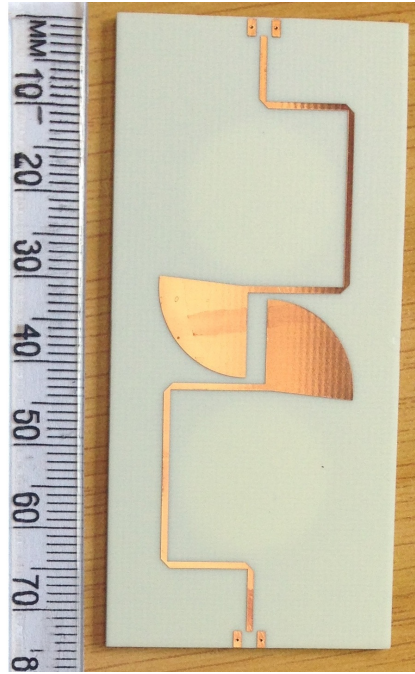


Figure 5.11: Photograph of the manufactured prototype

Details of how the various differential and common-mode properties of the network were determined are given in the next section.

## 5.4 Measurement Procedure

Differential and common-mode properties of balanced structures can be measured by using two single-ended ports to represent each differential (symmetrical) port [58,59].

Fan et al. did a concise characterization of combined differential-mode and common-mode (Mixed-Mode) S-parameters in order to assist in the evaluation of differential structures in [75]. Therein, a method was also devised with which single-ended S-parameters, which are more readily measurable, can be converted into mixed-mode S-parameters. This method is summarized below.

For the 4-port device in Figure 5.12, the standard, single-ended S-parameter matrix is given by

$$S_{std} = \begin{bmatrix} S_{11} & S_{12} & S_{13} & S_{14} \\ S_{21} & S_{22} & S_{23} & S_{24} \\ S_{31} & S_{32} & S_{33} & S_{34} \\ S_{41} & S_{42} & S_{43} & S_{44} \end{bmatrix}. \quad (5.4.1)$$

If the same 4-port single-ended device were to be seen as a 2-port differential device, with port 1 and 2 forming differential port 1, and port 3 and



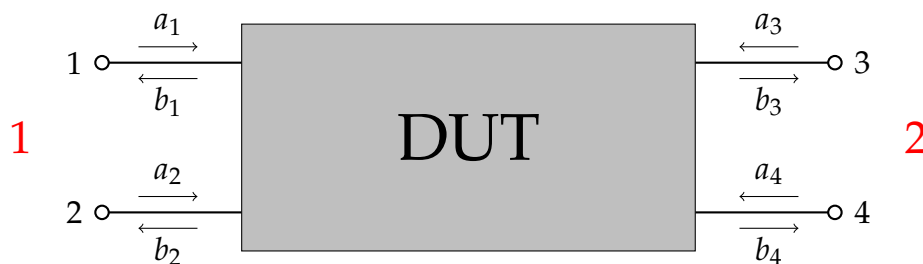


Figure 5.12: Single-Ended 4-port DUT

4 forming differential port 2, the mixed-mode S-parameter matrix would be given by

$$S_{mm} = \begin{bmatrix} S_{d1d1} & S_{d1d2} & S_{d1c1} & S_{d1c2} \\ S_{d2d1} & S_{d2d2} & S_{d2c1} & S_{d2c2} \\ S_{c1d1} & S_{c1d2} & S_{c1c1} & S_{c1c2} \\ S_{c2d1} & S_{c2d2} & S_{c2c1} & S_{c2c2} \end{bmatrix}. \quad (5.4.2)$$

The single-ended S-parameter matrix can then be transformed using a transformation matrix,  $M$ , given by

$$M = \frac{1}{\sqrt{2}} \begin{bmatrix} 1 & -1 & 0 & 0 \\ 0 & 0 & 1 & -1 \\ 1 & 1 & 0 & 0 \\ 0 & 0 & 1 & 1 \end{bmatrix}, \quad (5.4.3)$$

as

$$S_{mm} = MS_{std}M^{-1}. \quad (5.4.4)$$

Using the mixed-mode S-parameter matrix of the network given in Equation 5.4.2, the differential and common-mode properties of note can be determined as follows:

$S_{d2d1}$  is the differential-mode transmission,

$S_{c2c1}$  is the common-mode transmission of the network.

The common-mode rejection ratio (CMRR) will then be given by

$$\text{CMRR} = 20 \log \left( \frac{|S_{d2d1}|}{|S_{c2c1}|} \right). \quad (5.4.5)$$

In the next section, results from simulations as well as measurements will be presented.

## 5.5 Results

Figure 5.13 shows the results of simulations and measurements for the differential-mode transmission ( $S_{d2d1}$ ). The results match well across the entire

measured band, with a slightly increased deviation at higher frequencies. The dip at 1000 MHz present in the simulation results can be attributed to a resonance created in the structure due to the assumption that a lossless conductor is used. In practice, the resistance in the copper dampens the resonance which is why the dip is absent in the measured results.

In Figures 5.14 and 5.15 the common-mode transmission ( $S_{c1c2}$ ) and CMRR are depicted respectively. There is very little deviation between the measured data and the simulation.

All the measurements and simulation results meet or exceed the design specifications set out in Table 5.2.

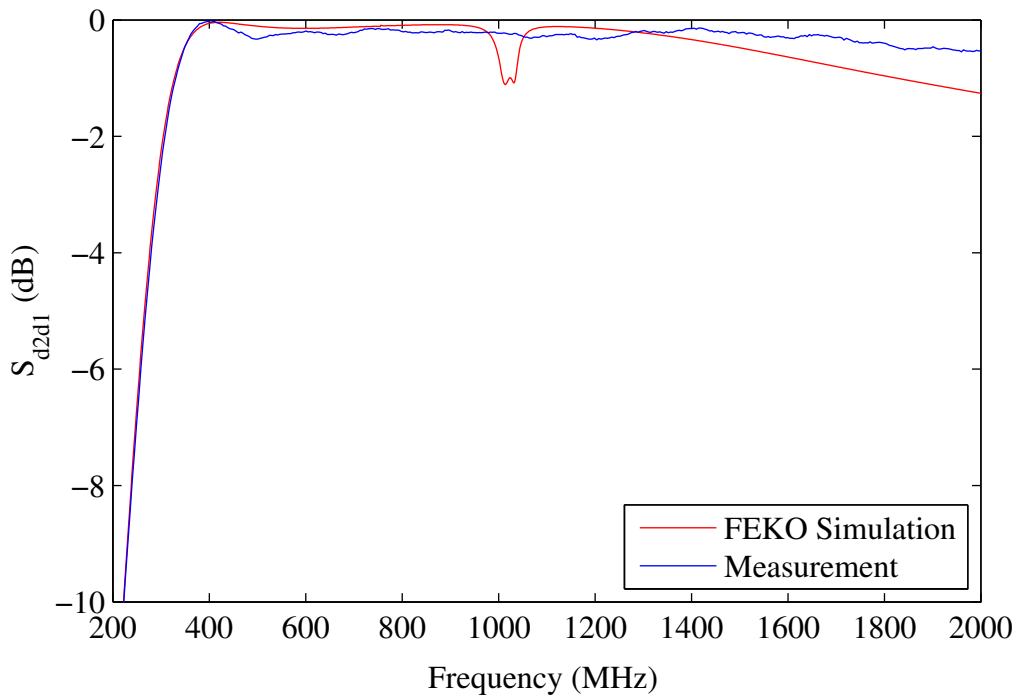


Figure 5.13: Differential-Mode Transmission

## 5.6 Conclusion

A design that will reject common-mode resonances in arrays of connected antennas over a wide bandwidth was presented. The PCB based design makes use of symmetrical wideband microstrip-slotline transitions in order to facilitate the cancellation of common-mode signals, while differential-mode signals propagate through the device with minimal loss.

Results from simulations and measurements have indicated that this design offers wide bandwidth and good common-mode rejection that exceed design specifications.

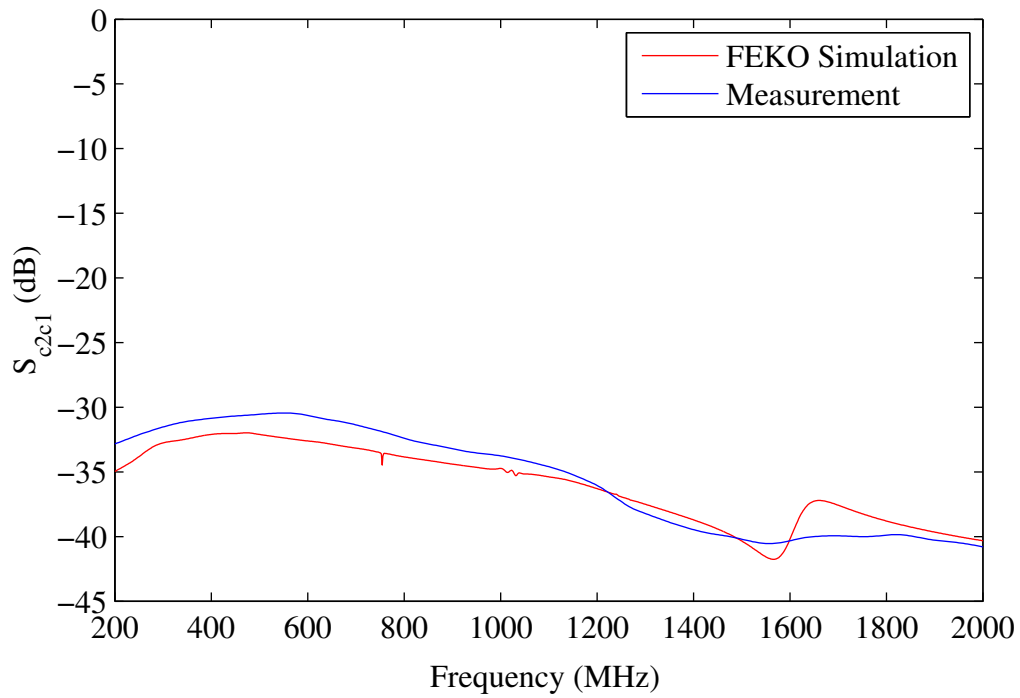


Figure 5.14: Common-Mode Transmission

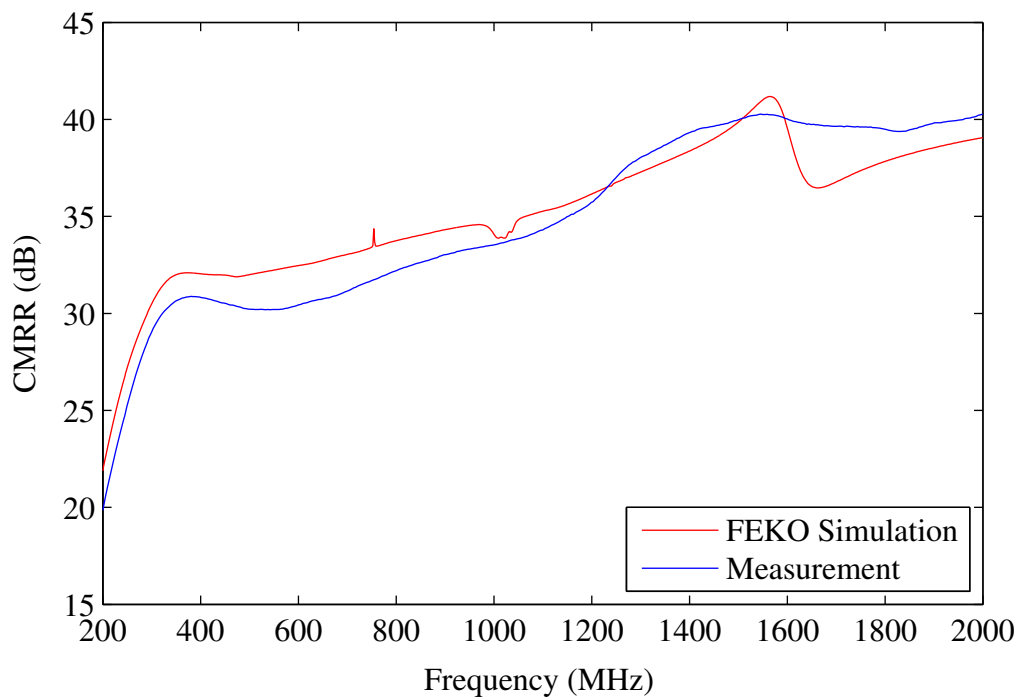


Figure 5.15: Common-Mode Rejection Ratio

# Chapter 6

## Results

### 6.1 Introduction

In this chapter, the results of two DDA prototypes are discussed. The first prototype is that of a small  $4 \times 4 \times 1$  DDA (i.e.  $4 \times 4$  array that is single-polarized), while the second prototype is a  $10 \times 10 \times 2$  array (i.e. a  $10 \times 10$  array that is dual-polarized).

The procedure that was used to measure the mixed-mode S-parameters of the two prototypes is summarized in Section 6.2. Section 6.3 presents the results of the  $4 \times 4 \times 1$  prototype. The results of the  $10 \times 10 \times 2$  prototype are discussed in Section 6.4, and Section 6.5 concludes.

### 6.2 Description of the Multi-Port Mixed-Mode S-parameter Measurement Procedure

This section contains a description of the procedure used to measure the S-parameters of both the  $4 \times 4 \times 1$  as well as the  $10 \times 10 \times 2$ . This is a summary of the procedure described in [59].

As explained in Chapter 5, it is not trivial to measure the mixed-mode properties of a differential system when the measurement equipment does not offer this functionality. It was therefore necessary to first measure the single-ended S-parameters and then convert them to mixed-mode S-parameters in order to analyse the differential- and common-mode behaviour of the system.

Measuring the differentially-fed antenna array offered the same difficulties in that the mixed-mode S-parameters could not be directly measured with the available equipment. In addition to that, the DUT now has more ports than the VNA with which the measurements are being made.

The single-ended S-parameter matrix is “filled” by conducting multiple measurements, ensuring that each pair of single-ended ports have been

used in at least one measurement. The ports that are not being measured are terminated in matched loads. It is possible to use symmetry to reduce the number of measurements that are required to describe the system; however, given the involved nature of the measurement process there is a high probability that measurement errors can occur. As a result it was decided to rather use the symmetry as a method of redundant error checking.

Once the whole S-parameter matrix has been filled, the measurement plane is shifted in order to exclude the SMA connectors from the measurement. The S-parameter matrix is then renormalized from a characteristic impedance of  $50 \Omega$ , which is characteristic impedance of the measurement equipment, to  $75 \Omega$ . This corresponds to a differential characteristic impedance of  $150 \Omega$ , which is the differential characteristic impedance of the DUT.

After the renormalization, the single-ended S-parameter matrix can be converted to the mixed-mode S-parameter matrix.

For a system with differential ports  $m$  and  $n$ , each consisting of two single-ended ports  $p$  and  $q$ , the mixed-mode S-parameter matrix of the array is given by:

$$\mathbf{S}_{\text{MM}} = \begin{bmatrix} \mathbf{S}_{\text{diff diff}} & \mathbf{S}_{\text{diff comm}} \\ \mathbf{S}_{\text{comm diff}} & \mathbf{S}_{\text{comm comm}} \end{bmatrix} \quad (6.2.1)$$

where the values of the elements in each submatrix are calculated as follows:

$$S_{\text{diff diff}, mn} = \frac{S_{pp,mn} - S_{pq,mn} - S_{qp,mn} + S_{qq,mn}}{2} \quad (6.2.2)$$

$$S_{\text{diff comm}, mn} = \frac{S_{pp,mn} + S_{pq,mn} - S_{qp,mn} - S_{qq,mn}}{2} \quad (6.2.3)$$

$$S_{\text{comm diff}, mn} = \frac{S_{pp,mn} - S_{pq,mn} + S_{qp,mn} - S_{qq,mn}}{2} \quad (6.2.4)$$

$$S_{\text{comm comm}, mn} = \frac{S_{pp,mn} + S_{pq,mn} + S_{qp,mn} + S_{qq,mn}}{2}. \quad (6.2.5)$$

The sub-matrices in equation 6.2 can now also be used to calculate the active reflection coefficient of element  $m$  for a given scan direction  $(\theta_0, \varphi_0)$

and excitation mode:

$$\Gamma_{dd,m}(\theta_0, \varphi_0) = \sum_{n=1}^N S_{\text{diff diff,mn}} e^{-jk(x_n \sin \theta_0 \cos \varphi_0 + y_n \sin \theta_0 \sin \varphi_0)} \quad (6.2.6)$$

$$\Gamma_{dc,m}(\theta_0, \varphi_0) = \sum_{n=1}^N S_{\text{diff comm,mn}} e^{-jk(x_n \sin \theta_0 \cos \varphi_0 + y_n \sin \theta_0 \sin \varphi_0)} \quad (6.2.7)$$

$$\Gamma_{cd,m}(\theta_0, \varphi_0) = \sum_{n=1}^N S_{\text{comm diff,mn}} e^{-jk(x_n \sin \theta_0 \cos \varphi_0 + y_n \sin \theta_0 \sin \varphi_0)} \quad (6.2.8)$$

$$\Gamma_{cc,m}(\theta_0, \varphi_0) = \sum_{n=1}^N S_{\text{comm comm,mn}} e^{-jk(x_n \sin \theta_0 \cos \varphi_0 + y_n \sin \theta_0 \sin \varphi_0)} \quad (6.2.9)$$

Note that to aid in the readability of the active reflection coefficient terms in Equations 6.2.6 - 6.2.9, the terms “diff” and “comm” were further abbreviated to “d” and “c” respectively to represent the different excitation modes.

## 6.3 The $4 \times 4 \times 1$ Prototype

Even though a  $4 \times 4 \times 1$  prototype DDA is not expected to be a good representation of the  $\infty \times \infty \times 1$  array simulations, it was still considered an important step in the design process, for various reasons which are briefly discussed below.

Firstly, it was necessary to confirm the reliability of the simulations. This included being able to test the validity of certain assumptions.

Secondly, building a scale model also serves as an opportunity to gain insight into some of the manufacturing and assembly difficulties associated with the design. These practical insights are valuable when progressing on to larger prototypes, and indeed a full aperture array.

Manufacturing and measurement of this prototype was done at ASTRON in the Netherlands.

### 6.3.1 Description of the Prototype

Photographs of the  $4 \times 4 \times 1$  prototype from various angles are given in Figure 6.1. From the top-view photograph on the left, it can be seen that the elements were connected in parallel as explained in Section 4.2. From the two side-view photographs on the right, the connection of the common-mode suppressing feed board from Chapter 5 can also be seen.

In order to aid electrical connection between the feed boards and the array elements, slots were milled into the PCB on which the array elements were printed. The feed-boards were then positioned to protrude slightly through these slots, and the feed lines of the array element pairs were soldered directly to that of the feed-boards.



Figure 6.1: Array Assembly

From the bottom-right photograph of Figure 6.1, it can be seen that array is fed via SMA connectors through the ground plane.

The array elements are printed on a 0.8 mm thick FR4 substrate while the feed boards use Rogers material as explained in Chapter 5. The ground plane is made of aluminium, while plastic standoffs provide additional mechanical support between the PCB and the ground plane.

### 6.3.2 Results

The S-parameter matrix of the array was measured using the measurement technique described in Section 6.2. Figure 6.2 shows a photograph of the measurement setup.

The measured and simulated  $\Gamma_{dd}$  at broadside for element pair #4, which is a central element pair, are given in Figure 6.3. It should be noted that for the simulation, an infinite ground plane and substrate was assumed. Figure 6.4 show the same results, but for element pair #1, which is a corner element.

It can be seen that there is reasonably good agreement between the measurement results and simulations for the central element, but not the corner element. The larger discrepancy between the measured and simulated results indicated that the design is sensitive to edge effects, especially that of a finite ground plane. This result is expected since the inherent mechanism of operation for the array is reliant upon the relationship between the inductance of the ground plane in the vicinity of the overlapping dipole elements and the capacitance between the tips of the neighbouring elements. At the edges of the ground plane, this relationship is disturbed, resulting in a deviation from the results measured at a central element.



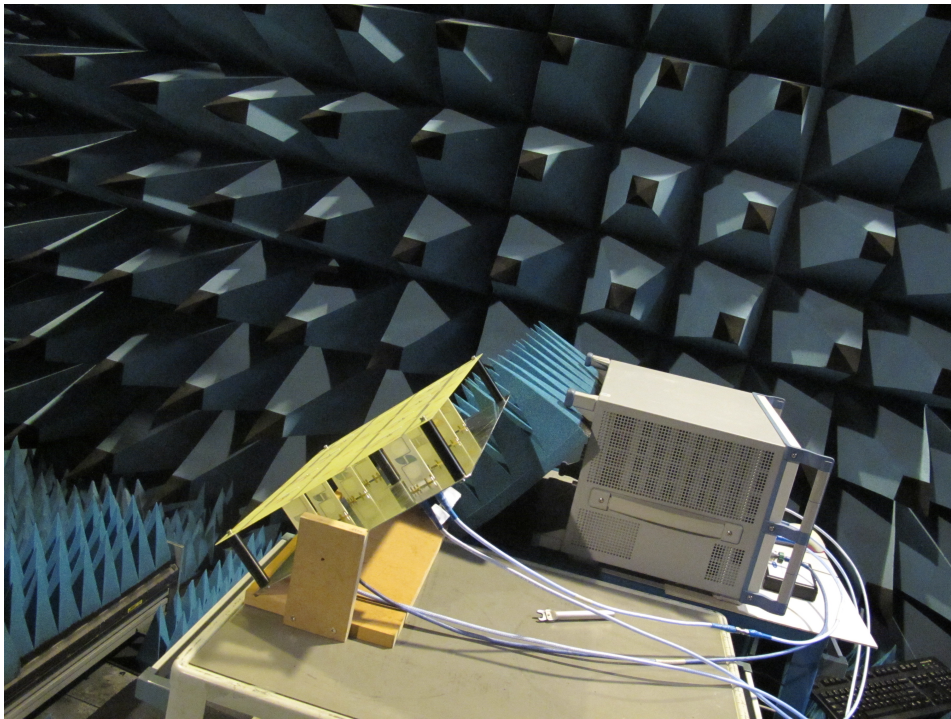
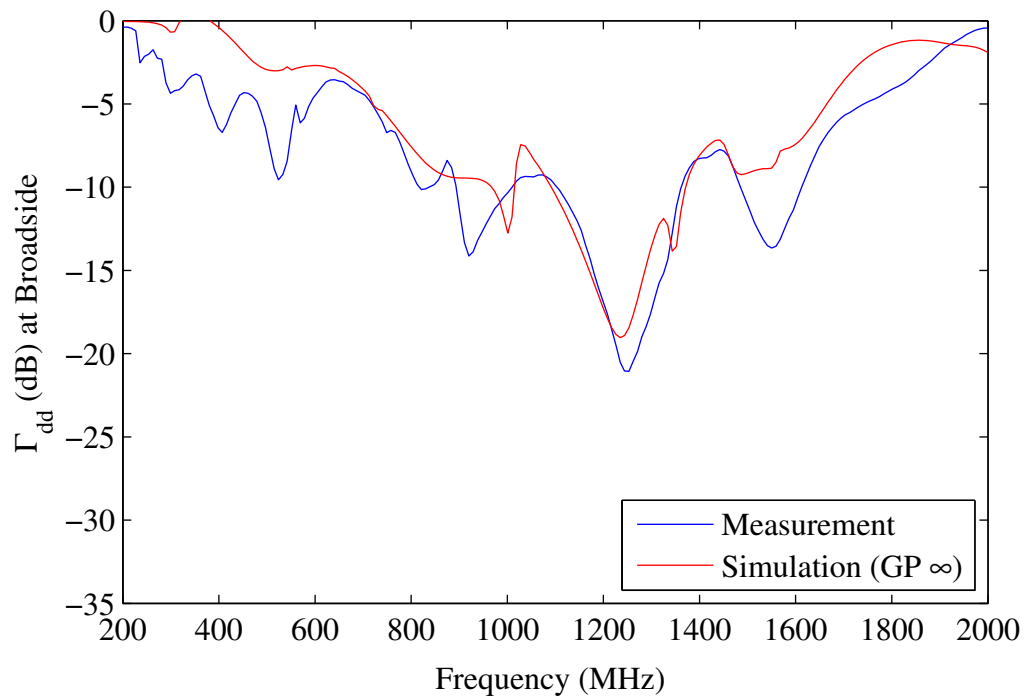


Figure 6.2: Array Assembly

Figure 6.3: Measured and Simulated  $\Gamma_{dd}$  at broadside for a central element in the array



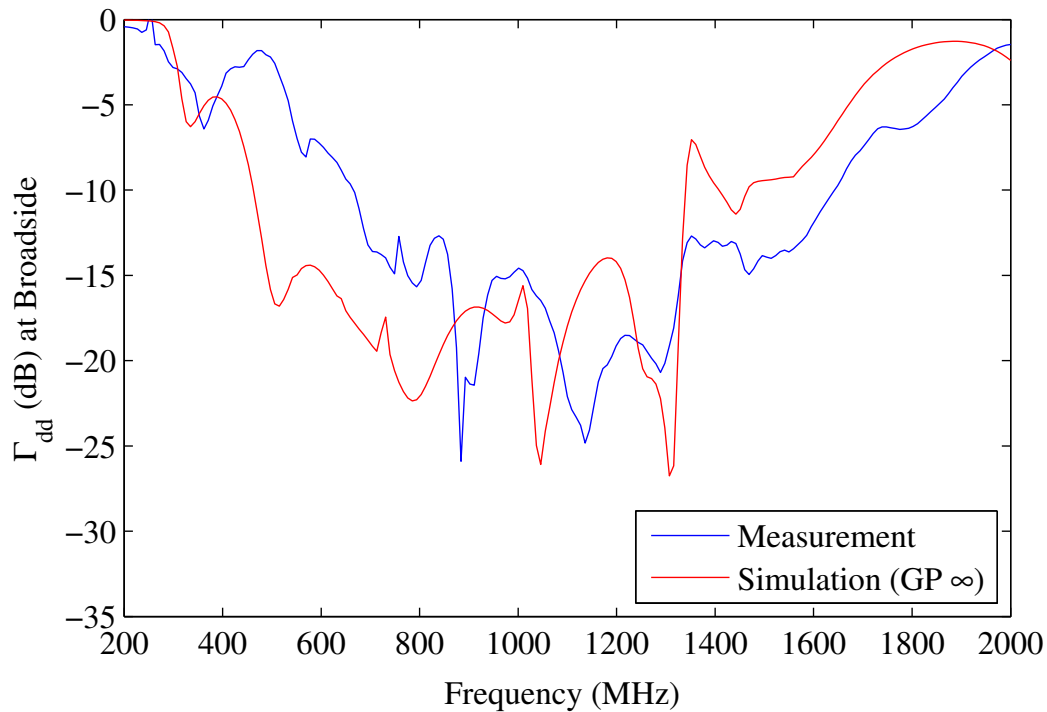


Figure 6.4:  $\Gamma_{dd}$  at broadside for a corner element in the array

It should also be noted that one of the elements of the central pair is still located at the edge of the array, so some edge effects will still be observed; however, the agreement between the measurements and the simulated results for this element pair is still considered to be sufficient to verify the simulation results.

A  $\Gamma < -10dB$  bandwidth in the order of  $\approx 200$  MHz was achieved. This is far from the bandwidth achieved by the infinite array simulation, however, as was explained above, the small prototype was intended to prove the accuracy of the simulations and the validity of certain simulation assumptions as well as to gain insight into the manufacturing process of the array.

The common-mode performance (measured as well as simulated results) for the same two elements pairs are depicted in Figure 6.5. The agreement between the measured and simulated results for both element pairs are very good, and the common-mode resonances seem to be thoroughly suppressed throughout the measured band. These results offer further confirmation to the effectiveness of the common-mode filter presented in Chapter 5.

Since the  $4 \times 4 \times 1$  array is such a small prototype, and there is quite a dramatic difference between  $\Gamma_{dd}$  for a corner and a central element, it was suggested that an embedded element pattern measurement for this array would not be a representative result and hence was not measured.

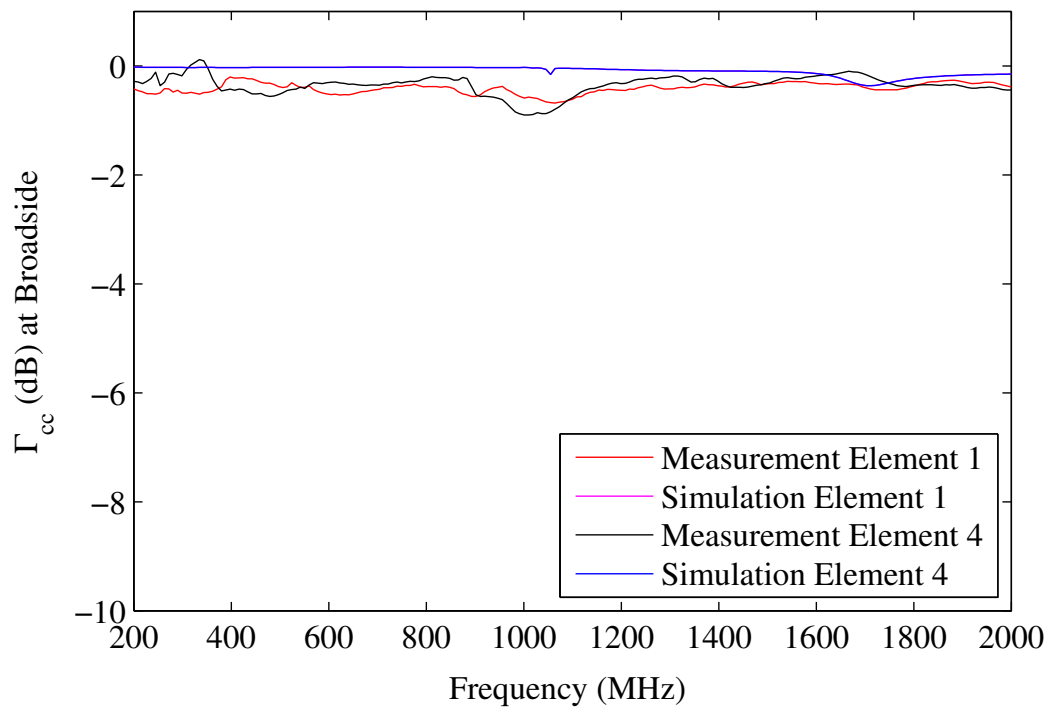


Figure 6.5:  $\Gamma_{cc}$  at broadside for a corner- and central element in the array

## 6.4 The $10 \times 10 \times 2$ Prototype

The  $10 \times 10 \times 2$  prototype was intended to serve as a test-bed with which more representative results could be obtained. Being close to  $1 \text{ m}^2$  in size, it is also in line with the tile size selected for other MFAA candidate topologies and is also the likely tile size for the final MFAA product that is intended for mass-production and deployment. The insight gained into various mechanical as well as manufacturability issues are therefore valuable for future studies on preparing the technology for mass-production.

### 6.4.1 Description of the Prototype

The two polarizations of the  $10 \times 10 \times 2$  array were printed on either side of a 0.8 mm thick FR4 substrate. Given how involved the process of measuring S-parameters for such a large array is, and adding how pronounced the edge effects of the array are, it was decided to only feed the central  $4 \times 4 \times 2$  elements, and to terminate the rest of the elements using small SMT resistors matched to the differential characteristic impedance ( $150 \ \Omega$ ) soldered directly to the feed point.

The “active” elements were fed via the common-mode filter feed-boards using the same construction method as with the small prototype. The same materials were used as with the small prototype, but as was explained in

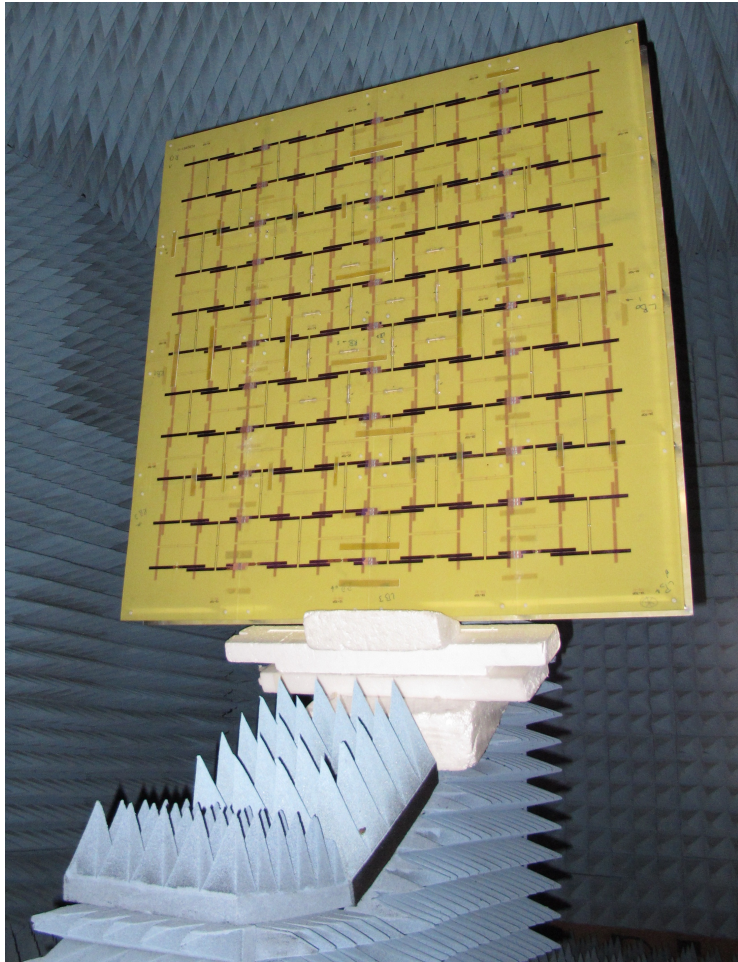


Figure 6.6: Photograph of the  $10 \times 10 \times 2$  DDA prototype mounted in the anechoic chamber.

Chapter 4, the array elements corresponding to each polarization were printed on either side of the PCB.

Limitations in the dimensions of the raw PCB materials that were available necessitated the array structure to be broken up into multiple smaller PCB's - 16 in total. Since the geometry of the array is by design a continuous structure, this meant that some array elements as well as feed lines had to be broken in order to achieve this. As a result, electrical connection had to be re-established at the edges of the PCB's on both layers during assembly using a combination of copper tape and solder for the array elements, and copper wire strands and solder for the thin feed lines.

The fact that multiple PCB's with weakened electrical connection points between them had to be accommodated for, required a more careful approach to the mechanical design. To aid with the positioning of the different PCB's and to improve the structural integrity of the thin, broken-up layer, small, plastic plates were specifically designed and laser-cut in order to con-



Figure 6.7: Photograph of the feed board being used to feed the  $10 \times 10 \times 2$  DDA prototype

nect the corners of the different PCB's together at the appropriate position. In addition to that, plastic standoffs were used to provide support between the PCB layer and the aluminium ground plane. A photograph detailing the mechanical support is shown in Figure 6.8.

The PCB's, laser-cut plates, standoffs and feedboards were all manufactured in-house at ASTRON, and the final assembly and measurements were done at Stellenbosch University.

Figure 6.6 is a photograph of the assembled array mounted in the anechoic chamber. Figure 6.7 offers a view-point to the space between the ground plane and the PCB layer. A partial view of one of the laser-cut support plates can be seen on the left hand side of the picture. The feedboards can also be clearly seen, as well as some of the plastic standoffs. Figure 6.9 offers view of the dual-layer continuous array structure.



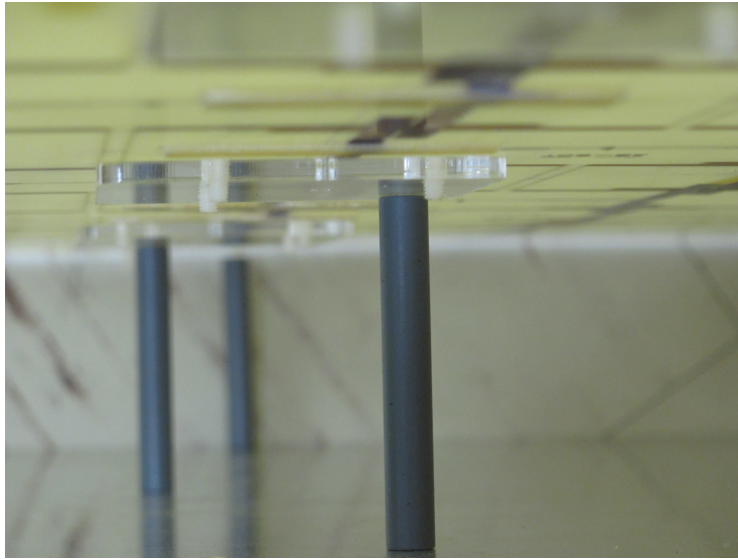


Figure 6.8: Photograph detailing the plastic laser-cut plates and standoffs that provide the mechanical support between the PCB layer and the ground plane.

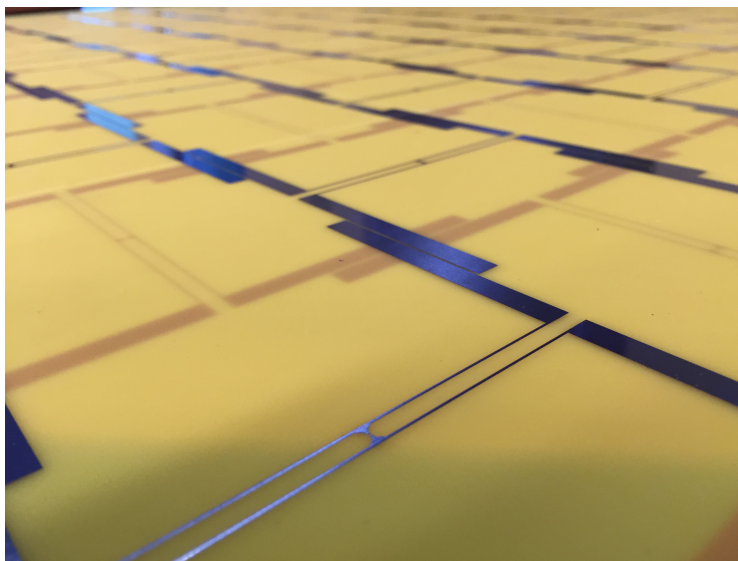


Figure 6.9: Photograph of the continuous array structure of the  $10 \times 10 \times 2$  DDA prototype

### 6.4.2 Results

The S-parameters were once again measured and converted to mixed-mode active reflection coefficient terms using the technique described in Section 6.2. The structure was also simulated in FEKO using an infinite substrate and ground-plane approximation. Due to the difficulties encountered in simulating a finite structure of this size, a coarser mesh was also used than with the infinite array approximation. This was expected to further influence the accuracy of the finite array simulation. The simulation model can be seen in Figure 6.10.

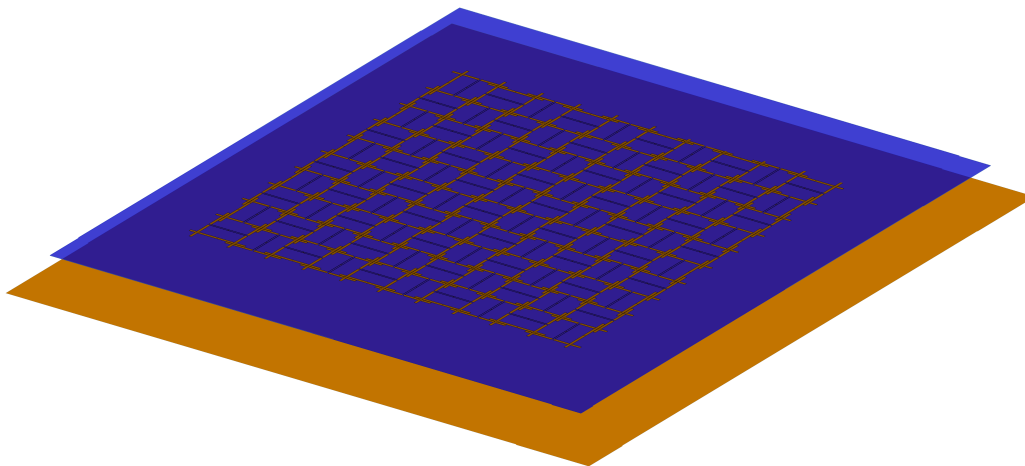


Figure 6.10: Simulation model of the  $10 \times 10 \times 2$  prototype.

The results of the differential-mode active reflection coefficient term  $\Gamma_{dd}$  for a central element for both the measurements as well as the simulations are shown in Figure 6.11. This is for broadside scan. It can be seen that despite the expected inaccuracies due to the difficulties encountered in simulating such a large, finite array, there is still some level of agreement between the simulated and measured results.

In Figure 6.12 the differential-mode active reflection coefficients for both vertically and horizontally polarized central elements at broadside are given. It can be seen that despite being printed on opposite sides of a PCB, the agreement between the results is very good. In addition to that, the bandwidth for  $\Gamma < -5$  dB is  $\approx 1.9 : 1$ , which compares well with the  $\approx 2 : 1$  bandwidth offered by the differentially fed Vivaldi design in [59]; however, as was the case with the Vivaldi design in [59] the  $\Gamma < -10$  dB bandwidth is still small and does not compare well with the results of the infinite array simulation. Since the -5 dB bandwidth of this prototype is comparable to that of the small single polarized  $4 \times 4$  prototype, it would suggest that the number of active elements is what determines the bandwidth, and not

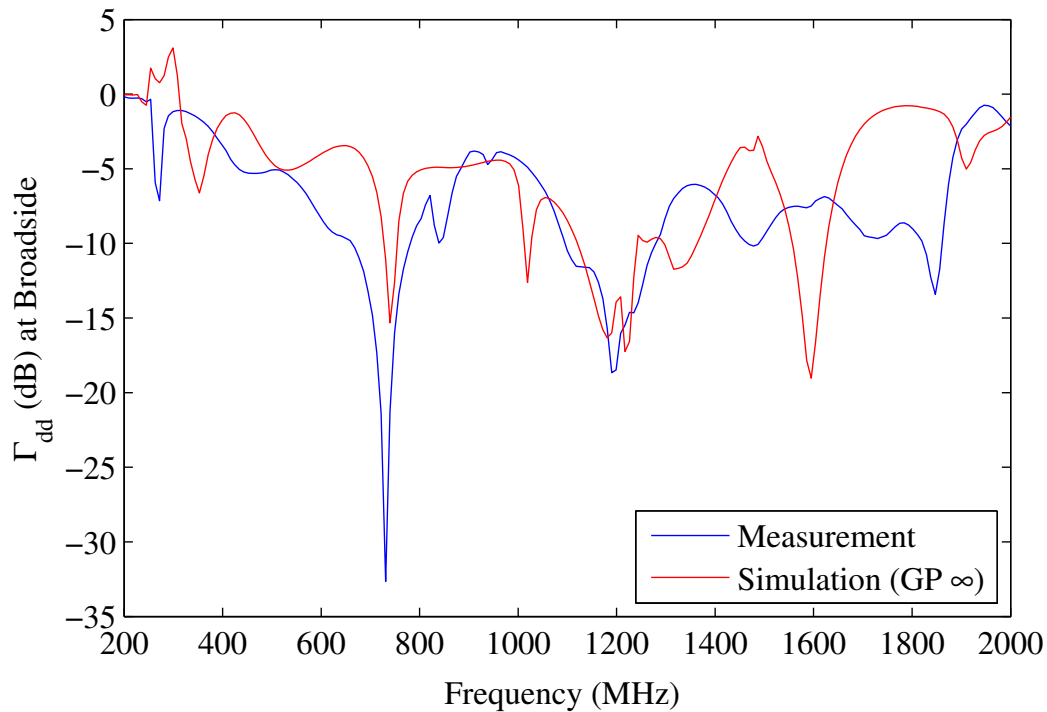


Figure 6.11: Differential-mode reflection coefficient of a central element in the  $10 \times 10 \times 2$  prototype array.

the size of the array aperture. This indicates that a larger active central section might be required to better emulate an infinite current sheet. As was detailed in Section 6.4.1, the laborious nature of the measurement process only the central  $4 \times 4 \times 2$  elements were fed at this stage.

The measured and simulated results of the common-mode active reflection coefficient for broadside scan,  $\Gamma_{cc}$  is shown in Figure 6.13. It can be seen that the common-mode resonances are very effectively suppressed by the common-mode filter. The agreement between the measured and simulated results is also good.

The differential-mode mutual coupling between two co- or cross-polarized neighbouring elements are shown in Figure 6.15. It can be seen that there is very little coupling between cross-polarized elements. The level of mutual coupling between co-polarized elements is much higher, although still less than  $-10$  dB.

The common-mode and mixed-mode mutual coupling between two co- or cross-polarized neighbouring is given in Figure 6.16 and Figure 6.17 respectively. In both cases A very low level of mutual coupling is observed for both polarizations. This again demonstrates the effectiveness of the common-mode filter.

The differential-mode antenna pattern was measured by measuring the two single-ended antenna patterns and converting it to the differential-mode

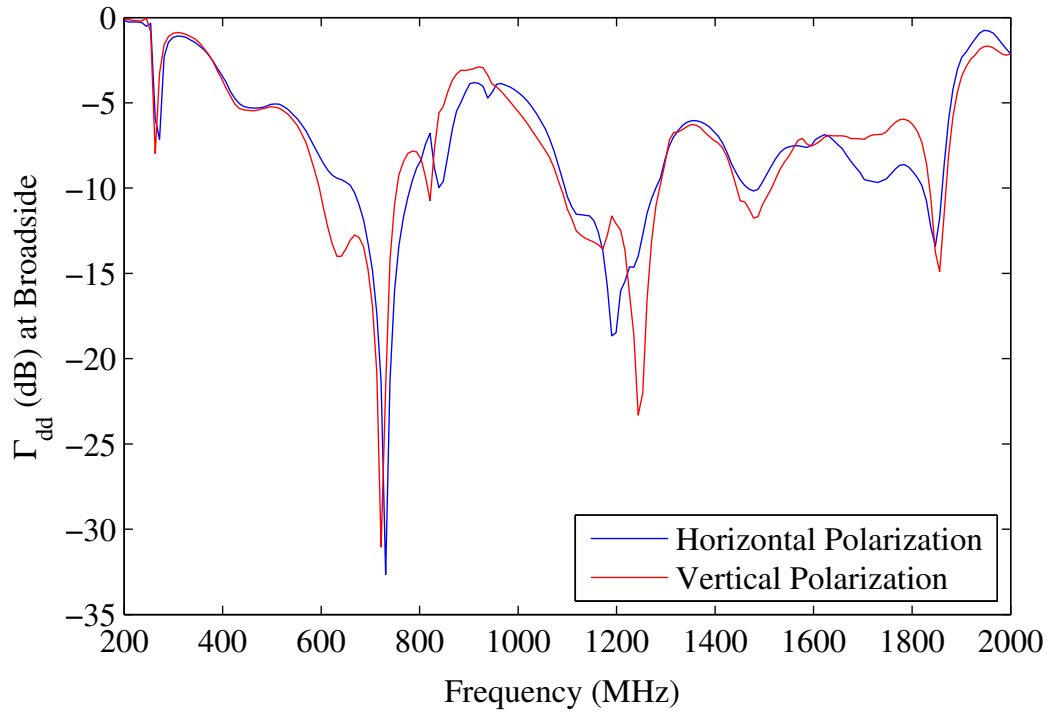


Figure 6.12: Differential-mode reflection coefficient of central elements in the  $10 \times 10 \times 2$  prototype array of both horizontal and vertical polarization.

pattern using the method described in [76]. From this method, the conversion between 2 single-ended measurements and the differential-mode gain pattern simplifies to:

$$\vec{G}_{\text{dd}} = \frac{1}{\sqrt{2}} \left[ \vec{G}_1(\theta, \phi) - \vec{G}_2(\theta, \phi) \right], \quad (6.4.1)$$

where  $\vec{G}_1(\theta, \phi)$  and  $\vec{G}_2(\theta, \phi)$  are the gain pattern vectors for the 2 single-ended ports that make up the differential port. This formulation applies to both the co- and cross-polar gain pattern.

The results of the normalised gain pattern along the  $E$ - and  $H$ -plane of the embedded element for 3 frequency points are shown in Figures 6.18 and 6.19 respectively.

Good cross-polar performance is shown along both planes, and the flatness of the beam along both axes is comparable to that of other MFAA prototype tiles [1,52].

## 6.5 Conclusion

In this chapter the results of two DDA prototypes were presented. The aim of the prototype development was to test the validity of the simulation re-



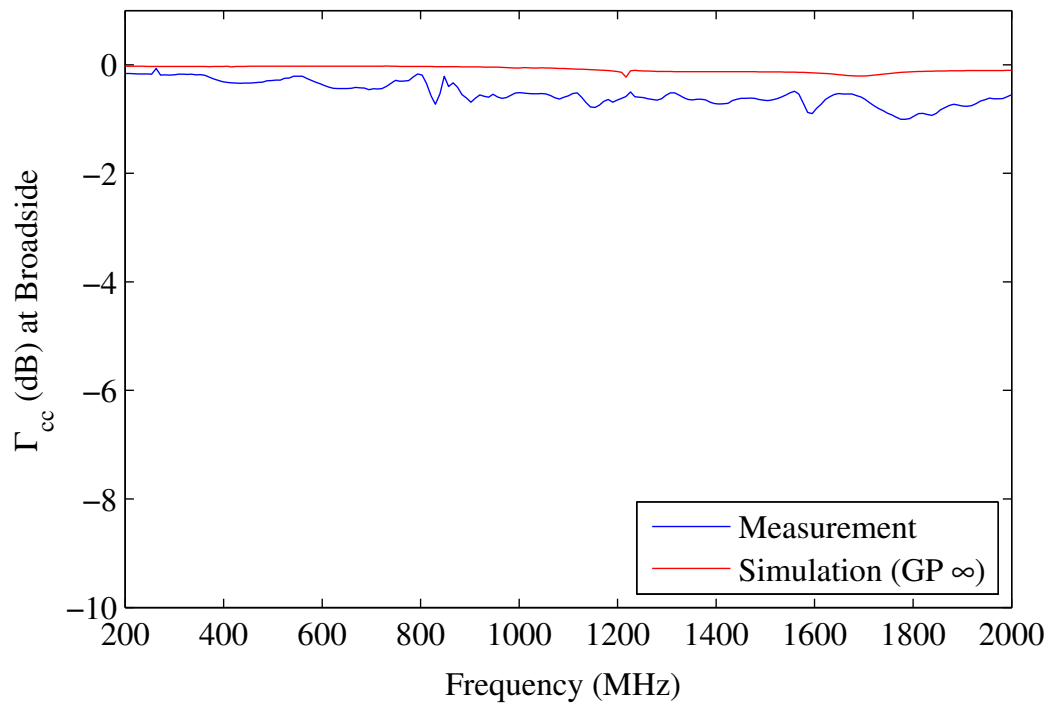


Figure 6.13: Common-mode reflection of a central element in the  $10 \times 10 \times 2$  prototype array.

sults and assumptions as well as to gain insight into any possible mechanical or manufacturing difficulties associated with the design.

The measured reflection coefficient results showed reasonable agreement with the simulations. However, it was confirmed that edge effects play a significant role in the performance of this geometry.

Embedded element gain pattern measurements of a  $10 \times 10 \times 2$  prototype showed good cross-polarization performance as well as pattern flatness that is comparable to that of other MFAA candidate topologies.

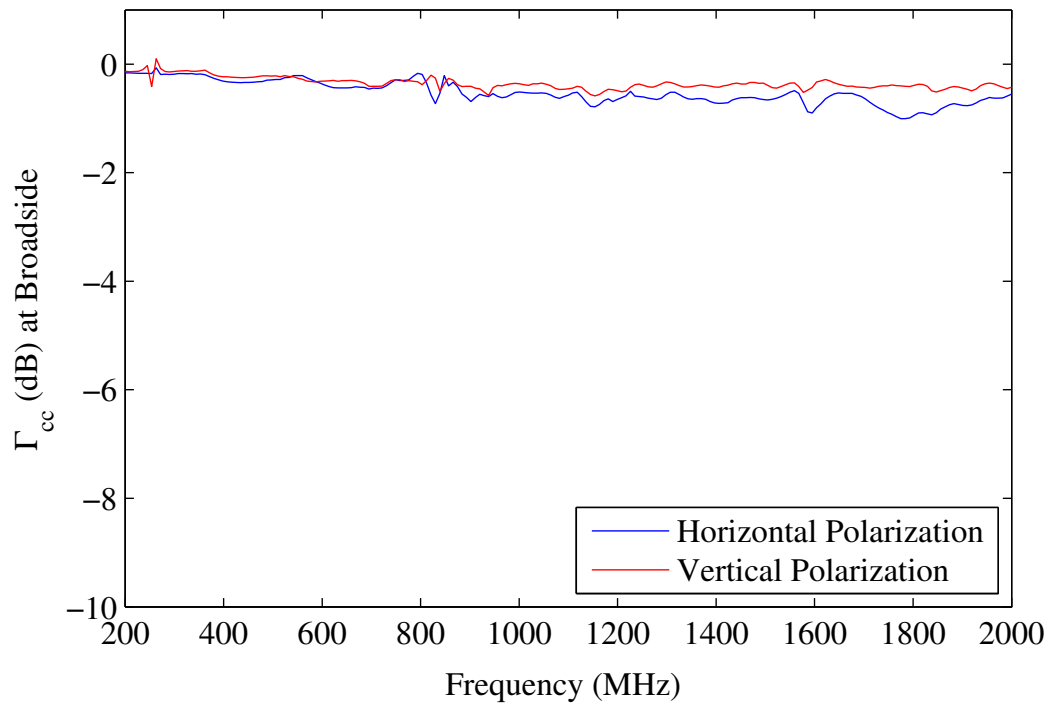


Figure 6.14: Common-mode reflection coefficient of central elements in the  $10 \times 10 \times 2$  prototype array for both horizontal and vertical polarization.

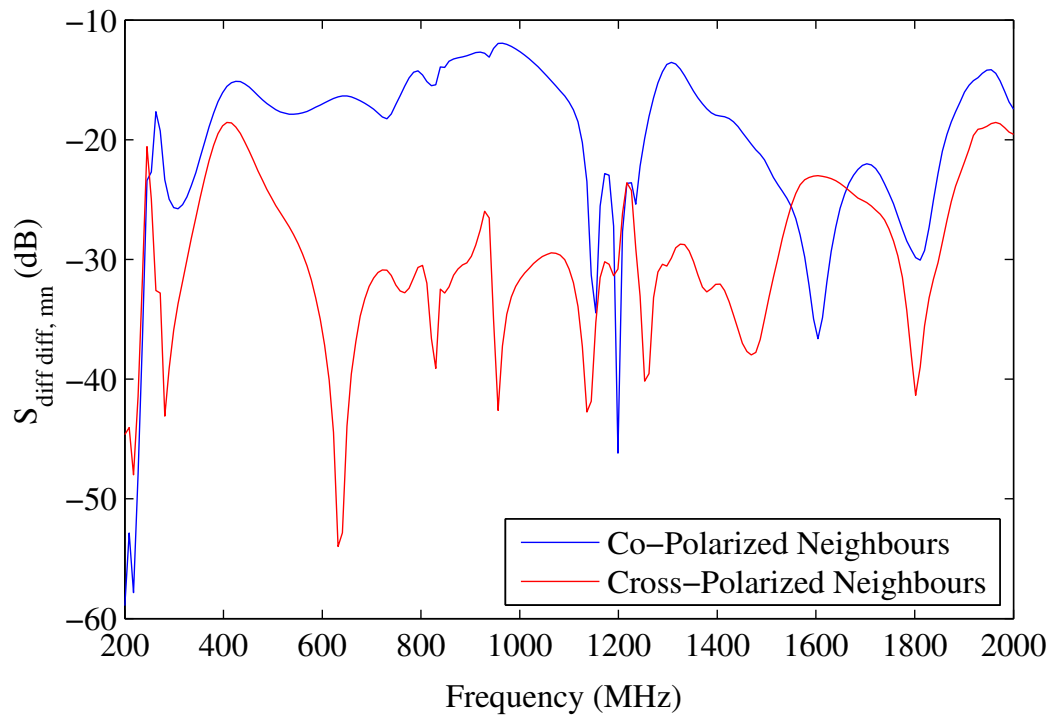


Figure 6.15: Differential-mode mutual coupling between neighbouring co- and cross-polarized elements in the  $10 \times 10 \times 2$  prototype array.

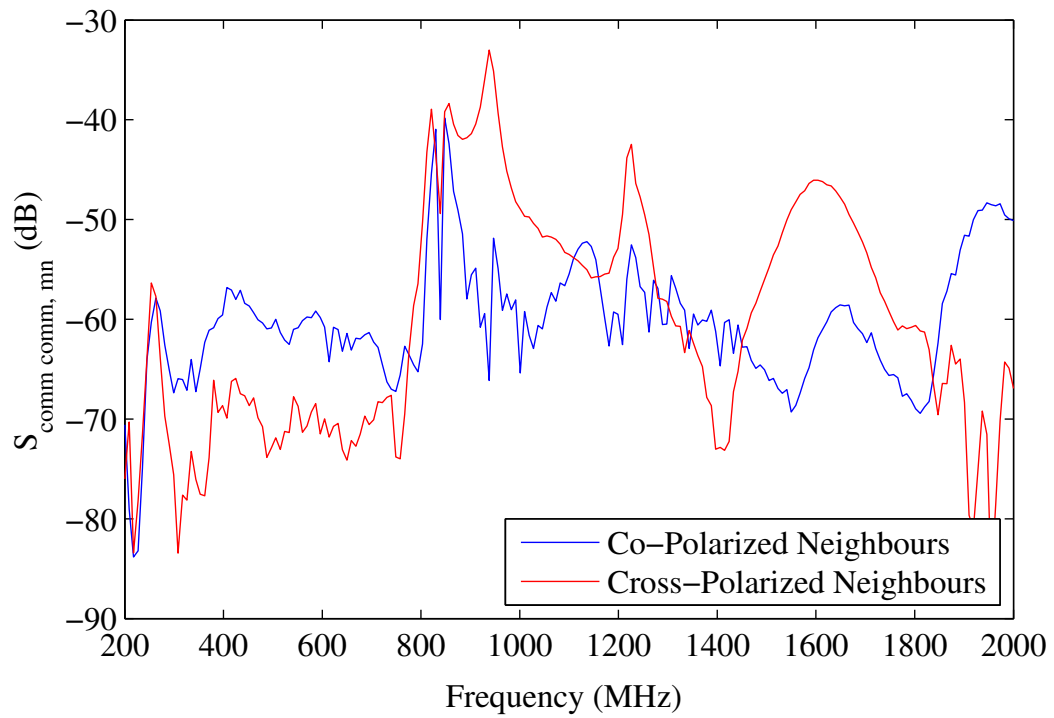


Figure 6.16: Common-mode mutual coupling between neighbouring co- and cross-polarized elements in the  $10 \times 10 \times 2$  prototype array.

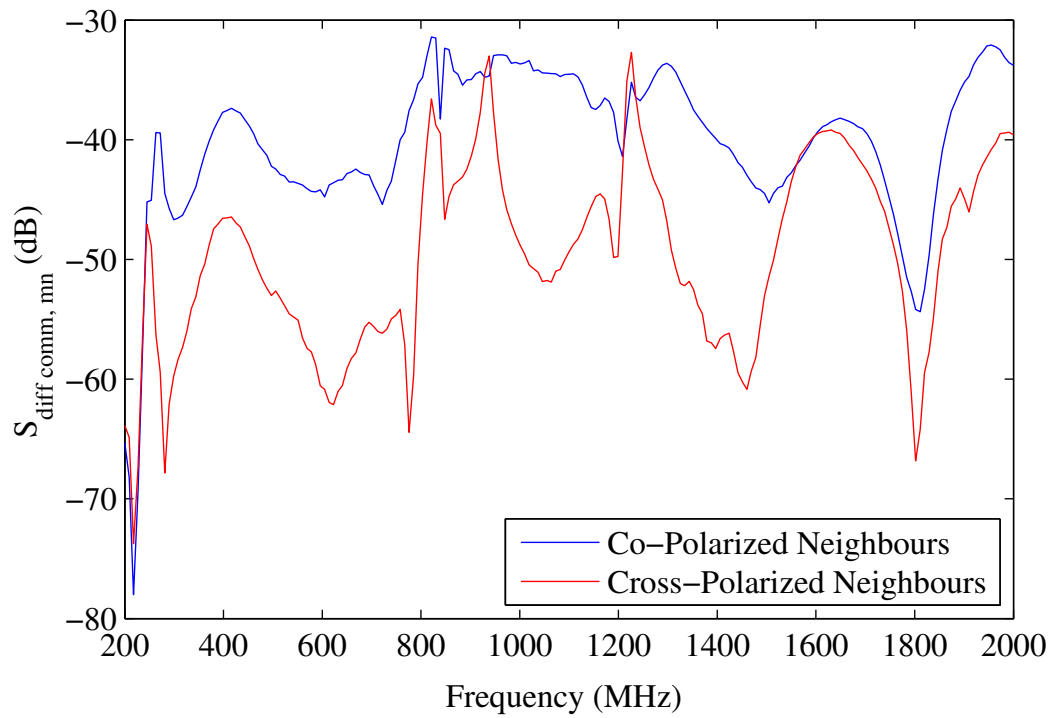


Figure 6.17: Mixed-mode mutual coupling between neighbouring co- and cross-polarized elements in the  $10 \times 10 \times 2$  prototype array.

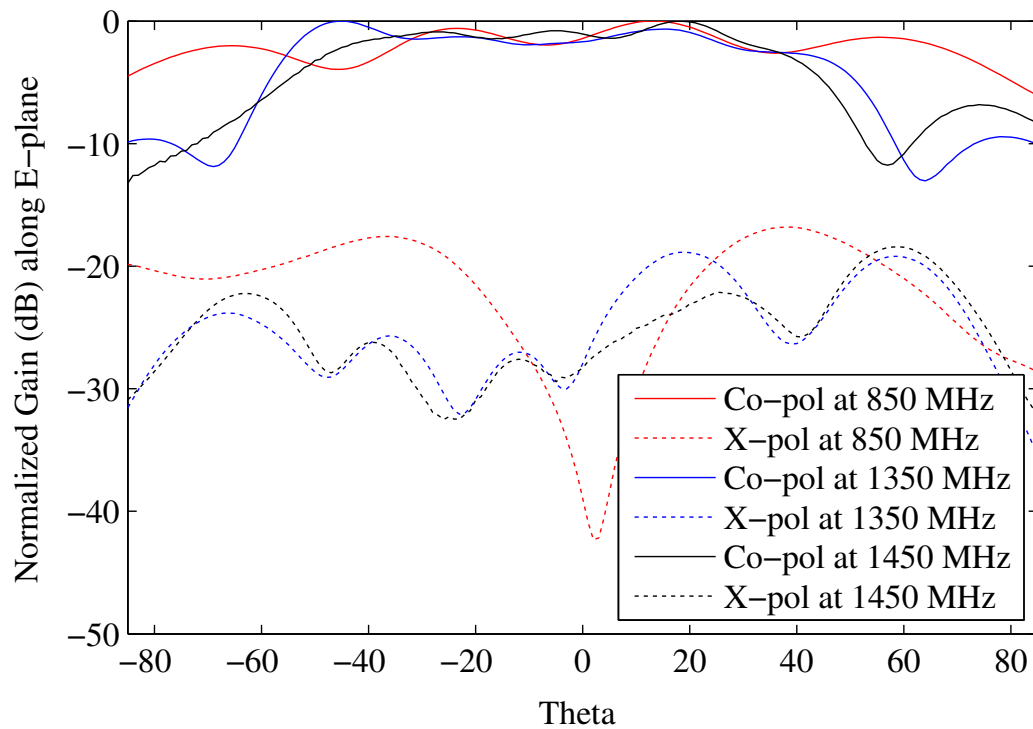


Figure 6.18: Normalised co-polar and cross-polar gain patterns along the  $E$ -plane for an embedded element.

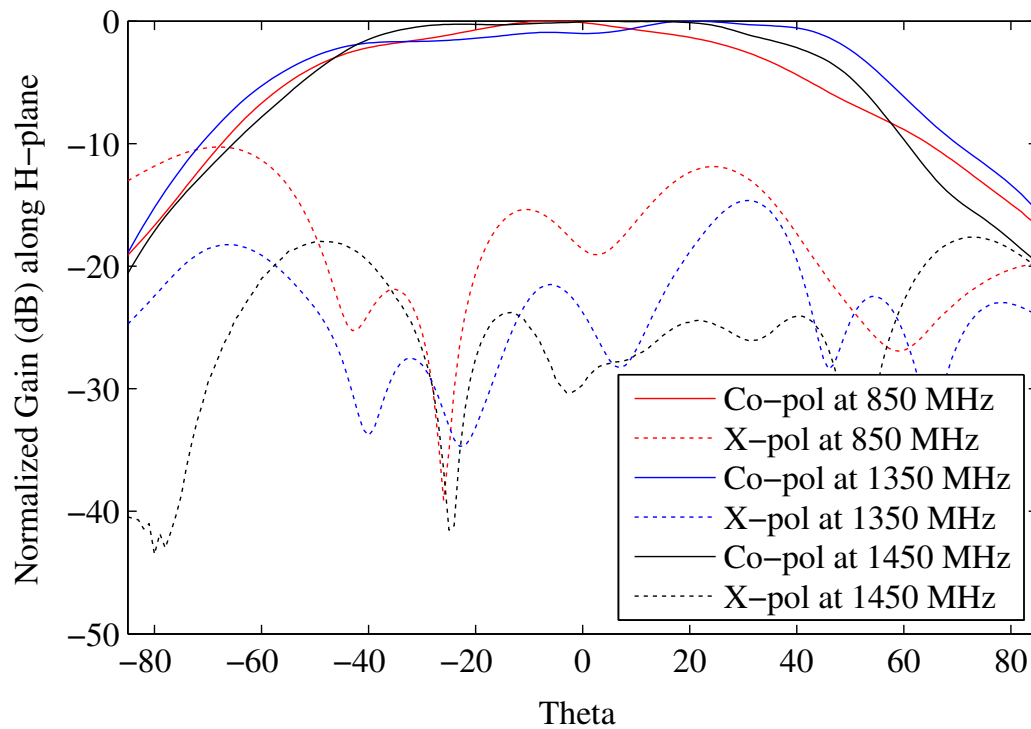


Figure 6.19: Normalised co-polar and cross-polar gain patterns along the  $H$ -plane for an embedded element.

## Chapter 7

# Conclusion and Future Work

This dissertation presented the design of a Dual-Polarized Dense Dipole Array for the SKA Mid-Frequency Aperture Array. The DDA is an implementation of Wheeler's current sheet array - instead of designing a single antenna element that has the required performance characteristics and then arranging many of these elements into a large array, the array is designed as an antenna array from the start by assuming the array is infinite.

This design approach allows for the exploitation of the mutual coupling between the array elements in order to stabilize the active array impedance across a wider frequency range which in turn increases the achievable array bandwidth. The capacitances between the tips of neighbouring dipole elements are used to cancel out the inductance of the ground plane and the elements themselves. In addition to that, the close proximity of the elements to one another due to their dense arrangement ( $d < \lambda/2$ ) across the entire in-band frequency range also contributes to the increased bandwidth since the physical area available for the energy associated with evanescent waves stored around antenna elements is significantly reduced compared to that of an isolated antenna element [13].

For the single-polarized DDA discussed in Chapter 3 a 3.8:1 bandwidth was achieved, while a smaller bandwidth was achieved for the dual-polarized DDA. This apparent performance penalty was attributed to difficulties encountered with the optimization process, and it is anticipated that should these problems be resolved in future, the bandwidth performance of the dual-polarized array would be able to match that of the single-polarized array.

An inherent problem with connected, dense antenna arrays like the DDA as well as the ORA [1] and the Vivaldi Array [59] is that the designs create a current path that result in the introduction of common-mode resonances at certain frequencies and scan angles. A major contribution of this project was the design of a wide-band common-mode filter that has proved to effectively suppress these common-mode resonances at all measured frequencies.



The DDA design, including the common-mode suppressing feed, was verified by building two prototype arrays. The first prototype was a single-polarized  $4 \times 4$  array printed on FR4 with the common-mode suppressing feed board incorporated. The simulation was that of a lossless finite array where an infinite ground plane and substrate is assumed. For a central element pair, the agreement between the simulated and measured results was reasonable considering the simulation assumptions; however, at the corner element there was much greater discrepancy between the results. This indicated that edge effects should be taken into consideration when scaling this array down from an infinite array to a finite one.

The measurements of the active reflection coefficient of a central element pair for the  $4 \times 4 \times 1$  prototype under common-mode excitation also showed good common-mode rejection. This provided further confirmation of the effectiveness of the common-mode suppressing feed-board.

Another major contribution of this project was the development of a large DDA prototype. This prototype was a much larger  $10 \times 10 \times 2$  array and while some difficulties were experienced in simulating such a large finite structure, there was still reasonable agreement between the measured and simulated results. Furthermore, the embedded gain pattern measurements of the large prototype indicate performance that compared well with that of other MFAA prototypes currently under investigation. The relatively flat embedded element pattern is a crucial performance characteristic in achieving cost-effective digital beam-forming.

In the absence of fixed system specifications, the DDA was designed to have performance that compared with the other MFAA candidate topologies. The strength of the DDA compared to the other MFAA topologies, however, is its planar structure. The ORA employs an extra superstrate layer in order to improve the bandwidth, which increases the required amount of manufacturing material as well as the manufacturing complexity. The Vivaldi array as well as the LPDA are inherently three dimensional structures, complicating the mass production process. Although the connection of the feed structure of the DDA during the assembly of the prototypes proved to be an intricate process, this is a problem common to all the MFAA candidate topologies. As a result it was not judged a major drawback of the DDA at this stage.

It should also be noted that this technology is not limited to use in radio-astronomy. Although the investigation of possible future MFAA topologies was the motivation behind this project, it can be deployed in any environment where high sensitivity is a key performance requirement, for instance in Radar, which was the background from which Munk developed the underlying theory in [13].

The following publications present work from this dissertation:

1. A review of full-wave and reduced-order modelling techniques for large, dense antenna arrays as proposed for the Square Kilometre Array is presented in [73]. A reduced-order method of modelling microstrip-fed Vivaldi Arrays, the Infinite Array Approximation as well as the Domain Green's Function method are discussed with specific reference made to runtime, memory usage and solution accuracy as compared to that of brute-force MoM solutions.
2. Preliminary results of a single-polarized Dense Dipole Array (DDA) design are presented in [68]. The array consists of tightly coupled dipole elements above a ground plane and fed differentially through a specially designed common-mode suppressing feed. Measurements of a  $4 \times 4$  prototype indicate an impedance bandwidth of  $\approx 2.5 : 1$ .
3. A design of an antenna feed that suppresses common-mode resonances commonly encountered in connected antenna arrays is presented in [77]. The design makes use of symmetrical wideband microstrip-slotline transitions to cancel out common-mode signals, while differential signals will still propagate through. The design is verified using both simulations and measurements of a manufactured prototype. A wide bandwidth and a CMRR  $> 30$  dB is achieved that exceeds the design specifications set out.
4. Progress made on the design of the DDA, specifically the expansion of the design into a dual-polarized array is presented in [78]. This paper primarily focusses on the simulated results for the dual-polarized DDA. A wide bandwidth is realized and good cross-polarization performance for an element embedded in the infinite array is demonstrated.

In conclusion, future work on this project could include the following:

1. Identifying a method with which the dual-polarized DDA structure can be effectively optimized.
2. Design of a differential low noise amplifier for the DDA.
3. Generating simulation results that describe the noise performance of a large, dense array is a computationally expensive exercise. The development of computational methods that can be used to minimize the computational complexity of the problem will therefore also be useful.
4. In the absence of efficient computational techniques for determining the noise performance of a large, dense array, measurements of the

noise performance with an integrated LNA is the most accurate and time-efficient way of determining  $T_{sys}$  at this stage. This will be a crucial step in confirming the viability of the DDA for use in radio astronomy.

5. Improvements in the manufacturability of the array, including investigating alternative materials that simplifies the manufacturing and assembly process while maintaining good noise performance. These materials and methods include the method that was used to manufacture the ORA [1] and early Vivaldi prototypes [59], i.e. screen-printing the antenna elements on foil using silver ink and then electro-plating them afterwards.

# Bibliography

- [1] Y. Zhang and A. K. Brown, "Octagonal Ring Antenna for a Compact Dual-Polarized Aperture Array," *IEEE Transactions on Antennas and Propagation*, vol. 59, no. 10, pp. 3927–3932, oct 2011.
- [2] A. van Ardenne, J. Bregman, W. van Cappellen, G. Kant, and J. de Vaate, "Extending the Field of View With Phased Array Techniques: Results of European SKA Research," *Proceedings of the IEEE*, vol. 97, no. 8, pp. 1531–1542, aug 2009.
- [3] P. Dewdney, P. Hall, R. Schilizzi, and T. Lazio, "The Square Kilometre Array," *Proceedings of the IEEE*, vol. 97, no. 8, pp. 1482–1496, aug 2009.
- [4] P. Hall, R. Schilizzi, P. Dewdney, and T. Lazio, "The Square Kilometer Array ( SKA ) Radio Telescope : Progress and Technical Directions," *Radio Science Bulletin*, vol. 326, no. 326, pp. 4–19, 2008.
- [5] R. Braun and W. van Cappellen, "Aperture Arrays for the SKA: Dense or Sparse?" p. 15, nov 2006.
- [6] J. G. Bij de Vaate, S. A. Torchinsky, A. J. Faulkner, Y. Zhang, A. Gunst, P. Benthem, I. M. van Bemmelen, and G. Kenfack, "SKA Mid Frequency Aperture arrays: Technology for the ultimate survey machine," in *2014 XXXIth URSI General Assembly and Scientific Symposium (URSI GASS)*. IEEE, aug 2014, pp. 1–4.
- [7] G. W. Kant, P. D. Patel, S. J. Wijnholds, M. Ruiter, and E. van der Wal, "EMBRACE: A Multi-Beam 20,000-Element Radio Astronomical Phased Array Antenna Demonstrator," *IEEE Transactions on Antennas and Propagation*, vol. 59, no. 6, pp. 1990–2003, jun 2011.
- [8] A. J. Faulkner and P. Alexander, "Design Considerations for an SKA Quality , Cost Effective Aperture Array," pp. 2009–2011, 2009. [Online]. Available: [http://www.skads-eu.org/PDF/EMTS\\_paper\\_AJF\\_submitted.pdf](http://www.skads-eu.org/PDF/EMTS_paper_AJF_submitted.pdf)
- [9] I. M. van Bemmelen, A. van Ardenne, J. G. bij de Vaate, A. J. Faulkner, and R. Morganti, "Mid-frequency aperture arrays: the future of radio

- astronomy," *Resolving the Sky Radio Interferometry Past Present and Future RTS2012*, p. 8, aug 2012.
- [10] A. J. Faulkner, "Dense aperture arrays for the Square Kilometre Array," in *2011 XXXth URSI General Assembly and Scientific Symposium*, University of Cambridge, Cavendish Laboratory, Cambridge CB3 0HE, UK. IEEE, aug 2011, pp. 1–4.
- [11] H. Wheeler, "Simple relations derived from a phased-array antenna made of an infinite current sheet," *IEEE Transactions on Antennas and Propagation*, vol. 13, no. 4, pp. 506–514, jul 1965.
- [12] B. A. Munk, *Frequency Selective Surfaces*. Hoboken, NJ, USA: John Wiley & Sons, Inc., apr 2000.
- [13] B. a. Munk, *Finite Antenna Arrays and FSS*. Hoboken, NJ, USA: John Wiley & Sons, Inc., jul 2003.
- [14] P. Benthem and G. W. Kant, "EMBRACE : Results From an Aperture Array for Radio Astronomy," in *6th European Conference on Antennas and Propagation (EUCAP)*, 2012, pp. 629–633.
- [15] "Square Kilometre Array Website." [Online]. Available: [www.skatelescope.org](http://www.skatelescope.org)
- [16] B. Munk, R. Taylor, T. Durharn, W. Croswell, B. Pigon, R. Boozer, S. Brown, M. Jones, J. Pryor, S. Ortiz, J. Rawnick, K. Krebs, M. Vanstrum, G. Gothard, and D. Wiebelt, "A low-profile broadband phased array antenna," in *IEEE Antennas and Propagation Society International Symposium. Digest. Held in conjunction with: USNC/CNC/URSI North American Radio Sci. Meeting (Cat. No.03CH37450)*, vol. 2. IEEE, 2003, pp. 448–451.
- [17] D. Cavallo, A. Neto, and G. Gerini, "PCB Slot Based Transformers to Avoid Common-Mode Resonances in Connected Arrays of Dipoles," *IEEE Transactions on Antennas and Propagation*, vol. 58, no. 8, pp. 2767–2771, aug 2010.
- [18] J. D. Kraus, *Radio Astronomy*, 2nd ed. Durham, NH: Cygnus- Quasar, 2005.
- [19] S. Hay, J. O'Sullivan, J. Kot, C. Granet, A. Grancea, A. Forsyth, and D. Hayman, "Focal plane array development for ASKAP (Australian SKA pathfinder)," in *IET Seminar Digests*. IET, 2007, pp. 775–775.
- [20] D. R. DeBoer, R. G. Gough, J. D. Bunton, T. J. Cornwell, R. J. Beresford, S. Johnston, I. J. Feain, A. E. Schinckel, C. A. Jackson, M. J. Kesteven, A. Chippendale, G. A. Hampson, J. D. O'Sullivan, S. G. Hay,

- C. E. Jacka, T. W. Sweetnam, M. C. Storey, L. Ball, and B. J. Boyle, "Australian SKA Pathfinder: A High-Dynamic Range Wide-Field of View Survey Telescope," *Proceedings of the IEEE*, vol. 97, no. 8, pp. 1507–1521, aug 2009.
- [21] R. Maaskant, M. V. Ivashina, O. Iupikov, E. A. Redkina, S. Kasturi, and D. H. Schaubert, "Analysis of Large Microstrip-Fed Tapered Slot Antenna Arrays by Combining Electrodynamic and Quasi-Static Field Models," *IEEE Transactions on Antennas and Propagation*, vol. 59, no. 6, pp. 1798–1807, jun 2011.
- [22] A. K. Bhattacharyya, *Phased Array Antennas: Floquet Analysis, Synthesis, BFNs, and Active Array Systems*. John Wiley & Sons Inc, 2006.
- [23] E. Garcia, E. de Lera, D. Segovia, V. Gonzalez, and J. Lopez-Fernandez, "Elimination of scan impedance anomalies in ultra-wide band phased arrays of differentially fed tapered slot antenna elements," in *2008 IEEE Antennas and Propagation Society International Symposium*. IEEE, jul 2008, pp. 1–4.
- [24] E. de Lera Acedo, E. Garcia, V. Gonzalez-Posadas, J. Vazquez-Roy, R. Maaskant, and D. Segovia, "Study and Design of a Differentially-Fed Tapered Slot Antenna Array," *IEEE Transactions on Antennas and Propagation*, vol. 58, no. 1, pp. 68–78, jan 2010.
- [25] D. J. Ludick, U. Jakobus, and D. B. Davidson, "Numerical analysis of finite antenna arrays using the Domain Green's Function Method," in *2012 International Conference on Electromagnetics in Advanced Applications*, no. 2. IEEE, sep 2012, pp. 216–219.
- [26] D. J. Ludick, R. Maaskant, R. Mittra, U. Jakobus, and D. B. Davidson, "Applying the CBFM-Enhanced Domain Greens Function Method to the Analysis of Large Disjoint Subarray Antennas," in *International Conference on Electromagnetics in Advanced Applications (ICEAA)*, 2013, pp. 94–97.
- [27] J. P. Hamaker, J. D. Bregman, and R. J. Sault, "Understanding radio polarimetry. I. Mathematical foundations," *Astronomy and Astrophysics Supplement Series*, vol. 117, no. 1, pp. 137–147, may 1996.
- [28] D. McGrath, N. Schuneman, T. Shively, and J. Irion, "Polarization properties of scanning arrays," in *IEEE International Symposium on Phased Array Systems and Technology*, 2003., no. 3. IEEE, 2003, pp. 295–299.
- [29] A. Ludwig, "The definition of cross polarization," *IEEE Transactions on Antennas and Propagation*, vol. 21, no. 1, pp. 116–119, jan 1973.

- [30] M. Roy and D. George, "Estimation of Coupled Noise in Low Noise Phased Array Antennas," *IEEE Transactions on Antennas and Propagation*, vol. 59, no. 6, pp. 1846–1854, jun 2011.
- [31] C. H. Niow and H. T. Hui, "Improved Noise Modeling with Mutual Coupling in Receiving Antenna Arrays for Direction-of-Arrival Estimation," *IEEE Transactions on Wireless Communications*, vol. 11, no. 4, pp. 1616–1621, apr 2012.
- [32] R. Maaskant and E. Woestenburg, "Applying the active antenna impedance to achieve noise match in receiving array antennas," in *2007 IEEE Antennas and Propagation International Symposium*. IEEE, jun 2007, pp. 5889–5892.
- [33] M. V. Ivashina, R. Maaskant, and B. Woestenburg, "Equivalent system representation to model the beam sensitivity of receiving antenna arrays," *IEEE Antennas and Wireless Propagation Letters*, vol. 7, pp. 733–737, 2008.
- [34] K. F. Warnick, M. V. Ivashina, R. Maaskant, and B. Woestenburg, "Unified Definitions of Efficiencies and System Noise Temperature for Receiving Antenna Arrays," *IEEE Transactions on Antennas and Propagation*, vol. 58, no. 6, pp. 2121–2125, jun 2010.
- [35] K. Warnick and B. Jeffs, "Efficiencies and System Temperature for a Beamforming Array," *IEEE Antennas and Wireless Propagation Letters*, vol. 7, pp. 565–568, 2008.
- [36] K. F. Warnick, "Optimal noise matching for a phased array feed," in *2009 IEEE Antennas and Propagation Society International Symposium*, no. 2. IEEE, jun 2009, pp. 1–4.
- [37] B. Woestenburg, "Definition of Array Receiver System Gain and Noise Temperature," pp. 1–12, 2008. [Online]. Available: <http://www.skatelescope.org/publications/>
- [38] E. Woestenburg and K. F. Dijkstra, "Noise characterization of a phased array tile," in *33rd European Microwave Conference, 2003*, vol. 1, no. 2. IEEE, oct 2003, pp. 363–366.
- [39] E. Brookner and J. Howell, "Right way to calculate reflector and active-phased-array antenna system noise temperature taking into account antenna mismatch," in *IEEE International Symposium on Phased Array Systems and Technology, 2003*. IEEE, 2003, pp. 130–135.
- [40] R. Janaswamy and D. Schaubert, "Analysis of the tapered slot antenna," *IEEE Transactions on Antennas and Propagation*, vol. 35, no. 9, pp. 1058–1065, sep 1987.



- [41] D. Schaubert, "A parameter study of stripline-fed Vivaldi notch-antenna arrays," *IEEE Transactions on Antennas and Propagation*, vol. 47, no. 5, pp. 879–886, may 1999.
- [42] —, "Parameter study and design of wide-band widescan dual-polarized tapered slot antenna arrays," *IEEE Transactions on Antennas and Propagation*, vol. 48, no. 6, pp. 879–886, jun 2000.
- [43] D. H. Schaubert and T.-H. Chio, "Wideband Vivaldi Arrays for Large Aperture Antennas," in *Perspectives on Radio Astronomy: Technologies for Large Antenna Arrays*, A. B. Smolders and M. P. Haarlem, Ed. Dwingeloo: ASTRON, 1999, pp. 49–57.
- [44] N.-T. Huang, R. Mittra, M. Ivashina, and R. Maaskant, "Numerical study of a dual-polarized Focal Plane Array (FPA) with Vivaldi elements placed in the vicinity of a large feed box using the parallelized FDTD code GEMS," in *2009 IEEE Antennas and Propagation Society International Symposium*. IEEE, jun 2009, pp. 1–4.
- [45] H. Oraizi and S. Jam, "Optimum design of tapered slot antenna profile," *IEEE Transactions on Antennas and Propagation*, vol. 51, no. 8, pp. 1987–1995, aug 2003.
- [46] D. Schaubert, T.-H. Chio, and H. Holter, "TSA element design for 500-1500 MHz array," in *IEEE Antennas and Propagation Society International Symposium. Transmitting Waves of Progress to the Next Millennium. 2000 Digest. Held in conjunction with: USNC/URSI National Radio Science Meeting (Cat. No.00CH37118)*, vol. 1. IEEE, pp. 178–181.
- [47] "Netherlands Institute for Radio Astronomy (ASTRON) Website." [Online]. Available: [www.astron.nl](http://www.astron.nl)
- [48] J. B. de Vaate and D. Kant, "The Phased Array Approach to SKA, Results of a Demonstrator Project," in *32nd European Microwave Conference, 2002*, no. 3. IEEE, oct 2002, pp. 1–4.
- [49] Y. Zhang and A. K. Brown, "A high performance planar phased array for wide field of view applications," in *2012 International Conference on Electromagnetics in Advanced Applications*. IEEE, sep 2012, pp. 375–378.
- [50] E. de Lera Acedo, "SKALA: A log-periodic antenna for the SKA," in *2012 International Conference on Electromagnetics in Advanced Applications*. IEEE, sep 2012, pp. 353–356.
- [51] E. de Lera Acedo, N. Razavi-Ghods, E. Garcia, P. Duffett-Smith, and P. Alexander, "Analysis of an ultra wideband aperture array element for low frequency radio astronomy," in *2009 IEEE Antennas and*



- Propagation Society International Symposium*, vol. 3966, no. 1. IEEE, jun 2009, pp. 1–4.
- [52] E. Colin-Beltran, A. J. Faulkner, and E. de Lera-Acedo, “Log-periodic sparse aperture array antennas dedicated to the MFAA instrument of the SKA telescope,” in *2014 International Conference on Electromagnetics in Advanced Applications (ICEAA)*. IEEE, aug 2014, pp. 746–749.
- [53] E. Colin-Beltran and E. de Lera Acedo, “Directivity optimization of a Log-periodic antenna for the SKA-AAMid instrument,” in *2015 IEEE International Symposium on Antennas and Propagation & USNC/URSI National Radio Science Meeting*. Vancouver, BC: IEEE, jul 2015, pp. 1700–1701.
- [54] Altair Engineering, “FEKO Suite 7.0,” Stellenbosch, South Africa, 2014. [Online]. Available: <http://www.feko.info>
- [55] J. Noordam and J. Voute, “Design Aspects of a Tile Telescope: A possible approach to a Square Kilometre Array Interferometer (SKAI),” ASTRON, Dwingeloo, Netherlands, Tech. Rep., 1994.
- [56] C. Balanis, *Antenna theory: analysis and design*, 3rd ed. Hoboken, NJ, USA: John Wiley & Sons, Inc., 2005.
- [57] “FEKO Suite 6.3,” Stellenbosch, South Africa, 2013. [Online]. Available: <http://www.feko.info>
- [58] D. Bockelman and W. Eisenstadt, “Combined differential and common-mode scattering parameters: theory and simulation,” *IEEE Transactions on Microwave Theory and Techniques*, vol. 43, no. 7, pp. 1530–1539, jul 1995.
- [59] M. Arts, R. Maaskant, E. De Lera Acedo, and J. G. Bij De Vaate, “Broadband differentially fed tapered slot antenna array for radio astronomy applications,” in *2009 3rd European Conference on Antennas and Propagation*. Berlin: IEEE, 2009, pp. 566 – 570.
- [60] D. M. Pozar, *Microwave Engineering*, 4th ed. John Wiley & Sons Inc, 2012.
- [61] J. Robinson and Y. Rahmat-Samii, “Particle Swarm Optimization in Electromagnetics,” *IEEE Transactions on Antennas and Propagation*, vol. 52, no. 2, pp. 397–407, feb 2004.
- [62] F. J. Ares-pena, S. Member, J. A. Rodriguez-gonzalez, E. Villanueva-lopez, and S. R. Rengarajan, “Genetic Algorithms in the Design and Optimization of Antenna Array Patterns,” vol. 47, no. 3, pp. 506–510, 1999.

- [63] D. S. V. D. M. Prinsloo, "Multi-Mode Antennas for Hemispherical Field-of-View Coverage," PhD, Stellenbosch University, 2015.
- [64] L. E. Garcia-Munoz, D. Segovia-Vargas, O. Garcia-Perez, E. Ugarte-Munoz, V. Gonzalez-Posadas, J. M. Serna-Puente, and J. A. Lopez-Fernandez, "Broadband active differential array for the mid-frequency SKA band," *IEEE Antennas and Propagation Magazine*, vol. 56, no. 2, pp. 27–38, apr 2014.
- [65] K. Gupta, R. Garg, I. Bahl, and P. Bharta, *Microstrip Lines and Slotlines*, 2nd ed. Artech House Inc, 1996.
- [66] D. Cavallo, A. Neto, and G. Gerini, "Connected phased array antennas for ultra-wide band radar applications," in *2008 IEEE International Conference on Microwaves, Communications, Antennas and Electronic Systems*. IEEE, may 2008, pp. 1–10.
- [67] D. Cavallo, A. Neto, G. Gerini, and A. Micco, "A Novel Printed-Circuit-Board Feeding Structure for Common-Mode Rejection in Wide-Scanning Connected Arrays of Dipoles," in *Proceedings of the Fourth European Conference on Antennas and Propagation (EuCAP)*. Barcelona, Spain: IEEE, 2010, pp. 1–4.
- [68] J. Gilmore, D. Davidson, and J. Noordam, "A Dense Dipole Array for mid-frequency aperture arrays," in *2015 IEEE International Symposium on Antennas and Propagation & USNC/URSI National Radio Science Meeting*. Vancouver, BC: IEEE, jul 2015, pp. 1524–1525.
- [69] J. Knorr, "Slot-Line Transitions," *IEEE Transactions on Microwave Theory and Techniques*, vol. 22, no. 5, pp. 548–554, may 1974.
- [70] B. Shuppert, "Microstrip/slotline transitions: modeling and experimental investigation," *IEEE Transactions on Microwave Theory and Techniques*, vol. 36, no. 8, pp. 1272–1282, 1988.
- [71] M. M. Zinieris, R. Sloan, and L. E. Davis, "A broadband microstrip-to-slot-line transition," *Microwave and Optical Technology Letters*, vol. 18, no. 5, pp. 339–342, aug 1998.
- [72] B. Schuppert, "Analysis and Design of Microwave Balanced Mixers," *IEEE Transactions on Microwave Theory and Techniques*, vol. 34, no. 1, pp. 120–128, jan 1986.
- [73] J. Gilmore and D. B. Davidson, "A review of full-wave and reduced-order modelling methodologies for dense aperture arrays," in *The 8th European Conference on Antennas and Propagation (EuCAP 2014)*, no. EuCAP. The Hague, Netherlands: IEEE, apr 2014, pp. 3317–3320.

- [74] "RT/duroid  $\hat{A}$ ® 5870 /5880 High Frequency Laminates." [Online]. Available: <http://www.rogerscorp.com/documents/606/acm/RT-duroid-5870-5880-Data-Sheet.pdf>
- [75] W. Fan, A. Lu, L. Wai, and B. Lok, "Mixed-mode S-parameter characterization of differential structures," in *Proceedings of the 5th Electronics Packaging Technology Conference (EPTC 2003)*. IEEE, 2003, pp. 533–537.
- [76] P. Meyer and D. Prinsloo, "Generalized Multi-Mode Scattering Parameter and Antenna Far-Field Conversions," *IEEE Transactions on Antennas and Propagation*, no. c, pp. 1–1, 2015.
- [77] J. Gilmore and D. B. Davidson, "Suppressing Undesired Common-Mode Resonances in Connected Antenna Arrays," *IEEE Transactions on Antennas and Propagation*, vol. 63, no. 11, pp. 5245–5250, nov 2015.
- [78] J. Gilmore, D. B. Davidson, and J. G. Bij de Vaate, "Progress on the Development of a Dual-Polarized Dense Dipole Array for the SKA Mid-Frequency Aperture Array," in *Abstract submitted to the 10th European Conference on Antennas and Propagation (EuCAP 2016)*, 2000, pp. 2–3.